HIGH PRESSURE STUDIES OF HYDROGEN BONDED SOLIDS

by

Bharat Bhooshan

Enrollment No. PHY01201204007

Bhabha Atomic Research Centre, Mumbai

A thesis submitted to the
Board of Studies in Physical Sciences
In partial fulfillment of requirements
for the degree of

DOCTOR OF PHILOSOPHY

of
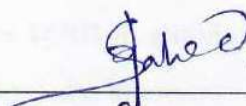
HOMI BHABHA NATIONAL INSTITUTE

December, 2017

Homi Bhabha National Institute

Recommendations of the Viva Voce Committee

As members of the Viva Voce Committee, we certify that we have read the dissertation prepared by **Bharat Bhooshan** entitled **High Pressure Studies of Hydrogen Bonded Solids** and recommend that it may be accepted as fulfilling the thesis requirement for the award of Degree of Doctor of Philosophy.
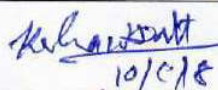
Chairman Name & Signature with date _____ _Jalee_ 10/5/18
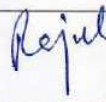
Guide / Convener Name & Signature with date _____ 10/5/18 (CHITRA MURLI)

Examiner Name & Signature with date _____ _Godhun_ 10/5/18

Member 1 Name & Signature with date _____ 10/5/18

Member 2 Name & Signature with date _____ _Rejul_ 10/5/18

Member 3 Name & Signature with date _____

Technology Advisor Name & Signature with date _____ 10/5/18

Final approval and acceptance of this thesis is contingent upon the candidate's submission of the final copies of the thesis to HBNI. I/We hereby certify that I/we have read this thesis prepared under my/our direction and recommend that it may be accepted as fulfilling the thesis requirement. Date:

Place:

Signature

Guide   CHITRA MURLI

STATEMENT BY AUTHOR

This dissertation has been submitted in partial fulfillment of requirements for an advanced degree at Homi Bhabha National Institute (HBNI) and is deposited in the Library to be made available to borrowers under rules of the HBNI.

Brief quotations from this dissertation are allowable without special permission, provided that accurate acknowledgement of source is made. Requests for permission for extended quotation from or reproduction of this manuscript in whole or in part may be granted by the Competent Authority of HBNI when in his or her judgment the proposed use of the material is in the interests of scholarship. In all other instances, however, permission must be obtained from the author.

Signature

Candidate Name

Bharat Bhooshan

DECLARATION

I, hereby declare that the investigation presented in the thesis has been carried out by me. The work is original and has not been submitted earlier as a whole or in part for a degree / diploma at this or any other Institution / University.

Bharat Bhooshan

Signature

Candidate Name

Bharat Bhooshan

List of publications arising from the thesis

Journals

1. Hydrogen Bonds and Ionic forms Versus Polymerization of Imidazole at High Pressures; Bharat Bhooshan Sharma, Ashok Kumar Verma, Susy Thomas, Chitra Murli, and Surinder M Sharma; Journal of Physical Chemistry B, 2015, 119(1), 372-378.

2. Hydrogen bonds and Polymerization in Acrylamide under Pressure; Bharat Bhooshan Sharma, Chitra Murli and Surinder M. Sharma; Journal of Raman Spectroscopy Journal of Raman Spectroscopy 2013, 44 (5), 785-790.

3. Hydrogen-bonding interactions in fully deuterated α-glycine at high Pressures; Bharat Bhooshan Sharma, Chitra Murli, R. Chitra, Surinder M. Sharma; Journal of Raman Spectroscopy 2012, 43, 138-145.

4. Hyper-coordination of Iodine under Pressure: Raman, X-Ray and *ab-initio* Studies of Iodic Acid. (*To be submitted*)

Conferences

1. High Pressure Raman And XRD Investigation of Iodic Acid (HIO_3); Bharat Bhooshan Sharma, Partha Sarathi Ghosh, Himanshu Kumar Poswal, Chitra Murli; 62nd DAE-SSPS, December 26-30 2017, Mumbai, India.

2. Imidazole under Pressure - A Raman Spectroscopic Study; Bharat Bhooshan Sharma, Chitra Murli, Susy Thomas, Surinder M. Sharma; DAE-BRNS Conference on Organic Devices: The Future Ahead (ODeFA-2014) March 3-6, 2014.

3. Structural behaviour of niobium oxynitride under high pressure; Bharat Bhooshan Sharma, HK Poswal, KK Pandey, Surinder M Sharma, JV Yakhmi, Y Ohashi, S Kikkawa; 58th DAE-SSPS, 17-21 December 2013 Location: Thapar University, Patiala, Punjab, India; AIP Conf. Proc., Volume 1591, Issue 1, 156-157.

4. Structural behaviour of Mg, Al and Si doped Niobium Oxynitrides under high pressures; Bharat Bhooshan Sharma, H.K. Poswal, Surinder M Sharma and J. V. Yakhmi, Y.

Ohashi and S. Kikkawa; 57th DAE-SSPS, Dec. 3-7, 2012, IIT-Mumbai; AIP Conf. Proc. 1512, 108-109, 2013.

5. Raman Investigations of Polymerization in Acrylamide under Pressure; Bharat Bhooshan Sharma, C. Murli, Surinder M. Sharma; AIRAPT-23, Sept 25-30, 2011, BARC, Mumbai-400085, India.

6. Rocksalt to monoclinic transformation in nano nickel oxide at high Pressures; Nandini Garg, B. Bhooshan, A.K. Mishra, S. Vaidya, A.K. Ganguli, Surinder M Sharma; AIRAPT - 23, Sept 25-30, 2011, BARC, Mumbai-400085, India.

Bharat Bhooshan

Signature

Candidate Name

Bharat Bhooshan

DEDICATIONS

Dedicated to my father

ACKNOWLEDGEMENT

It would not have been possible to write this doctoral thesis without the help and support of the kind people around me. It is a pleasure to convey my gratitude to them all in my humble acknowledgment. First of all, I wish to express my heartfelt gratitude to my supervisor Prof. (Dr.) Chitra Murli for her inspiring guidance, strong motivation, valuable advice and encouragement from the very early stage of this research as well as giving me extraordinary experiences throughout the work. I appreciate her for the enduring interests in her student's progress and her ability to clear the doubts at all time. I am also indebted to her for patiently going through the thesis and for her critical comments. My sincere thanks goes to Mr. Yogesh Kumar for his efforts in reviewing the thesis, enlightening suggestions, support and encouragement. I would also like to thank to my dissertation committee members Dr. (Mrs.) R. R. Choudhary, Dr. K. D. Joshi, Dr. N. K. Sahoo, Dr. S. K. Deb, Dr. D. K. Aswal and Dr. H. K. Poswal for their time, effort and valuable suggestions which were important in improving the quality of this research.

SYNOPSIS

High Pressure Studies of Hydrogen Bonded Solids

Introduction

Hydrogen bond (X-H- - -Y) is an electrostatic, directional attractive interaction in which hydrogen (H) atom interacts between two electronegative atoms X and Y. It significantly influences the physical and chemical properties of a material such as boiling point, dielectric constant, surface tension *etc.* Hydrogen bonding interactions also play an important role in the supramolecular polymers [1,2] fuel cells [3], biophysical [4], geophysical [5], polymerization/amorphization [6,7] and materials research applications [8]. This thesis explores the role of hydrogen bonds on the pressure induced structural and polymeric transitions in some solids of relevance to basic and advanced materials research.

Chapter 1: Introduction to Hydrogen Bond and High Pressure

Different types of hydrogen bonds which are found in nature such as co-operative, bifurcated, multi-centered *etc.* are described in detail to explore the bonding nature. To understand the concept of hydrogen bond, simple one dimensional theoretical model has also been discussed. Description of the recent developments in the high pressure research on hydrogen bonded materials and various techniques such as Raman/IR spectroscopy and diffraction methods to probe hydrogen bonding interactions have also been discussed in this chapter.

Pressure is an important thermodynamical variable which results in changes in the crystal structure, electronic state and physical properties. A detailed description of pressure as a variable is given in this chapter. Design and development of various high pressure devices such as piston cylinder, Bridgman anvil cell *etc.* are discussed in detail. Diamond anvil cell (DAC) which is extensively used for high pressure investigation, and practical methods to generate high pressure using DAC is described in this chapter with full description of diamonds, piston-cylinder, gasket materials and pressure generation mechanism. An introduction to various pressure transmitting mediums to generate hydrostatic condition and

methods to measure the pressure inside the diamond anvil cell, such as Ruby fluorescence, equation of state, *etc.* are described in detail along with the relevant examples. Recent frontier of high pressure materials research has also been included to complete the discussion. A detailed introduction of the theoretical and experimental methods for Raman scattering and x-ray diffraction techniques is given in the context of high pressure research carried out for this doctoral thesis. Important instrument parameters, schematic diagram of the Raman and x-ray instrument set-up are also discussed in detail.

Chapter 2: Hydrogen bond Vs Conformational Changes: Deuterated α-Glycine

Amino acids are the basic building blocks of protein structures which fold in different ways for the growth, repair and working of the living cells. Hydrogen bonding interactions control the secondary structures of protein and play an important role in stabilizing the structure. The deuterated form of α-glycine, which is the simplest amino acid, has been studied under pressure using Raman spectroscopic investigations up to $\sim$20 GPa. A detailed review of the high pressure behavior of several other amino acids in the context of hydrogen bonds is also presented. The discontinuous changes in the vibrational modes corresponding to ND_3^+ and COO groups and decrease in intensity of the ND_3^+ torsional mode indicated possible conformational changes of glycine molecules across $\sim$3 GPa [9]. In un-deuterated glycine NH_3^+ torsional and N-H stretching modes were found overlapping with the other modes. In order to study the high pressure behavior of these modes under pressure, deuterated form of this compound was studied. Due to different atomic weight of deuterium (D) from hydrogen (H), reduced mass of the corresponding vibrating atoms changes and the corresponding vibrational modes shift to lower wavenumbers. Hence the ambiguity in the vibrational assignment of ND_3^+ torsion and N-D stretching bands were removed.

Under pressure, competing interaction of intra layer N-D- - -O hydrogen bond with the emerging interlayer C-D- - -O hydrogen bonds result in conformational changes of the molecular units with subtle structural modifications and inhibit any drastic change in the crystal symmetry.

Chapter 3: Hydrogen Bond Vs Polymerization: Acrylamide

Acrylamide (C_3H_5NO) is a hydrogen bonded amide useful in DNA analysis, sewage/wastewater treatment, pesticide formulations, cosmetics, sugar manufacturing, soil erosion prevention, ore processing, food packaging, plastic products, and paper production. Acrylamide is also considered as a potential carcinogen which is recently confirmed in several heated/backed food articles. High pressure is a novel method to synthesize new materials as an alternative to chemical methods. Molecules having unsaturated double or triple bonds tend to saturate by breaking bonds, when they are forced close to each other under pressure. During this process, conformation of the molecules in unit cell and the associated hydrogen bonds play an important role.

High pressure Raman investigations were carried out up to ~17 GPa to understand the mechanism of polymerization under pressure [10]. Studies revealed the significant impact of inter-molecular interactions as well as in hydrogen bonds under pressure on polymerization. Relative intensity of the CH_2 symmetric stretching mode decreases drastically with respect to CH_2 asymmetric stretching mode as well as CH stretch mode up to 1.4 GPa. Along with this, new modes emerge adjacent to both CH_2 symmetric and asymmetric stretching modes. NH_2 symmetric mode softens up to ~2 GPa and shows a discontinuous jump to a higher value at 2.6 GPa which indicates reorganization of N-H- - -O bonds of the initial phase and formation of relatively weaker N-H- - -O bonds in the new phase. Also discontinuous changes in the relative intensity of C-O torsional mode, decrease in the relative intensity of NH_2 deformational mode, splitting of C=O stretching and CH_2 rocking modes were observed. Aforementioned changes are some of the spectral changes observed in the pressure range up to 2.8 GPa indicating a structural phase transition. Vibrational modes of polyacrylamide emerge at 4 GPa and the relative intensities of these new modes were found to increase with pressure. Characteristic C-H polymer band of polyacrylamide at ~2900 cm^{-1} became visible at pressures above 17 GPa and also its relative intensity increased during decompression. Acrylamide molecules are arranged in dimer form through intra-dimer hydrogen bond. These

dimer units are connected to each other through another inter-dimer N-H- - -N hydrogen bond. So acrylamide which is having unsaturated double bond combined to each other with extensive network of strong hydrogen bonds that influences its structural stability. When acrylamide is subjected to high pressure, molecules come close to each other by the rearrangement of hydrogen bonds at ∼2.6 GPa resulting in a new phase that assists in the close interaction of adjacent acrylamide molecules. At this close distance, double bonds are broken and molecular units of acrylamide connect to each other by single covalent bond forming polyacrylamide. As the pressure is released, molecular units of the acrylamide find enough volume to reorient in such a way that higher fraction of polymer is formed during decompression. This is confirmed by the increase in the relative intensity of the C-H stretch mode on release of pressure.

Chapter 4: Hydrogen Bond Vs Ionic Form: Imidazole

The dynamics and mechanism of proton transfer [11] in the condensed phase are important for understanding of charge transfer processes and also for the development of electrolyte membranes in electrochemical devices such as fuel cells [12]. Imidazole which has a strong inter-molecular N-H- - -N hydrogen bond, close to the symmetrization limit, provides a model system for understanding proton transfer mechanisms under pressure [11]. In addition, imidazole also has C-H- - -X (X=N, π) interactions, which are known to play an important role in various biological processes. High pressure Raman spectroscopic studies supplemented by *ab-initio* calculations on imidazole ($C_3H_4N_2$) [13] were carried out up to ∼20 GPa. At pressures around ∼10 GPa, the reduction in the N- - -N distances to the symmetrization limit and the emergence of the new spectral features of the cationic form indicate the onset of proton disorder. The pressure induced strengthening of the 'blue shifting hydrogen bonds' such as C-H- - -X (X=N, π) in this compound is also revealed by the Raman spectra as well as *ab-initio* calculations. Results indicated that C-H- - -X (X= N, π) and N-H- - -N inter-molecular hydrogen bonding interactions largely influenced the nature of structural transformations in imidazole under pressure. No polymer phase of imidazole was noted under pressure or on release from the highest pressure of 20 GPa in this study [14]. This result is

in sharp contrast to the high pressure behavior of carnosine, where its constituent imidazole displays onset of polymeric transition at ∼2.8 GPa.

Inhibition of polymeric phase in imidazole is largely attributed to the competing N-H- - -N and C-H- - -X (X = N, π) interactions.

Chapter 5: Hydrogen Bond Vs Halogen Bond: Iodic Acid

Iodine based compounds are very important for laser, ferroelectric, piezoelectric and various other industrial applications [15–18]. Iodic acid, the simplest oxoiodate of iodine with the oxidation state V is an ideal system for studying the competing I- - -O halogen bond and O-H- - -O hydrogen bonding interactions. High pressure Raman and x-ray diffraction studies of iodic acid have been carried out up to ∼36 GPa and ∼23 GPa respectively at room temperature [19]. In addition to these, experimental results are also supplemented by *ab-initio* calculations.

At ∼0.4 GPa, enhanced interaction of iodine with the adjacent non-bonded oxygen atoms is indicated by Raman scattering and *ab-initio* studies. Pressure induced changes in the coordination is also indicated across this pressure. However, x-ray diffraction study does not show any change in the crystal symmetry up to the highest pressure. Several discontinuities in the frequency versus wavenumber of vibrational modes under pressure were also observed at higher pressures such as ∼5 GPa, ∼10 GPa which indicate structural modifications under pressure. The study of iodic acid under extreme conditions may be further explored to look for novel coordination compounds which may be exploited for advanced materials research applications.

Conclusion

Hydrogen bond plays an important role in the pressure induced variation in the structural, physical and chemical properties of the solids. In the case of deuterated α-glycine [9], the simplest amino acid, competing hydrogen bonding interactions result in subtle structural rearrangement through conformational changes rather than any modification in the crystal symmetry. While in imidazole, which is a hydrogen bonded heterocyclic aromatic compound, proton transfer through hydrogen bonds result in the ionic forms and inhibit polymerization

at high pressures [14]. In acrylamide, the modifications in the hydrogen bonding network assist in the structural transition and subsequent polymerization [10]. Also, hydrogen bond plays an important role in the formation of non-bonded co-ordination compound in iodic acid under pressure [19].

Future Prospects

This doctoral thesis helps in understanding the role of hydrogen bonding interaction in the structural and polymeric transitions in some solids under pressure. Also, the results obtained may be exploited for exploring novel hydrogen bonded supramolecular and other technological materials.

Contents

List of Figures

List of Tables

1

Chapter 1

Introduction to Hydrogen Bond and High Pressure

1.1   Significance of Hydrogen Bond

"Life would be impossible without hydrogen bond..."

Importance of hydrogen bond is widely recognized in biology, chemistry, materials science and physics *etc.*, Hydrogen bond is an ubiquitous interaction found in many important compounds in the nature and is one of the important mediator of life on the earth. All animals, plants are made of protein, cellulose *etc.*, which contain hydrogen bonds of various strengths. The DNA molecule is made up of two polynucleotide strands tangled together to form a long double helical structure. This helical structure is very stable because polynucleotide strands are held together by a series of hydrogen bonds. At room temperature, water (H_2O) is liquid but hydrogen sulphide (H_2S) is a gas. This remarkable difference is due to hydrogen bonds in water. Recently, supra-molecular chemistry, mediated through hydrogen bonds have been broadly applied to crystal engineering, molecular analysis, and catalysis applications. These are few interesting examples which has made the hydrogen bond a fascinating field of research. In this chapter, I shall discuss the basic concepts, experimental techniques and relevance of high pressure research of hydrogen bond.

1.2   Definition and History of Hydrogen Bond

'Hydrogen bonding is a donor-acceptor interaction specifically involving hydrogen atom' [22]. A situation when a hydrogen atom is simultaneously binding to two other atoms where one is donor (A) and the other is acceptor (B), is known as hydrogen bond (A-H- - -B). Donor is generally more electronegative compared to hydrogen atom so it partially withdraws the electron charges from the covalent A-H bond towards it, makes hydrogen atom 'unshielded'. This partially unshielded hydrogen atom interacts with the acceptor atom B. To facilitate bonding, B should have a lone pair of electrons or π electron cloud. Popular classification of hydrogen bond is based on the bond energy. Strength of hydrogen bond vary from 0.5 to 40 Kcal/mol broadly depending upon the electro-negativity of interacting atoms. Hydrogen bond strength is closer to the covalent bond at higher energy side, and van der Waals interaction towards lower energy side. Though hydrogen bond is strong enough to hold A- - -B atoms together in a specific direction at the room temperature, in some situations such as in water it becomes weak enough to allow independent directional movements in bond. O-H- - -O$^-$, O$^+$-H- - -O, N$^+$-H- - -N, N-H- - -N$^-$ and (F-H- - -F)$^-$ bonds often give rise to strong hydrogen bonds. In a symmetric hydrogen bond, energy exceeds $\sim$12 Kcal/mol and hydrogen atom is found at symmetric position relative to donor and acceptor atoms [22]. Moderate hydrogen bonds (energy between 3 Kcal/mol - 12 Kcal/mol) are formed between neutral donor group and neutral atom containing lone pair of electrons, for example are N-H- - -O, O-H- - -O $etc.$. Weak hydrogen bonds have energy less than 3 kcal/mol and typical examples are C-H- - -N,C-H- - -O, C-H- - -π $etc.$. Hydrogen bonds with donor-acceptor distances of 2.2 - 2.5 Å are characterized as 'strong', 2.5 - 3.2 Å as 'moderate' and 3.2 - 4.0 Å as 'weak' [22].

History of hydrogen bonds start with the discovery of an interaction, which was claimed by W. M. Latimer and W. H. Rodebush in 1920 [23]. Later Linus Pouling extended the concept of hydrogen bond in valence bond theory and hydrogen bond became popular. He described hydrogen bond as a bond where hydrogen atom acts as a bond between two atoms [24]. This 'bond' is strong enough to keep constituent atoms directional and stable.

But to accommodate the very nature of 'bond' for weaker hydrogen bond where there are no specific directions, the definition of hydrogen bond is modified by the IUPAC in 2011 as following:

"The hydrogen bond is an attractive interaction between a hydrogen atom from a molecule or a molecular fragment X-H in which X is more electronegative than H, and an atom or a group of atoms in the same or a different molecule, in which there is evidence of bond formation [25]."

1.2.1   Special Nature of Hydrogen Bonds and Theoretical Model

There are three parameters which are used to define a hydrogen bond. They are angle (δ) of $\angle$ A-H- - -B, A-H covalent bond length (r) and distance (R) between A and B as shown in the figure 1.1. Hydrogen bond does not always exist in a simple linear A-H- - -B form. It may be found in the bent, bifurcated and multicentre forms also. When a hydrogen atom is attached to two acceptors atoms, then it is called two centre hydrogen bond. Two centres may be replaced with three centres also. Multi center hydrogen bonds are mostly found as moderate hydrogen bond. If two hydrogen atoms are attached to one acceptor, it is described as bifurcated hydrogen bond. Multi-centre and bifurcated hydrogen bonds are shown in the figure 1.1.

If hydrogen bond, formed between two molecules alters the ability of adjacent molecules for making further hydrogen bonding by charge redistribution, then it is known as cooperative hydrogen bond. For example, as shown in figure 1.2 for water (H_2O), formation of one hydrogen bond changes the distribution of electron density on the acceptor (oxygen atom). Because of this, ability to form to new hydrogen bond arises. This is why water has two hydrogen bonds (as acceptor) while hydrogen sulphide (H_2S) has only one hydrogen bond. This extra hydrogen bond strength forces water to be liquid at room temperature while hydrogen sulphide is a gas.

A simplified theoretical model for the hydrogen bond is given in the literature [26]. For a theoretical model, several approximations are assumed. As for potential equation (V_1), A-B
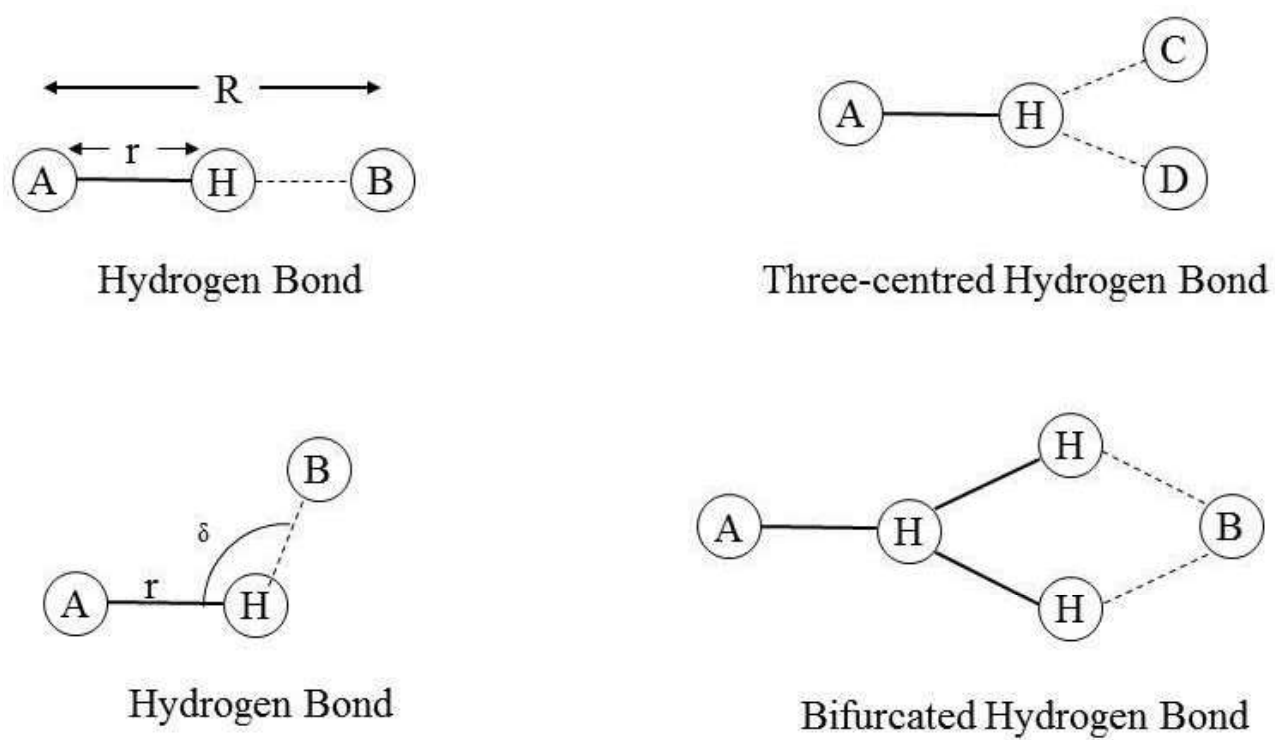
Figure 1.1: Different types of hydrogen bonds

Co-operative Hydrogen bond in water
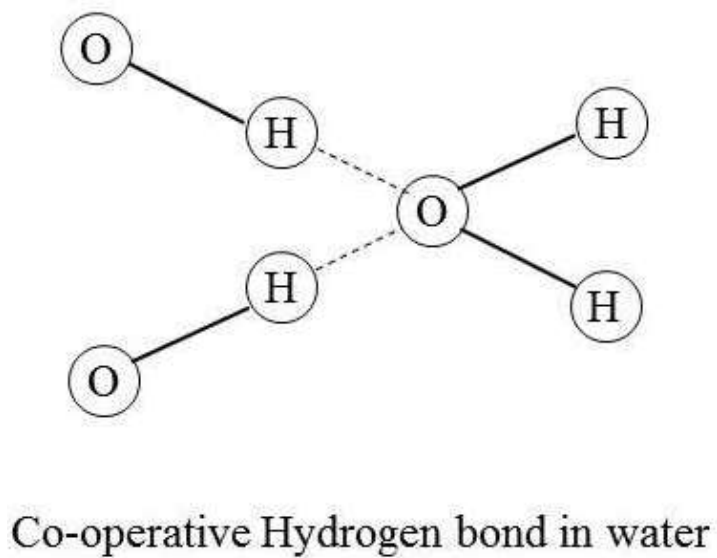
Figure 1.2: Co-operative hydrogen bond

interaction is approximated by the Morse potential of covalent bond

$$V_1 = D(1 - exp(-n\Delta r^2/2r))$$

Here $\Delta r = r - r_0$ (r_0 is the equilibrium position of A-H bond), D is the dissociation energy of covalent bond and n is a constant value.

Similarly, potential interaction (V_2) between H- - -B may be written as an approximation of covalent bonding. Here the bond length is written as (R-r-r_0^*) and D^* is dissociation energy of the bond while n^* is the constant value.

$$V_2 = D^*(1 - exp(-n^*(R - r - r_0^*)^2/2(R - r))$$

There exists van der Waal attraction and electrostatic potential between A and B.

van der Waal repulsion is expressed as the function below, where b is a constant

$$V_3 = Kexp^{-bR}$$

and electrostatic repulsion between A and B is expressed as

$$V_4 = -\frac{K}{R^m}$$

Total approximate potential function (V) for the hydrogen bond may be written as the sum of all the potentials as following

$$V = V_1 + V_2 + V_3 + V_4$$

Hydrogen bond potential in one dimension is plotted in the figure 1.3. With the advancement of computational power and invention of new methods such as Density Functional Theory (DFT), theoretical methods are now popular and more accurate to calculate the properties of hydrogen bond. Though the overall effect of hydrogen bond on the intermolecular inter-
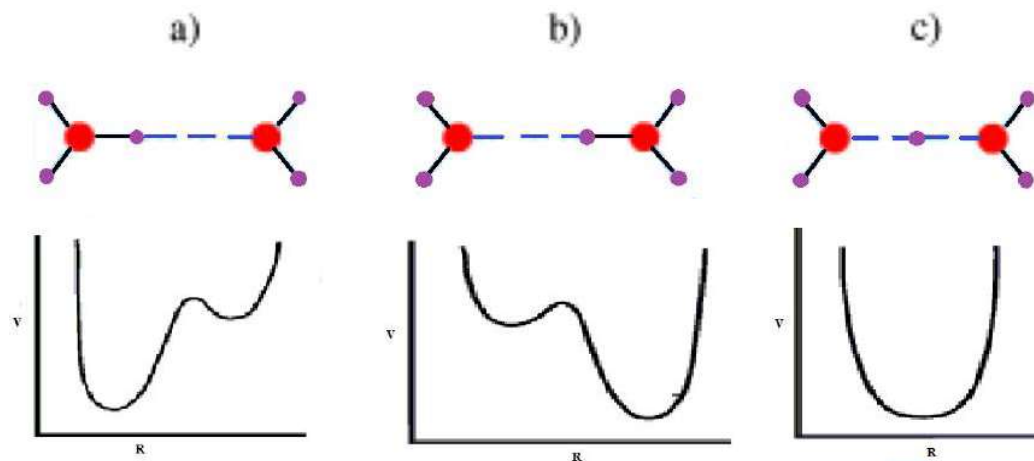
Figure 1.3: One dimensional potential for Hydrogen bond: (a) A-H- - -B, (b) A- - -H-B, (c) A- - -H- - -B

actions is yet to be formulated in theory [27]. Many computer programs are available and these are being used to explain many new phenomena [28, 29].

1.3 Introduction to Pressure

The state of a thermodynamical system is expressed as a function of thermodynamical variables, pressure (P), temperature (T) and volume (V). Equation of state for any system is defined as following:

$$f(P, V, T) = 0$$

In equilibrium, system stays in the energy minima created by the thermodynamical variables and any change may force it to change the structure or configuration, transforming it to a new state having different energy with altogether new properties. This transition from one state to an other is described as 'phase transition'.

1.4 Pressure as Variable

Pressure, as a thermodynamical variable, is a versatile parameter, can be employed alone or with the combination of other variables such as temperature and/or magnetic field *etc.* Pressure is in fact more effective and refined parameter [30] for study because it can vary in large order of magnitude starting from 10^{-30} to 10^{30}. Unit cell under pressure can easily be compressed to half of its initial volume which is very significant compared to the effect of other parameters. While temperature only puts the system into ground state and change the volume of unit cell by only a fraction, in contrast, pressure can 'reshape' the inter-atomic potentials between the atoms. As of now, materials can be compressed to such a great extent that basic interaction between atoms can be altered to resulting in drastic changes, for example, formation of graphite or diamond is possible from same carbon atoms by applying different pressure and temperature environment.

For any system in equilibrium, Gibbs free energy (G) is minimum. Gibbs free energy relates to the enthalpy H, temperature T and entropy S by following relation:

$$G = H - TS$$

$$dG = V dP - S dT$$

Static high pressure experiments are isothermal so dT=0.

So the thermodynamical volume is related to the Gibb's free energy (G) with pressure derivative. This explains why there is a reduction in volume with increasing pressure.

$$V = \frac{dG}{dP}$$

Phase is defined as a definite state of the system. If there is a discontinuous change in any of properties such as volume, symmetry *etc.* then system is said to have changed the phase. In materials, phase transition is often seen through the changes in the structure, in the atomic arrangement and in bondings at molecular level. When a material is compressed, constituent

atomic or molecular units move closer to each other until the electrostatic repulsion is strong enough to resist. This steric limit often decides the phase transition point and pressure is generally used to explore the new phases of system or to investigate system stability. There may be changes in the inherent properties of the sample and new phases of the system may have novel properties of electronic, structural or superconductive importance.

If there exists another phase of the system that has the free energy minima with a different volume, then the system will transform to that phase with a volume change, provided that there is enough energy to crossover the barrier. If there is a discontinuous change in the volume of unit cell and discontinuity in the first derivative of the Gibb's free energy exists, the observed phase transition is said to be of the first order. Not only the final phase but the transition path is also very important. In the first order phase transition, co-existence of the multiple phases is also possible because of the kinetic barrier which exists in the path. There may be the possibility of system going to new state where Gibb's energy is not at global minima, such a state is called a meta-stable state. Diamond is a classic example of meta-stable state of carbon which form graphite when subjected to high pressure and temperature conditions. If the second derivative of Gibb's free energy, for example, specific heat is discontinuous, then the transition is said to be of second order. Free energy of the system with pressure in event of phase transition is shown in the figure 1.4.

Pressure induced phase transitions are of three types: re-constructive, order-disorder and displacive. Re-constructive phase transition involves breaking and rejoining of bonds across the transition. There may be changes in the topology of bonds after phase transition. Secondly, order-disorder phase transition involves either sluggish substitution where new and old phases are having close relationship or change in the orientation of atoms by small amount without changing the fundamental bonding. As there is no long distance movement, transitions are fast. In displacive phase transition, atoms are moved from one position to other without breaking the existing bonds. If bonds are not broken across the transition then this type of movement needs to have same order of time period as of phonons. Because atoms move in the gradual manner so the symmetry of crystal breaks at the transition point. Most
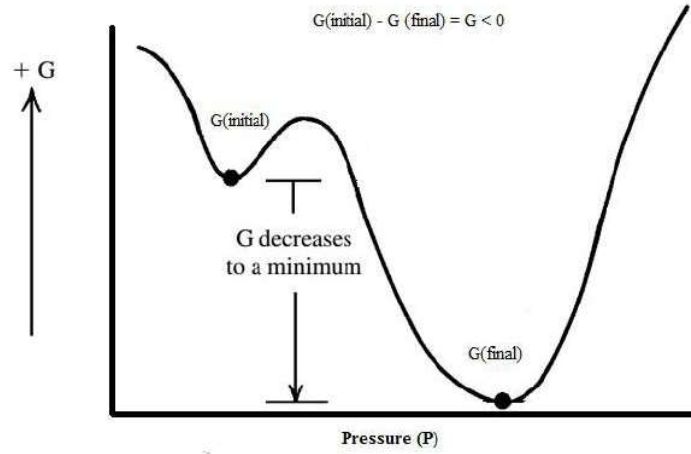
Figure 1.4: Change in the free energy during phase transition

of the transitions under pressure are of displacive in nature as inter-atomic repulsion exists between the atoms. In displacive transition one to one correspondences can be established between the initial and final phases.

1.4.1 Pressure measuring units

Pressure P, a scalar quantity relates the amount of force ($\vec{F}$) on an area ($\vec{A}$). Equation for the pressure is written as:

$$P = \frac{\vec{F}}{\vec{A}}$$

A second rank stress tensor (σ) represents the force acting along the different directions. Application of stress produces the strain (ϵ) which is also a second rank tensor, in all three directions. Relationship between the stress and strain is given as following:

$$\epsilon_{ij} = S_{ijkl}\sigma_{kl}$$

Here S_{ijkl} is elastic modulus tensor. Stress tensor (σ) can be written in the matrix form as following:

$$\begin{pmatrix} \sigma_{11} & \sigma_{12} & \sigma_{13} \\ \sigma_{21} & \sigma_{22} & \sigma_{23} \\ \sigma_{31} & \sigma_{32} & \sigma_{33} \end{pmatrix}$$

Application of stress gives rise to different strain along different directions except for cubic structure wher is is equal in all three directions due to symmetry. Diagonal elements of stress tensor are called normal stress and the off-diagonal elements constitute shear stress. For hydrostatic stress, off-diagonal elements are zero and only diagonal elements exist with equal values.

For hydrostatic pressure $\sigma_{ij} = 0$, where i $\neq$ j. So,

$$\sigma_{11} = \sigma_{22} = \sigma_{33}$$

Pressure (P) relates to the stress tensor (σ)

$$P = \frac{1}{3}[\sigma_{11} + \sigma_{22} + \sigma_{33}]$$

This condition can be obtained in a liquid medium where shear stress is zero. Only few liquids indeed can be used as pressure transmitting medium for the generation of hydrostatic pressure conditions. As the medium solidify, off diagonal elements of stress tensor becomes non-zero and the hydrostatic conditions are lost.

When a material is subject to stress, changes in the volume is related to the stress tensor as following:

$$\frac{\Delta V}{V} = \Sigma\epsilon_{ii} = \sigma\Sigma S_{iikk}$$

Where S_{iikk} is an isothermal volume compressibility.

Isothermal bulk modulus in terms of elastic modulus tensor can be written as

$$K = (S_{11} + S_{22} + S_{33} + 2S_{12} + 2S_{13} + S_{23})^{-1}$$

If the trace elements of stress for non hydrostatic pressure are $[\sigma_1\sigma_2\sigma_3]$ then radial stress

$$P = \frac{2\sigma_1 + \sigma_3}{3}$$

and axial stress

$$t = \sigma_1 - \sigma_3$$

For high pressure experiments, axial stress effect on materials is explained by A. K. Singh *et. al.* [31].

For high pressure experiments bulk modulus is related to the change in volume of unit cell as following:

$$K = -V\frac{\partial P}{\partial V}$$

To measure the pressure on sample, first and second derivative of bulk modulus are also derived at ambient conditions:

$$K' = \frac{\partial K}{\partial P}$$

$$K'' = \frac{\partial^2 K}{\partial^2 P}$$

These values can be substituted in the equation of state for measurement of pressure [32–34]. To measure the pressure various common units are frequently used. These units are interrelated to each other as shown in the table 1.1.

1.4.2   Wide Range of Pressure in Nature

In the universe, pressure is found on a very diverse scale. Different scales of pressure are relevant for the different branches of sciences. While inside the neutron stars, pressure is of the order of 10^{35} Pa, it is of the order of 10^{-15} Pa in intergalactic space. Inside the black hole it is assumed that even higher order pressure exists. Typical pressure scale that exists in the universe is shown in the figure 1.5.

For biological systems, upper limit of pressure is generally 1 GPa and for material chem-

	Pascal (Pa)	Bar	atmosphere	Torr.	Pounds per square inch (psi)
1Pa	1 N/m^2	10^{-5}	7.5006×10^{-3}	1.4503×10^{-4}	
1 bar	10^{5}	1.0197	0.9869	750.06	14.5037
1 atm.	1.0132×10^{5}	1.0132	1	760	14.6959
133.322	1.3332×10^{-3}	$\frac{1}{760} = 1.3157 \times 10^{-3}$	1 torr	1 mmHg	1.9336×10^{-2}
1 psi	6.8948×10^{3}	6.8948×10^{-2}	6.8046×10^{-2}	51.7149	$1 \text{ lbf }/\text{in}^2$

Table 1.1: Relation between different pressure measuring units

istry and physics it is of the order of tera pascal. The existence of diverse materials on earth such as coal, diamond *etc.* are due to the different ranges of pressure. Coals are remains of plants that lived millions of years ago, subjected to various high pressure and temperature conditions. Similarly, petroleum is made of remains of millions of tiny plants and animals that once lived. When they died, their bodies sank under the sea bed and bacteria attacked the dead remains to change them into oil under high pressure and temperature. Formation of diamond, as a carbon allotrope, is also the result of combination of high pressure ($\sim$15 GPa) and temperature ($\sim$ 1500ºC) that exists inside the earth. Our earth is divided into the layers of core, mantle and crust. Core, which is the innermost part of the earth where materials remain under very high pressure and temperature conditions. Here materials such as iron, nickel *etc.* behave differently from their normal ambient properties.

1.5 High Pressure Materials Research

High pressure research has received much of the attention due to promising materials research and application utility. Investigation of the properties of materials which reside deep within our earth or other heavenly bodies, synthesis of novel and useful materials not readily available by other means, study of pressure effect on living organisms and exploring of the
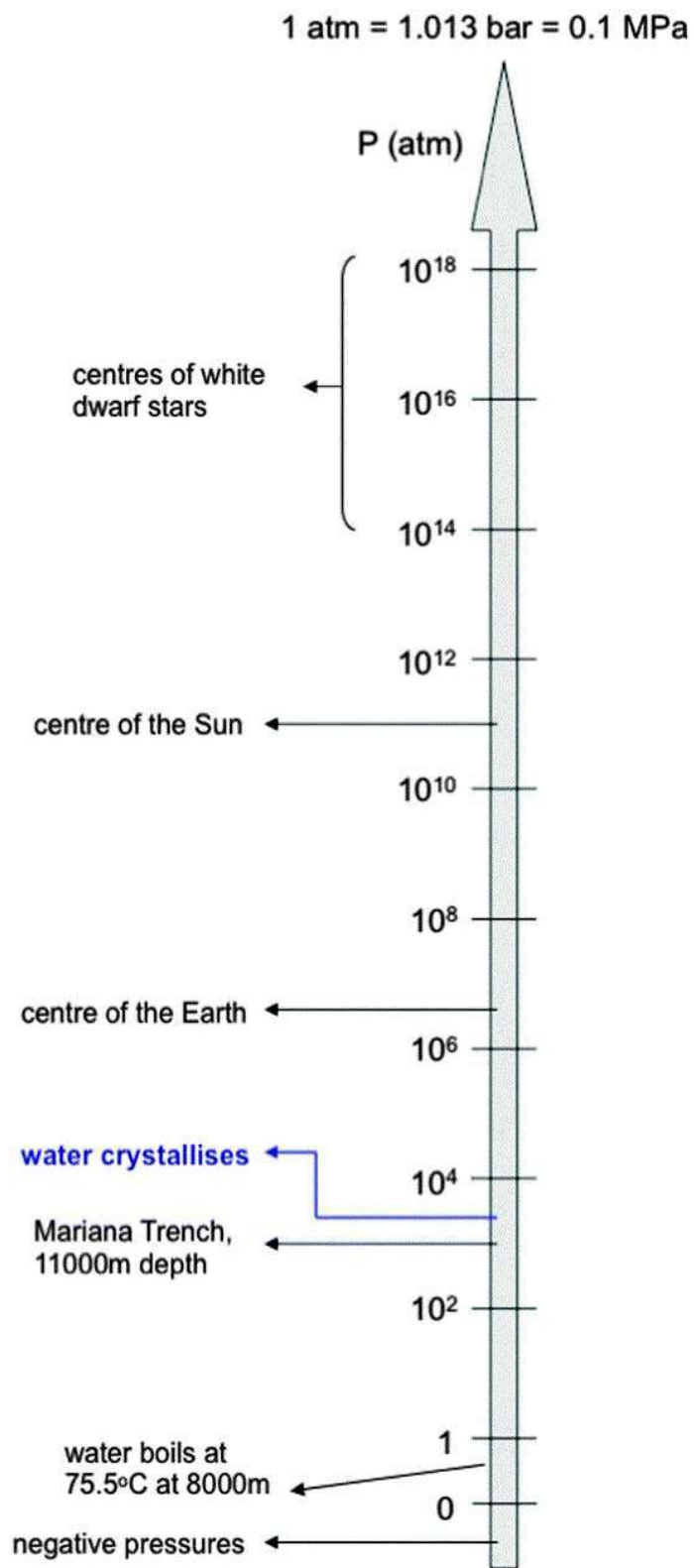
Figure 1.5: Pressure ranges found in the nature

conditions favorable for the origin of life itself are few important areas of current research.

In a laboratory, pressure ranging from few bars to mega-bars (1 bar or 100,000 Pa) can be generated easily. Theoretically it has been predicted that maximum pressure of approximately 5 Megabar can be sustained by the diamonds without breaking, as above this pressure, the structure of diamond is said to become unstable [35]. Jian Sun *et. al.* has described the upper limit of pressure 2.5 terapascal at 300 K [36]. But the maximum static pressure achieved by any laboratory till date is ~770 GPa [37]. As the maximum pressure limit is increasing, new applications of pressure in materials science, geophysics, astrophysics and biology are also being explored. [38,39].

Matter is made of atoms which are connected to each other by different types of interactions such as covalent, ionic, hydrogen-bonding, metallic or van der Waals. Properties of materials are predominantly determined by these inter-atomic interactions. By varying pressure, we can tune the inter atomic distances between molecular units. As atoms move closer, overlap of electronic charge density between them increases which results changes in the electronic, optic and mechanical properties. Also, during rearrangement of molecular units under pressure, breaking and formation of bonds are possible and this may lead to the formation of new crystal structure with different properties and symmetry altogether. There are several hypothesis to explain the mechanism of phase transition out of which minimization of Ehrenfest free energy [40] and Landau free energy theories are frequently used. Several new structures of various materials have been retrieved with properties very different from their known ambient properties. High temperature superconducting phase of hydrogen sulphide [41] is recently discovered under pressure. Different from chemical route, high pressure is a novel method for polymerization/amorphization by which various materials such as acetylene [42], benzene [43] are polymerized. Pressure induced metallization of hydrogen is promising field of basic science [44,45]. It is reported that hydrogen gas becomes metal at room temperature under high pressure [46,47]. Ashok Kumar *et. al.* has recently calculated the metallization pressure of ZrX_2 (X = S, Se, Te).

The development of technologically advanced materials, alloys, ceramics, intermetallics

or composites are key areas for research. Pressure is frequently employed along with the temperature ranging from few milli-kelvin to thousands kelvin. High pressure and high temperature conditions are employed to generate the planetary conditions in the laboratory [48–50]. In the laboratory high temperature under pressure is generated by two methods, one by Laser Heated Diamond Anvil Cell (LHDAC) [51] where the temperature is measured by the optical pyrometer and other is heating by resistant wire. Localized high temperature (few thousand kelvin) can be achieved by the LHDAC, while resistant heating gives large area heating but comparable low temperature ($\sim$1000°C [52]). Resistant heating is affected by the graphitisation of diamond above 800°C under high pressure. Measurements from Z. Jenei *et. al.* have shown that high temperature up to 1200°C may be achieved with resistant heating [53–55]. Using LHDAC, temperature of the range of 6400° C is already achieved and combined with the pressure range of $\sim$200 GPa [56]. But, high temperature by LHDAC can only be sustained for few micro seconds while it can be maintained for long time in the resistant heating. Laser shock and projectile may also be employed for the adiabatic high pressure generation for terapascal pressure range.

Electrical resistivity of materials, which is an intrinsic property determined primarily by the interaction strength between electrons and phonons, can be explored under pressure. Lanzilo *et. al.* has investigated copper and alumunium under pressure to find the relationship between phonon and resistivity up to 2 GPa [57]. These studies on copper and aluminum show how phonons can be modeled through strain/pressure to achieve special electrical properties that has applications in modern integrated circuits. Dielectric and optical properties under pressure are of special interest because of their technological relevance. Ding Pan *et. al.* has calculated the dielectric constant of water under pressure to simulate the geological conditions [58]. For these measurements low temperature is required under pressure. Liquid nitrogen or helium are used to generate milli kelvin temperature. Tunning of pressure along with temperature opens up the possibility of exploring superconductivity and other applications such as Karr effect [59], magneto-resistant [60], de-Has Van Alphen effect [61] and NMR [62]. High pressure is also coupled with low temperature and high

magnetic field. To generate high pressure in magnetic field, Cu-Be magnetic cell is used. Cu-Be cell being the non-magnetic so does not interfere with the magnetic measurement of the sample. SQUID for magnetic measurements has already been used upto 5 GPa with 20 Tesla magnetic field till date [63, 64].

Neutron diffraction is carried out using the thermal neutrons of energy ∼0.025 meV. Neutron diffraction has an advantage of locating low atomic number materials under pressure. As neutron also interacts with atoms magnetically, magnetic studies are also possible by neutron diffraction but neutrons are only available at nuclear reactors or spallation sources and because of neutral nature, it is very difficult to focus neutrons on a small size of sample under pressure. Hence large anvil piston-cylinder are preferred device for high pressure neutron based experiments. Recently many studies have been done on the powder and single crystal neutron diffraction up to high pressure [65–67]. Kermarrec *et. al.* has investigated the frustrated rare-earth pyrochlore magnet $Yb_2Ti_2O_7$ which exhibits a classical spin liquid state with fractionalized thermal excitations under pressure and found magnetic transition from a disordered, non-magnetic, ground state to ferromagnetic ground state [68]. Network structure found in many glassy materials and liquids are recent research front of neutron diffraction under pressure [69].

High pressure x-ray diffraction is a preferred way to investigate the materials because it is not limited by the flux availability or focusing limitations like neutron diffraction. High intensity and high energy fourth generation synchrotron sources have made the measurements very easy. X-ray interacts with the atom through electronic charge so the location of low atomic number becomes very difficult. But recently M. Woinska *et. al.* has improved the x-ray diffraction accuracy for hydrogen atom up to 0.8 Å using Hirshfeld atom refinement method [70].

Most of the life on earth exists under one atmospheric pressure. But few organisms are found to survive in deep geological conditions at higher pressure. There have been efforts to explore life on the heavenly bodies at different pressure ranges. Recently a amino acid, glycine, a building block of protein, is found by NASA spacecraft 'Stardust'. High pressure

effect on protein structure is interesting from the point of view of biology as well as studying the macromolecule dynamics [71]. For enzyme reactions, the pressure dependence can explore enzyme mechanisms or the new path of their function. In addition, high pressure sterilizing techniques are also being used to keep food fresh for long time. Phil M. Onger *et. al.* have discussed the microbiological activities under high pressure conditions [72].

1.6 Overview of Hydrogen Bonded Materials Research Under Pressure

Hydrogen bond is integral part of the many molecular systems. Generally, energy associated with hydrogen bond is significantly small compared to ionic or covalent bonds. So, small changes in pressure can generate large changes in the hydrogen bond parameters compared to ionic or covalent bonds. High pressure studies of hydrogen bonded systems are done to study the response of a materials under pressure and also to solve the problems related to polymorphism, materials science, structural properties correlations, compressibility, isotope substitution effect and reactivity. A good review of hydrogen bond under pressure is given in article by Sikka [7]. Experimental techniques such as Raman, IR, NMR, powder, single crystal x-ray and neutron diffraction are used to investigate hydrogen bonded systems up to very high pressures [65–67].

Pressure can change the geometry of hydrogen bond drastically [73–79] and so the compressibility of system. Compressibility of hydrogen bond also depends upon the structure in which atoms are arranged as an example O-H- - -O hydrogen bonds has different compressibility in chain/layer structure [74,75,77] compared to spiral structures [76,80]. Strong negative linear compressibility is also observed in $Na(NH_2BH_3)$ because of hydrogen bond [81]. As a good example, nylon-6, compressibility is four times larger in the direction normal to the hydrogen-bonded sheet than in parallel direction [82]. In paracetamol, two types of hydrogen bond N-H- - -O and O-H- - -O exist in the two dimensional structure. With pressure, monoclinic paracetamol expand on increasing pressure along the chains linked by the N-H-

- -O hydrogen bonds, and it compressed along the chains linked by the O-H- - -O hydrogen bonds [83, 84].

Three polymorphs of Glycine α, β and γ, where α polymorph is found to be stable under pressure but γ polymorphs shows phase transition at $\sim$3 GPa [85]. This ability of few polymorphs to resist pressure largely depends upon the hydrogen bond network in the system. Similarly, no polymorphic transformations for paracetamol, but only a reversible anisotropic structural distortion was observed for the single crystal of the monoclinic polymorph (P2$_1$/n) pressure till 5 GPa [86], but for powder samples, same polymorph, however shows, an irreversible partial transformation into the orthorhombic below 2 GPa [86]. Pressure-induced phase transitions in the molecular crystals with hydrogen bonds can generate rotation, polarization of hydrogen bonds and make possible migration of protons from one atom to another. The same effect also accounts for the pressure-induced hydrogen bond assisted amorphization. [6, 9, 14, 87].

Hydrogen bonded materials also represent the technologically important class of materials. High-pressure behaviour of hydrogen-bonded energetic material *ex.* carbohydrazide (CON$_4$H$_6$, CHZ) shows phase transition across $\sim$ 8-10 GPa and the resultant phase is found to be the 23.1% denser [88]. In cyano-acetohydrazide, pressure induced changes occur near 22 GPa and the drastic changes in the optical properties were found [89]. Multidimensional metal-organic frameworks constructed by hydrogen bonds constitute a latest class of materials which are currently very interesting in various areas such as supramolecular chemistry, materials science, crystal engineering, catalysis, molecular magnetism [90–94]. Shyamapada Nandi *et. al* has reported that the hydrogen bonded framework formed by a single tripodal tricarboxylic acid molecule can be used for the selective capture of CO$_2$ [95]. These kinds of permanent porous networks can be efficiently applied to remove CO$_2$ from an environment. It may be helpful to combat the adverse climate change in recent times. Studies by Jia Tian *et. al.* on supramolecular metal-organic frameworks found high homogeneous and heterogeneous photocatalytic activity for H$_2$ production [96].

Symmetrization of hydrogen bond under pressure is an important problem to be probed.

Hydrogen bonds near symmetrization limit are important for understanding proton dynamics in various biological and geological processes in nature and have special effects on the properties of bonding [97]. Ice phase 'X' [98] has been the well-known topic in high pressure science [99–102] but now many new compounds with symmetrization are being discovered under pressure.

1.7   Experimental Methods to Probe Hydrogen Bond

Hydrogen bond is probed by several methods of spectroscopy and diffraction. Spectroscopic methods investigate the specific bond nature while diffraction methods such as x-ray and neutron are used to identify the positions of atoms. A brief description of spectroscopic and diffraction methods is as follows:

1.7.1   Spectroscopic Methods

A first-hand information on the hydrogen bonding interaction can be obtained with the help of spectroscopic methods. Because of the formation of hydrogen bond (A-H- - -B), covalent bond A-H generally gets elongated so the red-shift in stretching frequency is observed. Though examples of blue shifting or shortening of the covalent bond also exists. Substituting the hydrogen atom by an isotope deuterium also shifts the frequency, popularly known as Ubbelohde effect [103, 104], can also be studied through spectroscopy. All these properties of hydrogen bond will be discussed in subsequent chapters.

Spectroscopic methods of Raman scattering and IR absorption are widely employed to probe the hydrogen bond, as hydrogen, a low atomic number element, is difficult to be located by the x-ray diffraction method. IR spectroscopic methods require special sample preparation, Raman which needs no special sample preparation. Raman and IR are complementary investigation tools but Raman is more convenient to use in in-situ biological samples because ubiquitous water has relatively low intensity Raman modes. Spectroscopic methods are useful not only for static experiments but also to study the dynamics of the

system [105]. In addition, chemical analysis can also be done easily by the spectroscopic methods. Because of portable and fast tool, spectroscopic methods are preferred in many fields of physics, chemistry and material science [106–108].

Raman spectroscopy involves the inelastic scattering of incident light. When light is made incident on molecule, molecule excitation or de-excitation may happen passing through the virtual states. The difference of energy in incident and scattered light is called Raman shift and it is indication of phonon energy shift. As merely change of energy happens here instead of energy absorption so Raman spectroscopy can be employed from entire range of visible to UV radiation. Strength of Raman signals depends upon the change in the strength of polarizability (α) of bonds, hence the bond formed with the more polar donor (ex. Oxygen) is less Raman intense compare of the bonding formed between the relatively less polar atoms (ex. Carbon). Where-ever there is structural, chemical or conformational changes in system, corresponding changes are easily seen through the Raman spectra [9, 10, 14, 106–109]. More elaborate discussion on Raman spectroscopy is done in Chapter 2.

Infra-red (IR) spectroscopy involves the transition between two vibrational states. So the use of infra-red radiation is necessary. The permanent dipole moment is required in the molecule for IR spectra [110]. Specific sample preparation and optics are also required for the detection of IR spectra. O-H, N-H type bonds where inherent dipole moment is very strong, IR gives very strong signal in comparison to the Raman spectroscopy [111–114].

NMR spectroscopy probes resonance between incident energy radiation and energy levels of the nucleus. Magnetic moment of nucleus is affected by the field produced in the environment. This produces shift in the energy levels and corresponding resonance frequency of nucleus is changed which is known as the *'chemical shift'*. In hydrogen bond, proton (hydrogen atom's) chemical shift is detected and the changes in hydrogen bond are determined accordingly [115, 116].

Inelastic scattering of neutron involves interaction with thermal neutron of energy 0.025 eV which exchange energy with the system. As neutron interacts with nuclear cross section rather than electronic charge density, potential energy surface of proton (H) can be easily

determined by neutron inelastic scattering. Using neutron scattering, full Brillouin zone curve of phonons (both acoustic and optic, in full Brillouin zone) can be determined in contrast to Raman where only Brillouin zone center phonon can be detected due to the restriction of selection rule ($k - k' = 0$). But, neutron as a probe tool is available only at the nuclear reactors and spallation sources, so the use of neutron inelastic scattering is expensive and remains limited to certain places.

1.7.2 Diffraction Methods

Location of hydrogen atom is essential to study hydrogen bonds. Coupled with spectroscopic methods, structural investigation can give complete insight of the system. Two important methods, x-ray and neutron diffraction are employed to study the structure of materials. Both diffraction methods follow the basic Bragg's equation $2d\sin(\theta) = n\lambda$ which involves interference between diffracted photons/neutrons from different atomic planes, which in turn produces the Fourier map of atomic arrangement. While x-ray radiation interacts with the electronic charge density of the atoms, neutron interacts with the nuclear absorption cross section. For hydrogen atom, electron charge density is lowest so the position determination by the x-ray diffraction has limited accuracy in hydrogen bonds unless the incident intensity is extremely high as in the synchrotron sources [117, 118]. Hydrogen nuclear absorption cross section is quite large for neutrons so neutron diffraction is an ideal probing tool. But, the intensity of neutron flux is always a matter of concern. Also neutron being the neutral particle is very difficult to focus on the small volume of sample [119].

1.8 High Pressure Generation

There are two popular methods employed to generate high pressure. First is dynamic method and second is static method. Dynamic and static pressure are complementary to each other in various ways, while static pressure allows us to achieve static, isothermal, hydrostatic pressure, contrast to it dynamic pressure is an adiabatic, for short time interval (approx-

imately micro seconds) and non-hydrostatic. The simplest method of generating dynamic pressure is the use of explosives on the surface of materials. Shock wave because of the explosive, generate high pressure and temperature on the sample. One popular example of shock wave generation is during the explosion of fission or fusion nuclear devices. Other examples include the use of gas gun, laser implosion *etc.*. These methods are frequently employed in modern laboratories. Pressure of the range of terapascal (1000 GPa) is achieved by the dynamic methods [120, 121]. In my thesis, I have restricted myself to the study of materials under static pressure at room temperature only.

Since first half of the 20th century, vast improvements in high-pressure apparatus and measuring techniques has allowed high-pressure physics to reach new limits. First systematic static high pressure methods were started by Percy Williams Bridgman and he was awarded Nobel Prize for Physics in 1946 for his contributions in high pressure science and technology. Initial experiments by Bridgman were done for the electric resistant of germanium under quasi-hydrostatic condition [122–124]. These experiments were limited up to 10 GPa. In 1958, development of the Diamond Anvil Cell (DAC) revolutionized the high pressure science and extended the use of high pressure for spectroscopic and x-ray diffraction investigations. Use of metal gaskets [125] as the pressure chamber, Ruby fluorescence [126, 127] for pressure measurements and various pressure transmitting mediums [128–130] to generate the hydro-static conditions has helped further advancement of high pressure research. Highest pressure achieved through diamond anvil cell has regularly increased manifold since the development of earliest device [131]. Pressure up to ∼100 GPa is now commonly achieved by DAC in laboratories across the world while the highest pressure achieved so far is ∼770 GPa [37].

1.9   Static High Pressure Devices

1.9.1   Piston Cylinder, Bridgman, Toroid and Multi-Anvil Devices

Generation of static high pressure is based on the idea of simple piston cylinder device in different forms. The piston-cylinder apparatus is a solid media device, used for generating

High Pressure Device	Pressure Achived
Simple Piston Cylinder	5 GPa
Bridgeman Anvil Cell	10 GPa [132]
Toroid Anvil	8 GPa [133]
Diamond Anvil Cell (DAC)	770 GPa [37]
Multi Anvil Cell	9.3 GPa [134]

Table 1.2: High pressure devices and their pressure limit
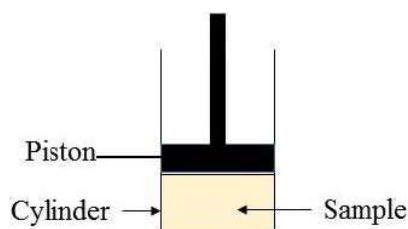
Figure 1.6: High Pressure Piston Cylinder Device

high pressure. It consists of a cylinder with one end closed and a movable piston at the other end as shown in the figure 1.6. Pressure generated is the ratio of force by the piston to area of the contact with cylinder. To generate high pressure either force has to be large or the area on which this force is applied should be small. Sample to be studied, is placed in the cylinder with pressure transmitting medium and pressed by the piston which is driven by the ram of a hydraulic press or manually operated. Usually steel, tungsten carbide are used to make piston and cylinder. Based on simple piston-cylinder concept, many types of refined press were invented. Few of them are still commonly used for high pressure generation such as Bridgman and Toroid anvil. Bridgman anvil consists two opposite truncated cones with a flat region between them to hold a pair of crushable gasket. The binding ring provides the external support to the piston. The main advantage of using the truncated cones is that when an axial force is applied, the strain distribution becomes reversed and higher pressure is generated. Toroid anvil is a modification of Bridgman anvil with the cupped type anvil
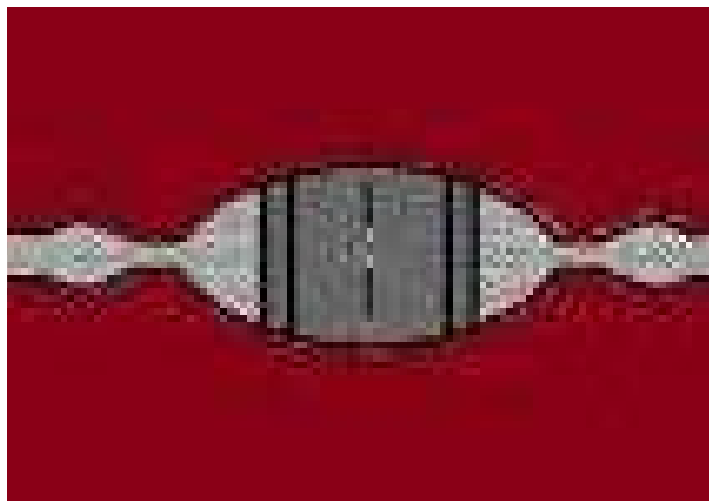
Figure 1.7: A toroid anvil

as shown in the figure 1.7. Toroid press has an advantage of employing large volume of sample which is a 'luxury' for high pressure experiments. But, the limiting factor on both of these anvils is the highest pressure (often upto $\sim$10 GPa) that could be achieved. Due to large size, these devices are also not fit for portable experiments. In addition to these difficulties, due to opaqueness for light, using high pressure techniques such as x-ray, Raman and IR experiments are also not possible. But these anvils are very useful in high pressure-high temperature material synthesis and resistivity experiments. Extension of Bridgman and Toroid anvils gave way to the development of multi-anvil apparatus and high pressure belt apparatus. These multi-anvil devices can press large volume of sample and also able to reach the high pressure compared to the Bridgman or Toroid anvils [134]. List for the highest pressure achieved by different types of devices is given in the table 1.2.

1.9.2   Development of Diamond Anvil Cell (DAC)

Development of Diamond Anvil Cell (DAC) has revolutionized high pressure research techniques [135, 136]. Diamond being the hardest material available in the nature, provides an extremely high static pressure range. Diamonds are cut from the tip in such way that the whole force is focused to the micron size area. DAC is also based on the principle of
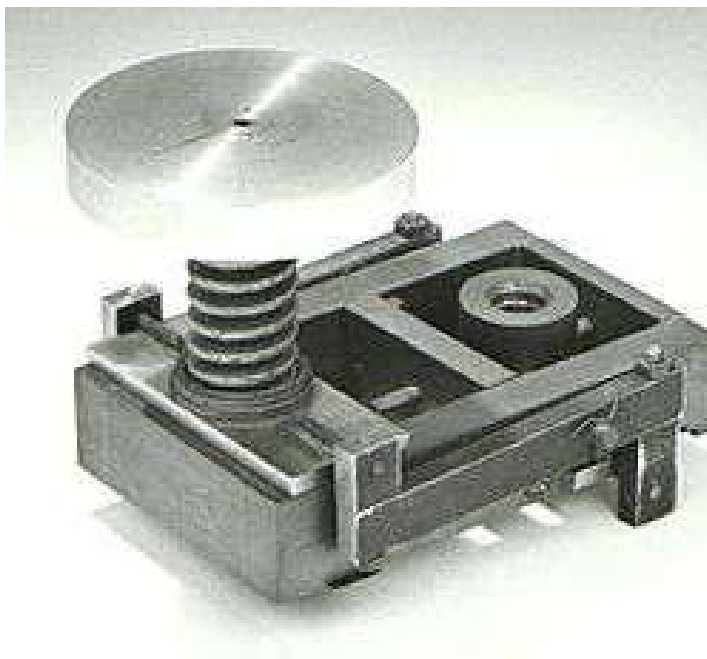
Figure 1.8: The first DAC: Source Wikipedia

piston cylinder device where one diamond is attached to the piston and other is attached with cylinder. Typical pressure generated in the laboratory is of the order of ∼100 GPa. Diamonds in the DAC may be replaced by synthetic diamonds as they are devoid of any impurities and imperfections which are commonly found in the natural diamonds. Recent study by employing the synthetic diamonds has achieved the pressure of ∼770 GPa [37]. With the order of this pressure range many geological processes can now be created in the laboratory, owing to the fact that pressure inside the core of earth is in the range of 360 GPa. DAC is portable and can be employed in several high pressure techniques. Also, it provides good optical window for x-ray and spectroscopic experiments such as Raman and infra-red. For experiments of resistivity or magnetic measurements new 'designer anvils' where anvil is itself embedded with the electric circuit, are used. But the limitation on the volume of sample which is of micron size and difficulty in the alignment inhibits or put restrain to the use of DAC. Notwithstanding the limiting factors, DAC is the most popular high pressure generating device presently and being increasingly employed around the world laboratories. The first DAC developed, is shown in the figure 1.8.
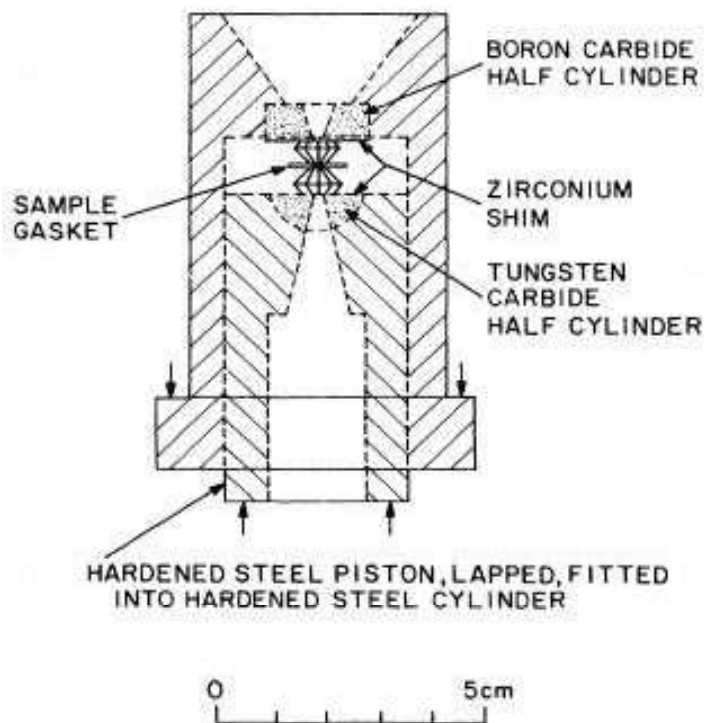
Figure 1.9: The basic design of DAC [20]

First use of diamond for pressure generation was done in 1950 by Lawson and Tang in University of Chicago. At that time the maximum pressure achieved by the cell was only up to 2 GPa. Currently used DAC are based on the design developed in 1959 by Weir, Lippincott, Van Valkenburg and Bunting at National Bureau of Standard [135]. Since then, many modification in DAC are done as per the requirements of the experiments. The basic design for DAC is shown in the figures 1.9.

1.9.3   High Pressure by DAC

For generation of high pressure, a pair of diamonds are mounted on the rocker and the backing plate respectively. A pre-indented gasket having a hole of ~60 micron, is kept between the diamonds as shown in the figure 1.11. This hole act as a sample chamber for the experiment. To generate the hydrostatic conditions generally liquid pressure transmitting medium and for measuring pressure, marker is kept along with the sample in the chamber. There are
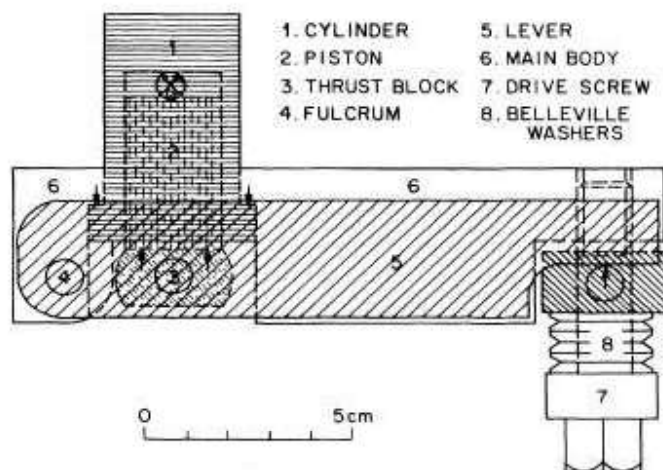
Figure 1.10: Design of a Mao-Bell cell [20]
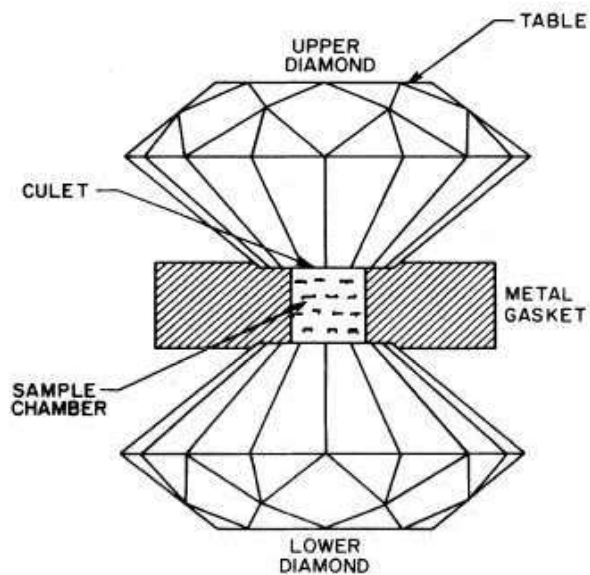
Figure 1.11: Diamonds with gasket for pressure generation [20]

several kinds of mechanical arrangements that are possible for pressure generation in a diamond anvil cell. Among them Mao-Bell [137], Merrill-Bassett [138], membrane cell [139] and Holzapfel [140] are the popular ones. I have used Mao-Bell type cells in all my studies. A basic design for the Mao-Bell cell is shown in the figure 1.10.

1.9.4 Diamonds for Pressure Generation

Diamond is the hardest known natural material. Though it is an allotrope of carbon but properties are very different from graphene and other allotrope. A particular arrangement of carbon atoms in the diamond unit cell gives it this unique property of hardness. It is transparent to the wide range of electromagnetic spectrum from x-ray, visible to infra red. Owing to this property, diamond is used for pressure generation in spectroscopic and x-ray diffraction experiments. However, not all diamonds can be used for all experiments. In natural diamonds, several kinds of impurities, such as Boron (B), Nitrogen (N) *etc.* are mixed during the geological formation process. Based on the existing impurities, use of diamond is determined for specific experimental requirements. Such as type I diamond, most abundant in nature, which contains nitrogen impurities are unsuitable for the high pressure infra-red experiments because of the nitrogen absorption bands. But these are extensively used for Raman experiments. Type II diamond are colorless pure natural diamonds do not have any impurity so used for all types of experiments. Due to the rareness, type II diamonds are expensive than Type I diamonds. Synthetic diamonds which are pure and defect free are increasingly used for very high pressure generation in the laboratory. Preparation of diamond for high pressure experiments require cutting of the diamond tip in to a particular shape a shown in the figure 1.11. Diamond can have 8 or 16 cut tip for the high pressure generation. Sixteen cut bevelled type diamond is widely used to achieve very high pressure.

1.9.5 Backing Plate and Rocker

For high pressure experiments, diamonds are mounted over backing plate and rocker, as shown in the figure 1.9. Backing plates and rocker are made of hardened steel or tungsten
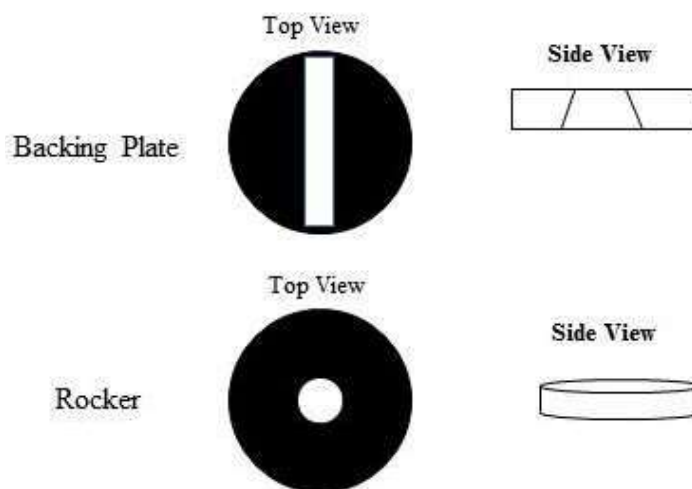
Figure 1.12: Rocker and backing plate

carbide to bear the high stress generated during the experiments. Geometrical designs for the backing plate and rocker are made in such a way that one can access the large *k-space* through the openings shown in figure 1.12. There are several designs available for backing plate and rocker. Recently, beryllium window which is transparent to x-ray is being increasingly used as rocker and backing plate for x-ray diffraction experiments. Diamonds are either glued or mechanically fixed by clamp ring over backing plate and rocker. For low temperature experiments, glue which can withstand the lowest temperature, is used.

1.9.6   Alignment of Diamonds

Diamonds are attached to rocker and backing plate as shown in figure 1.9. These diamonds need to be aligned parallel to each other for high pressure generation. Rocker and backing plate are attached to piston and cylinder respectively by the arrangement of screws. Rocker is moved to change tilt while backing plate is moved in XY direction. When diamonds on the anvil cell are not parallel then wage-shape/Newton's fringes appear that can be seen in the light, through vertically placed microscope. Using the tilt in rocker, Newton's fringes are made to disappear in order to make diamonds perfectly parallel. Diamond parallelism is

necessary to achieve very high pressure by DAC without breaking the diamonds.

1.9.7 Gasket

Gasket, a thin ($\sim$300 μ) metallic plate, is an important part of high pressure experiments. A metallic plain gasket is first put in between the diamonds and indentation is made. When the thickness of the gasket is reached $\sim$60 μm then a hole of $\sim$100 μm diameter (or typical 2/3 of the diameter of indentation) is made in the middle of the indentation as shown in the figure 1.13 and figure 1.14. This hole acts as a chamber for the sample, pressure transmitting medium and pressure marker. Pre-indentation pressing of gasket is necessary to stop the failure of gasket in experiments at high pressure. During the high pressure experiments at equilibrium, pressure from inside out is equal and opposite to the force generated from the friction. If the size of hole is too small or gasket is very thin than the force from inside toward out would not cancel the force from outside to inside causing gasket hole to collapse. In this case high pressure can be generated on the sample in small volume. If the gasket is too thick, then force from inside to outside will be greater than force from outside to inside, so hole will start expanding without increasing the pressure inside the hole. During an experiment, gasket material thickness and hole size in the gasket are chosen according to the specific pressure required to be achieved. For experiments up to $\sim$20 GPa, stainless steel gasket is used, but for higher pressure tungsten (W) or rhenium (Rh) gaskets are used. To achieve higher pressure thinner gasket should be used. A gasket between the diamonds is shown in the figure 1.13. For x-ray experiments if input beam size is larger than hole size, there may be possibility of gasket diffraction peak interfering with the sample peaks or absorption and scattering from the gasket, affecting the diffraction pattern. In such cases, smaller beam size is used. In some cases, beryllium gasket, which is transparent to x-ray, is also used. Amorphous boron, which is of high shear strength or Copper-Beryllium (Cu-Be) gasket is used for the radial x-ray diffraction which is an emerging field of high pressure science. Amorphous boron is too porous to be used as the gasket so it is used with the mixture of epoxy. Recently boron gasket is used for experiments up to 67 GPa [141]. For high pressure
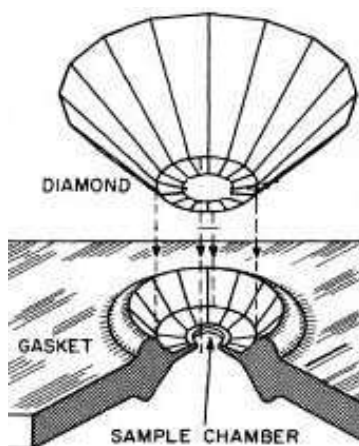
Figure 1.13: A Gasket [20]
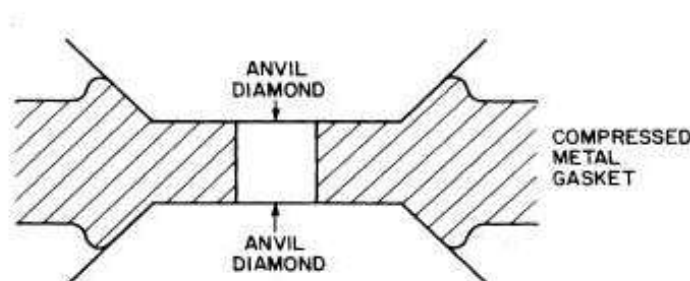
Figure 1.14: Compressed Gasket In Diamond Anvil [20]

synchrotron experiments higher atomic number gasket such as rhenium or tungsten is used as these materials have lower background scattering. For magnetic experiments Cu-Be alloy which is non-magnetic, is used. For transport measurements, gasket made of non conductive materials such as Al_2O_3 or MgO is often used.

1.9.8 Pressure Measurement

Pressure is traditionally measured by the ratio of known force applied per unit area. Measuring scales, based on the fundamental physical laws of conservation of energy, mass and momentum are called primary scales. Shock wave based dynamic pressure, Hugoniot, piston-cylinder device belong to the primary scale [142–144]. For real high pressure experiments, due to friction and material properties, accurate measurement of pressure is not possible.

Also static high pressure experiments are quite different from the dynamic experiments because in shock wave experiments high temperature is also generated along with high pressure so Hugoniot should not be used for static pressure measurements. For low pressure, shock wave equation of state for different materials such as gold or platinum are determined and compared with the static experiments for pressure calibration. These gold and platinum scale are called secondary scale. If primary scales are not possible to be employed for static high pressure experiments then these 'secondary scales' calibrated with the primary scale are employed.

To measure the pressure inside chamber 'pressure markers' are used. Pressure marker may be of any material whose property changes with the pressure and remain non-reactive with the sample. As an example, changes in the resistivity of materials with pressure are used as the indication of pressure. It should be easy to locate inside chamber and pressure determining property should be easily measurable up to the highest pressure range. Most common pressure marker is Ruby, whose fluorescent spectra (shown in figure 1.15) shifts under pressure. For DAC experiments, ruby (Al_2O_3, doped Cr^{+3}) fluorescence line R1 (6942 Å) and R2 (6928 Å) are widely used as the pressure marker [126, 145–147]. In Ruby when Y and U absorption bands are excited, the excited states are transferred in to meta-stable states of ^2T and ^2E. Transition from ^2E to ground state gives R1 and R2 lines. R1 and R2 lines are recently calibrated up to 150 GPa [148]. R1 line is blue shifted for pressure with at a rate of $dp/d\lambda = 2.746$ kbar Å^{-1}. Hydrostatic conditions are determined by the shape, size and distance between R1 and R2 lines. It is the R1 line which shows red-shifting under non-hydrostatic conditions. In contrast to R1 line, R2 line is independent of the non-hydrostatic conditions. For truly hydrostatic conditions R1-R2 line separation remains constant but it changes for non-hydrostatic conditions. The separation of R1-R2 line increases for the ruby, compressed along a-axis while it decreases for the ruby compressed along c-axis. Ruby lines have already been used to achieve accuracy of the order of 1% [149]. Syassen has shown [126] that Cr^{+3} doping, temperature and pressure are independent of each other and frequency

shift can be expressed as following

$$\Delta\nu = \Delta\nu(concentration) + \Delta\nu(Temperature) + \Delta\nu(Pressure)$$

For small value of ΔT and $\Delta\nu$(T) can be written as following

$$\Delta\nu(T) = \left[\left(\frac{\partial\nu}{\partial V}\right)_T \left(\frac{\partial V}{\partial T}\right)_P + \left(\frac{\partial\nu}{\partial T}\right)_V\right]\Delta T$$

Here, $\left(\frac{\partial\nu}{\partial T}\right)_V$ represents the contribution from thermal expansion.

Advantages for the ruby lines is that these lines are very intense, can also be excited by x-ray and ruby is highly non-reactive in most of the experimental conditions. However, ruby marker is not useful for pressure higher than 150 GPa because of shifting of its absorption edge. Also, asymmetry is generated in R line's shape [150] under pressure so exact peak position determination becomes difficult. Besides these, the intensity of Ruby luminescence decreases with pressure. At very high pressures above $\sim$ 150 GPa, diamond and Ruby fluorescence interfere, which need to get separated by appropriate method to measure the correct pressure. This separation of fluorescence of Ruby and diamond has been done by using separate time scale and applied up to $\sim$ 550 GPa by Xu *et. al.* [151]. For high pressure and high temperature experiments, materials such as Sm: YAG crystal (0.5% Sm^{2+}) *etc.* are used for pressure determination [152].

Pressure calibration formula for the ruby is as following [153]:

$$Pressure(P) = \frac{1904}{B}[(1 + \frac{\delta\lambda}{694.24})^B - 1]$$

Where B=7.665 for quasi-hydrostatic conditions and B=5 for non-hydrostatic condition.

For x-ray diffraction experiments, Copper(Cu), Gold(Au) or Platinum (Pt) are widely used as pressure markers.
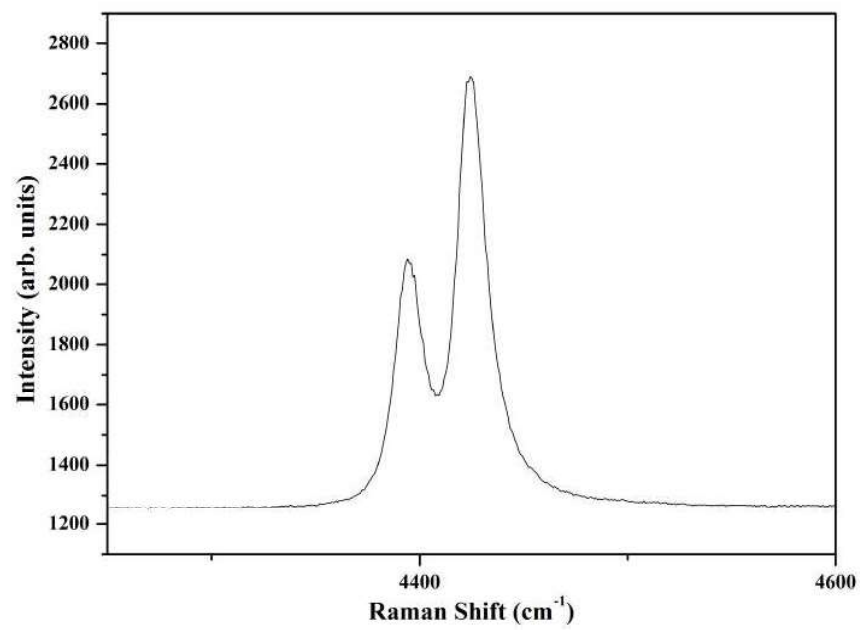
Figure 1.15: Ruby fluorescence at ambient conditions

Pressure (P) is related to volume and compressibility by the relation:

$$P = \int \frac{K_T}{V}(\frac{\partial V}{\partial P})$$

Pressure-Volume curve for the Cu and Au are determined and fitted for known equation of states (EOS) to calculate the pressure:

A third order Birch-Murnaghan equation of state:

$$f_a = (\frac{V_0}{V})^{7/3} - (\frac{V_0}{V})^{5/3}$$

$$f_b = (\frac{V_0}{V})^{2/3} - 1$$

$$Pressure(P) = \frac{3B_0}{2}f_a[1 + \frac{3}{4}(B_0' - 1)(f_b - 1)]$$

There are several equations of state available but most frequently used is the third order Birch-Murnaghan equation of state. Depending upon the requirements of the sample and pressure range, Vinet, universal equation of states *etc.* can be also used [32–34]. Raman mode of diamond at $\sim$1330 cm^{-1} is also sometimes used for calibrating pressure. Recently Yuichi Akahama *et. al.* has used the first order Raman mode of diamond for the pressure calibration up to 310 GPa [154].

1.9.9 Pressure Transmitting Medium

Pressure transmitting medium is used to generate hydrostatic medium inside the gasket chamber where sample is pressurized. Hydrostatic pressure is defined as the stress where off-diagonal elements of the stress tensor are zero. A hydrostatic stress tensor is represented

as following:

$$\begin{pmatrix} \sigma & 0 & 0 \\ 0 & \sigma & 0 \\ 0 & 0 & \sigma \end{pmatrix}$$

Liquids have zero shear strength hence are used for the generation of hydrostatic conditions in the pressure chamber. Any liquid which remains in liquid state at high pressure may be used as the pressure transmitting medium. Liquefied gases such as Helium remain nearly hydrostatic up to ∼50 GPa but due to the difficulty of handling, gases are not frequently used. Mixture of methanol and ethanol in the ratio of 4:1 remains hydrostatic till 10 GPa. Above 10 GPa this mixture solidifies but remains quasi-hydrostatic till ∼16 GPa. Alternatively, a mixture of methanol, ethanol and water in the ratio of 16:3:1 remains hydrostatic till 14.5 GPa. Both mixtures are very convenient to use but displacement of pressure marker or sample from original position, limited pressure range and reaction with sample are some of the disadvantages. Use of soft solid pressure transmitting medium such as CsI *etc.* are also common in high pressure experiments. A list of different pressure transmitting mediums and their usable pressure limit given in the table 1.3.

1.10 High Pressure Techniques Using DAC

There are several high pressure techniques which are feasible with diamond anvil cell [163]. Raman scattering and angle dispersive x-ray diffraction are two widely used techniques [153] to study the materials. In addition to these, energy dispersive x-ray diffraction (EDXRD), low and high temperature measurements [153], inelastic x-ray scattering [164], Brillouin scattering [153,165], neutron diffraction [166], ultrasonic [167], nuclear magnetic resonance [62,153], electron paramagnetic resonance [153], EXAFS [168], Mossbauer spectroscopy [169], magnetic measurements [153] *etc.* are few important techniques used to probe the materials under pressure. In this thesis I have used Raman and angle dispersive x-ray diffraction methods to study materials under pressure.

Medium	Freezing pressure (GPa)	Quasi hydrostatic (GPa)	References
Methonol: Ethanol (4:1)	10.5	~20	[128, 129, 155]
Iso-n-pentane mixtures		~7.4	[128, 129]
Methonol:Ethanol:Water (16:3:1)	14.5	~20	[129]
Silicone Oil	7	~15	[129, 156, 157]
Daphane	2	~5	[158]
Helium	12.1	~50	[129, 159]
Neon	4.7	~15	[129, 159]
Argon	1.9	~30	[130, 159]
Xenon		~55	[160]
Nitrogen (N_2)	2.4	~30	[129, 161]
Hydrogen	5.7	~60	[162]

Table 1.3: Hydrostatic limit of different pressure transmitting mediums

1.11 Raman Scattering

This effect was discovered by an Indian physicist C. V. Raman at Calcutta (Kolkata) in 1928. Meanwhile, two Russian physicists, Landsberg and Mandelstam also observed light scattering with change of frequency while investigating Brillouin scattering from quartz [170]. Theoretical basis had been provided by Smekal [171], though his work was not widely known at that time. Prof. C. V. Raman is considered to be the first who explained the phenomenon of light scattering effect which was named after him and that earned him the Nobel prize in 1930 [172].

Raman scattering is non-destructive, in-situ and fast technique for probing molecular interactions and chemical identification [173]. It is incoherent scattering, resultant scalar sum of scattering by individual atoms. In materials, atoms are connected through bondings. Atoms move relative to each other in materials depending upon the energy state. These molecular vibrations, described as normal modes in the materials, can be classified as optic

or acoustic modes depending upon their phase relation. Energy corresponding to the normal modes is quantized in the form of vibrational phonon. Raman scattering is very weak, approximately one out of 10^6 incident photons is Raman scattered. This is the reason why only after the development of high intensity Laser, Raman scattering has become widely popular.

If there are N number of atoms in the unit cell, total number of independent motions, a molecule can undergo are 3N. There are 3 translation modes, where atoms move in phase to each other, are known as acoustic modes, rest 3N-3 are termed as optic modes. For electromagnetic light ($E=\hbar\omega$), accessible phonons are at the zone center of phonon dispersion curve. There is another method called inelastic neutron scattering which probes all phonon in dispersion curves. Phonons are representative of atomic arrangements, chemical bonding and symmetry of the crystal structure in materials. So if crystal structure changes, phonons dispersion curve of a material also changes. Vibrational mode intensity, frequency *etc.* gives information about the state of a material.

Volume dependence of phonon mode is described by the Gruneisen parameter generated by the phonon dispersion curve. Dimensionless Gruneisen parameter (γ_i) for the vibrational mode ω_i is written as:

$$\gamma_i = -\left(\frac{\partial ln\omega_i}{\partial V}\right)$$

Gruneisen parameter is usually positive because phonon frequency increases with pressure but sometime there may be softening in the phonon frequency. Phonon softening is an indication of structure instability that may lead to a phase transition.

The dependence of thermodynamic variables temperature (T) and pressure (P) also relate with phonon frequency as following:
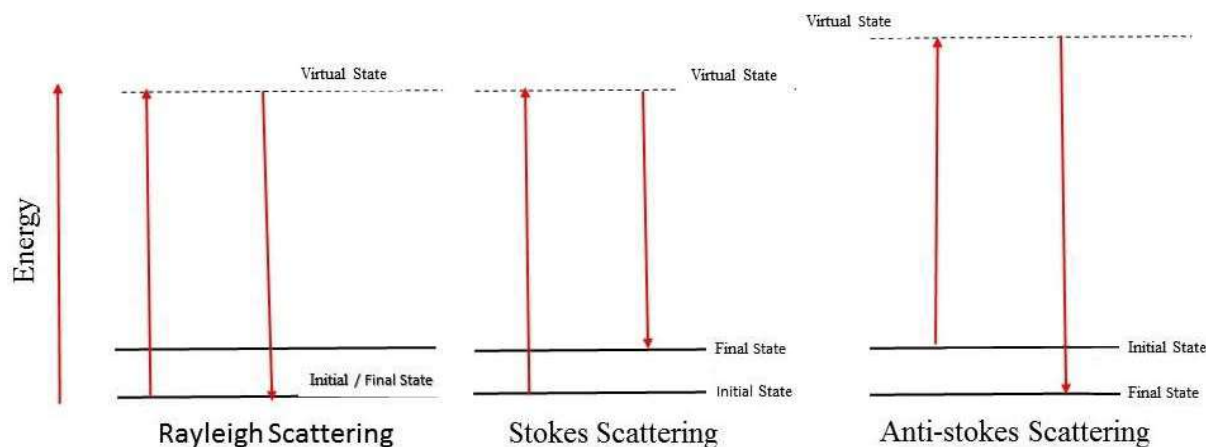
Figure 1.16: Raman Scattering: A energy model diagram

$$\frac{\partial \omega}{dT} = \frac{\partial \omega}{\partial T} - \alpha B \frac{d\omega}{dP}$$

Where B is bulk modulus of material.

1.11.1   Classical Electromagnetic Model

This model is based upon the electromagnetic nature of a photon. When a photon of energy $\hbar$ ω_o is incident on a molecule, photon energy is 'absorbed' and molecule is excited to the higher 'virtual state'. These virtual states are not real state of the molecule so this 'absorption' is not a real absorption of light. After excitation, molecule instantly (10^{-12} sec.) returns to the lower energy state with three possibilities. The process of scattering is shown in the figure 1.16.

1. If it comes back to initial state by emitting a photon of same energy, it is known as Rayleigh scattering.

2. If it returns to a higher vibrational state, which is of higher energy by ω_p from the initial state of molecule, with the energy ω_o- ω_p. It is known as the stokes scattering.

3. If it returns to the lower vibrational state which is of lower energy by the ω_p from the

initial state of molecule, with the emission of photon of energy $\omega_o + \omega_p$, it is known as the anti-stokes scattering.

This energy transfer model is a simplified explanation of Raman scattering. It does not explain the nature of interaction, their probability and intensity of scattered Raman spectra. Classical approach of the Raman scattering is based on the change in polarizability (α) of the molecule under the influence of electric field of incident radiation.

Induced dipole moment (p) of molecule under the influence of electric field (E):

$$p = \alpha E$$

α is two dimensional tensor and signify response of molecule under electric field (E) of incident radiation. Polarizability is the function of nuclear coordinates which in turn function of phonon frequency. A vibrational mode is Raman active only if first derivative of the polarizability is non zero. The condition for Raman active mode for tri-atomic molecule is illustrated in the figure 1.17. As molecules are vibrating about the mean position, polarizability can be expanded using Taylor series as following:

$$\alpha = \alpha_0 + \frac{\partial \alpha}{\partial Q} Q_k + ...$$

For linear approximation, we can neglect second and higher order derivatives of the series. So remaining terms are:

$$\alpha = \alpha_0 + \frac{\partial \alpha}{\partial Q} Q_k$$

If the vibration of molecules is harmonic, normal coordinates of the vibration may be written as a sine function:

$$Q_k = Q_0 \sin(\omega_p t)$$

Polarizability in terms of vibration frequency:

$$\alpha = \alpha_0 + \frac{\partial \alpha}{\partial Q} Q_0 \sin(\omega_p t)$$

Electric field of incident photon with frequency (ω_p):

$$E_k = E_0 \sin(\omega_0 t)$$

Substituting these, in equation

$$p = \alpha E$$

:

$$P = \alpha_0 E_0 \sin(\omega_0 t) + \frac{\partial \alpha}{\partial Q} Q_0 \sin(\omega_p t) E_0 \sin(\omega_0 t)$$

By solving this, we get:

$$P = P(\omega_0) + P(\omega_0 - \omega_p) + P(\omega_0 + \omega_p)$$

On the right hand side, first term represents Rayleigh scattering, second term stokes scattering and third term anti-stokes scattering. Classical theory explains the existence of Rayleigh, stokes and anti stokes lines. Raman emitting molecule will behave as a radiating dipole. A classical electromagnetic description of scattering from a dipole, is given in the appendix A.

At room temperature, number of atoms in a initial/ground state (N_0) are more than excited state ($N_{excited}$). Relation between the number of excited state atoms to ground state is given by Boltzmann's relation:

$$N_{excited} = N_0 \exp\left(\frac{-(\epsilon_i - \epsilon_j)}{KT}\right)$$

Where ϵ_i and ϵ_j are energy state of excited and ground state respectively.

This formula indicates that stokes lines are more intense than anti-stokes line at room temperature. At static high pressure Raman spectra, which is generally isothermal with room temperature, as in the studies presented in my thesis, stokes lines are shown for Raman scattering experiments. Anti-Stokes lines may be used for temperature measurements in high temperature experiments.
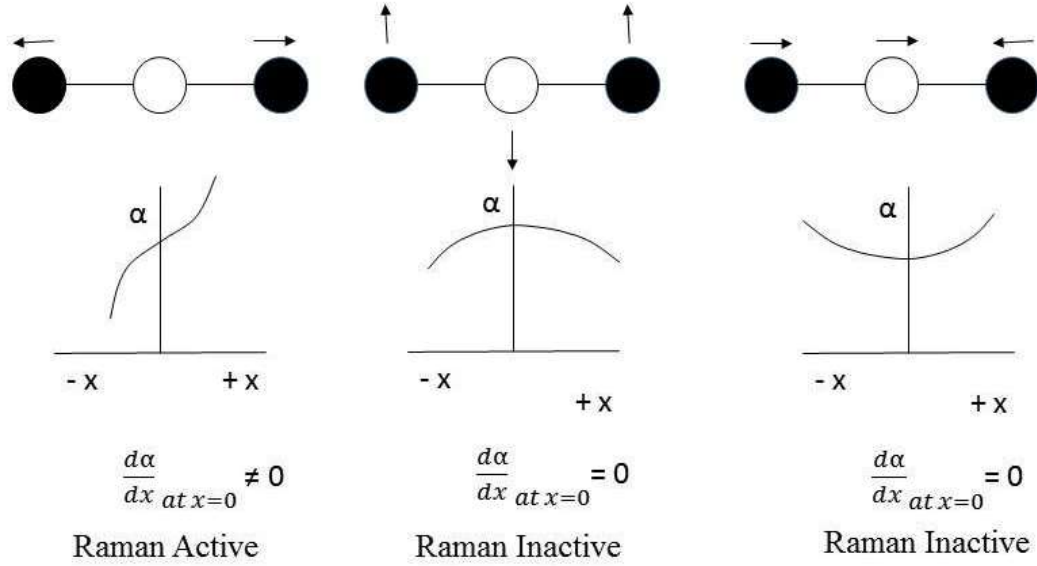
Figure 1.17: Raman Scattering: Active and inactive vibrations on the basis of polarizability change

1.11.2 Quantum Mechanical Theory of Raman Effect

Raman spectra for vibrational states arise due to the transition of molecule from one vibrational state to the other of same electronic state. The matrix element for the transition from one vibrational state to other is written in the terms of polarizability $P = \alpha E$.

$$R^{nm} = \int \psi_n^* P \psi_m d\tau$$

$$R^{nm} = E \int \psi_n^* \alpha \psi_m d\tau$$

As molecule vibrates about the mean position, polarizability can be expanded in terms of Taylor's series.

$$\alpha = \alpha_0 + \left(\frac{\partial \alpha}{\partial x}\right) x + \text{........}$$

where ψ_n and ψ_m are the vibrational eigenfunctions.

$$R^{nm} = \alpha_0 E \int \psi_n^* \psi_m dx + E \left(\frac{\partial \alpha}{\partial x}\right) \int \psi_n^* x \psi_m dx$$

Because of the orthogonality of vibrational states, first term becomes zero except $n=m$. This corresponds to the Rayleigh line (if n=m) in the Raman spectra. If n and m are different states then by putting the following vibrational wave function, integral can be solved.

$$\psi_n(x) = CH_n(x)\exp^{-\beta^2 x^2}$$

Where C, β are constants and $H_n(x)$ is a Hermite polynomial.

The orthogonality of Hermite's polynomial dictates that transition matrix is non zero when n=m±1. If n=m+1, outcome will be Stoke's line and if n=m-1 it will be anti-Stokes lines. Intensity of the Raman signal will depend upon the transition probability that can be calculated from the transition matrix. At room temperature, most of the molecules are in the ground state so the probability of their transition to the higher state will be higher, hence the intensity of Stokes's line will be generally stronger.

1.12   Raman scattering Set Up High Pressure

A high pressure Raman setup includes a spectrograph, sample mounting stage, a Rayleigh filter, diamond anvil cell, optical setup, a excitation source and a detector. The complete description for the Raman system is as following:

1.12.1   Spectrograph: Gratings and Mirrors

A spectrograph contains grating and the mirrors. Mirrors are used for guiding optical path of light and to focus light at right places. A diffraction grating is an optical component with periodic structure, which disperses light. These gratings can be of transmission or reflection type. The diffraction formula for grating is written as following:

$$e\sin\theta = n\lambda$$

Here e is the distance between two periodic structure/rulings and λ is incident light wave-length. n is the order of diffraction spectra. The dispersion power of the grating is obtained by differentiating the diffraction formula.

$$\frac{d\theta}{d\lambda} = \frac{n}{e\cos\theta}$$

So, lower the e, larger will be the dispersion power. For experiments included in this thesis, grating with 1200 lines per millimeter was used.

Scattered Raman light from sample is focused inside spectrograph by a combination of coaxial lens system. Mirrors inside the spectrograph reflects light on the grating. The size of mirror is chosen in such a way that it is able to collect all the scattered light from the sample. This is ensured by a proper combination of *f-number* of internal mirror and optics. Grating disperses the incident light, which is recorded by the detector. One of the popular method of mounting gratings and mirror combination in the spectrograph is known as Czerny-Turner configuration. Czerny-Turner combination is used in the laboratory spectrograph. Schematic of the spectrograph is given in the figure 1.18.

1.12.2   Detector: Charged Coupled Device (CCD)

To detect the scattered light, two types of detectors are used. One is Photo Multiplier Tube (PMT) and other is Charge Coupled Devices (CCD). PMT is highly efficient but collection time is longer, because of this, most of Raman experiments include CCD. CCD is essentially a semiconductor image plate made of tiny pixels. When dispersed light is incident on the CCD, each of these pixel accumulates charge proportional to the incident photons. When Raman signal (dispersed from grating) is incident on CCD, it forms the charge image of the scattered light. Accumulated charge undergoes gain by electronic means to enhance the signal to noise ratio. Accumulated charge is read in series of pixels in a certain specific way. This method to read the accumulated charge, is the reason why detector is named as the charge coupled device. At high temperature dark current in the semiconductor tends
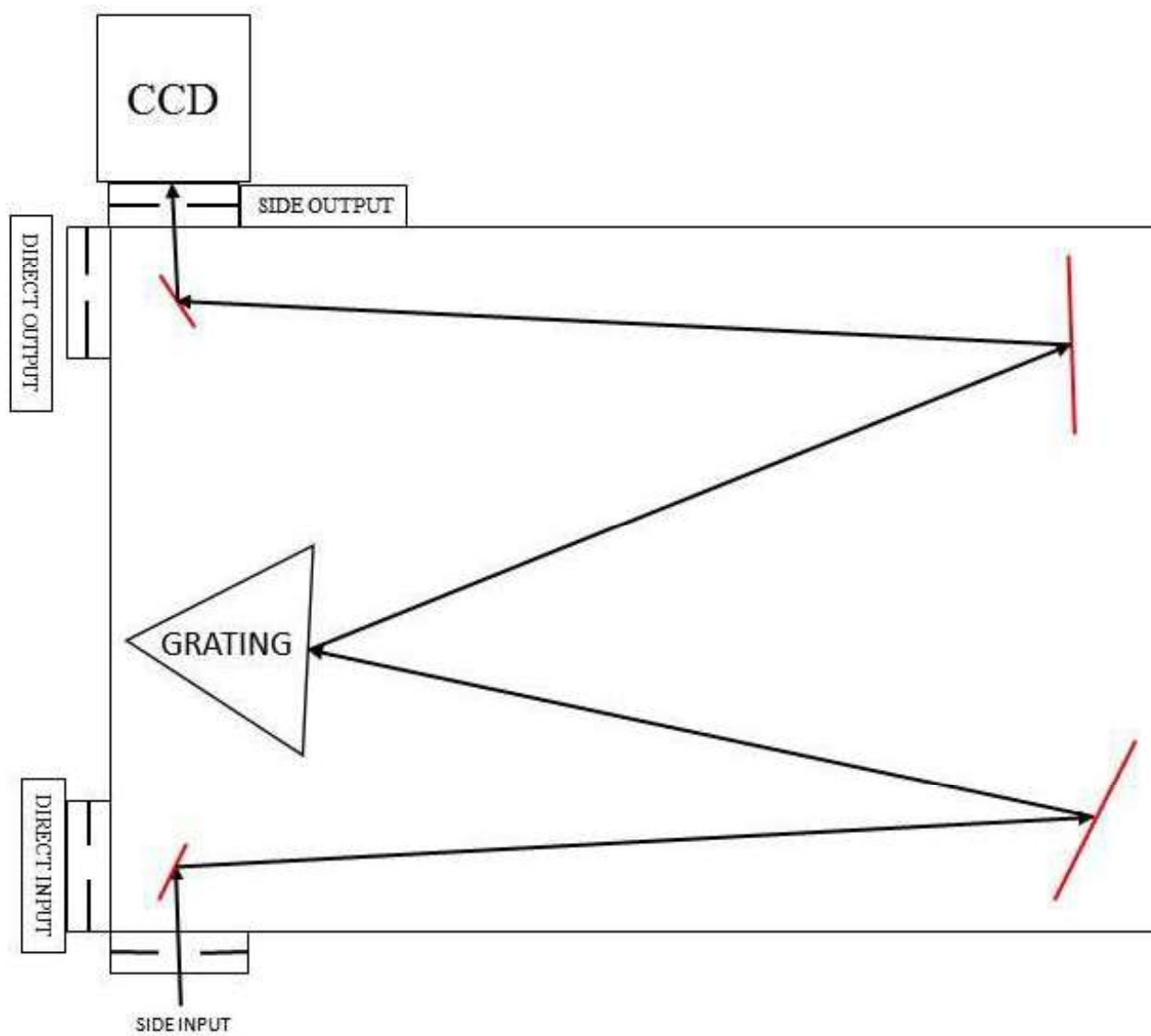
Figure 1.18: Internal arrangement of a Raman spectrograph

to enhance. This dark current reduces the signal to noise ratio. So to enhance the quality of signals, low temperature is desirable for CCD operation. Low temperature is generated either by Peltier or liquid nitrogen cooling. Output of CCD is directly read by the software on computer screen as Raman spectra.

1.12.3   Rayleigh Filter

Raman scattering intensity is 10^6 times weaker than Rayleigh scattering. So, it is necessary to separate the Rayleigh light from the Raman scattering. For this purpose two methods are widely used. First, a holographic filter made of layers of special dielectric materials. As scattered light from the sample is passed through the filter, thickness of layers are set in such a way that it introduces the destructive path difference for the Rayleigh wavelength. Using the recently available filters, it is possible to go up to ~ 10 cm^{-1} near the Rayleigh line. Also, these filters can be made only for a specific wavelength. If we require several wavelengths as an excitation source, to minimize the fluorescence as the case with UV-Resonance Raman, it is necessary to use different filter for each wavelength which is very costly and inconvenient exercise. Two type of filters are available, one is edge filter and the other is notch filter. Edge filter cuts one complete part while notch filter blocks only Rayleigh line, leaving Stokes and anti-Stokes lines. In the setup used for the studies included in this thesis, edge filter is used. Output for edge and notch filter is shown in the figures 1.19 and 1.20 respectively.

Second method to remove Rayleigh line is by introducing two stages of monochromator. These two monochromator, connected in series, are two single spectrograph excluding the detector. Here, output of first monochromator is used as the input for the second monochromator. Both monochromator's gratings rotate opposite to each other, because the dispersion ($\frac{d\theta}{d\lambda}$) for Rayleigh wavelength is zero hence Rayleigh wavelength can be eliminated. Output of the second monochromator is then used as the input for third monochromator with detector which is also in the series with other two spectrographs. But, the use of many stages include many mirrors, grating *etc*. Each of these optical components has efficiency of reflection of light which is not 100%, so the signal strength decreases accordingly with the number of
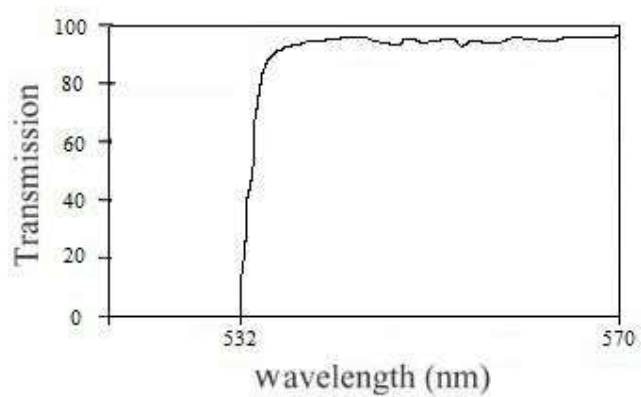
Figure 1.19: Output of a edge filter
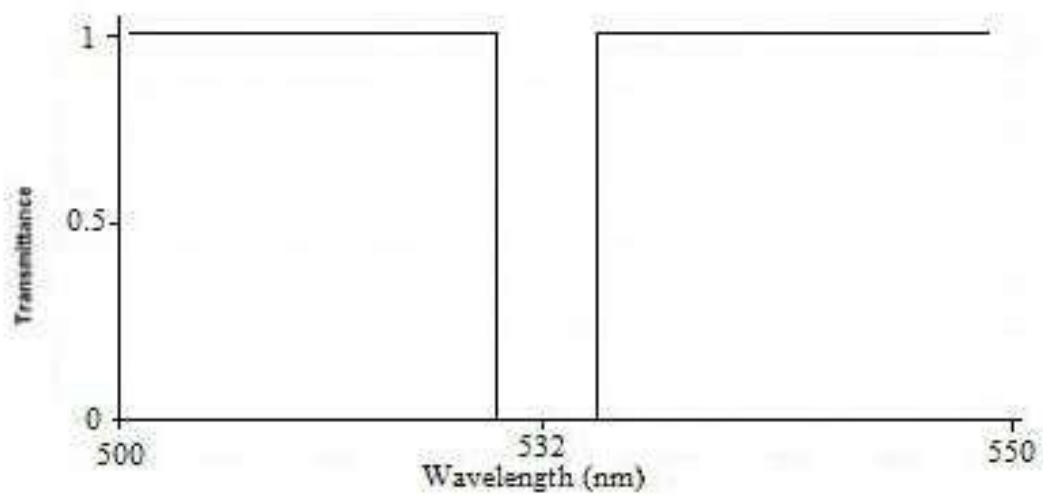
Figure 1.20: Output of a notch filter
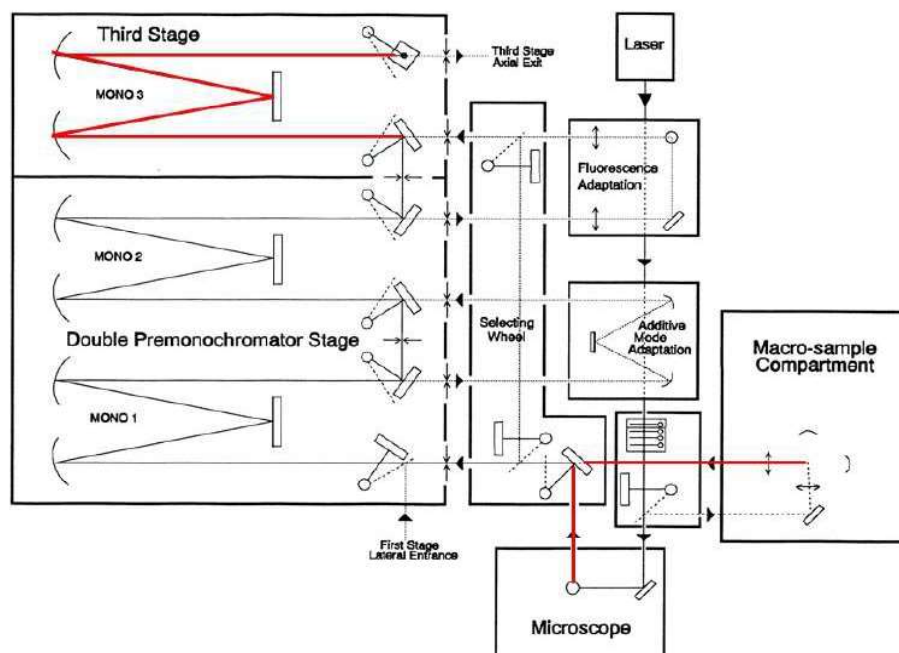
Figure 1.21: Triple stage Raman spectrograph `https://www.isp.kiev.ua/index.php/en/nato-sfp-novel-nanostructures`

optical components in the path. These combined 'triple stage' monochromator are widely used for UV-Resonance Raman experiments where multiple excitation wavelengths are used for excitation. By using triple stage it is possible to go $\sim$5 cm^{-1} closer to the Rayleigh line. Triple stages are also used to enhance the resolution, which typically becomes $\sim$1.0 cm^{-1}. A working diagram for triple stage Raman setup is shown in the figure 1.21.

1.12.4 Excitation Source

High intensity, monochromatic, coherent laser is used as a excitation source for Raman spectroscopy. Generally, solid state lasers, which are compact and easy to handle are used in laboratory. For multiple wavelengths, as required in UV-Resonance Raman, gas laser such as Argon ion or synchrotron sources are used.

1.12.5 External Optical Setup

External optical setup for Raman spectroscopy has sample stage, reflecting mirrors and lenses. The objective lens used for experiment, has 20x magnification and size of laser spot on the sample is less than 3μm. Schematic diagram of Raman setup used, is shown in the figure 1.22. Geometry used for the excitation is back scattering, where incident light and scattered light are at 180° to each other. In addition to it, geometry with incident and scattered light at ±45° may also be employed as per the requirement of experiments. The f-number of optical components are matched with each other and with spectrograph to optimize the collection of scattered light.

1.12.6 High Pressure Raman Setup Used For Experiments

High pressure Raman setup includes the diamond anvil cell which contain the pressurized sample. Excitation laser light is focused by an objective lens on the sample in gasket hole. Sample in DAC is kept at one of the focal point of the coaxial lense system. Scattered light is collected by the same objective and directed toward the spectrograph by a combination of lenses. A holographic edge filter is used to eliminate the Rayleigh wavelength. Rest of the collected light is dispersed by the gratings and recorded by the CCD detector. Collected spectra is shown on the computer screen. Photograph of Raman system used for studies included in this thesis is shown in the figure 1.23. A new confocal Raman scattering for high pressure experiments is installed in the laboratory and details of this system are given in the appendix B.
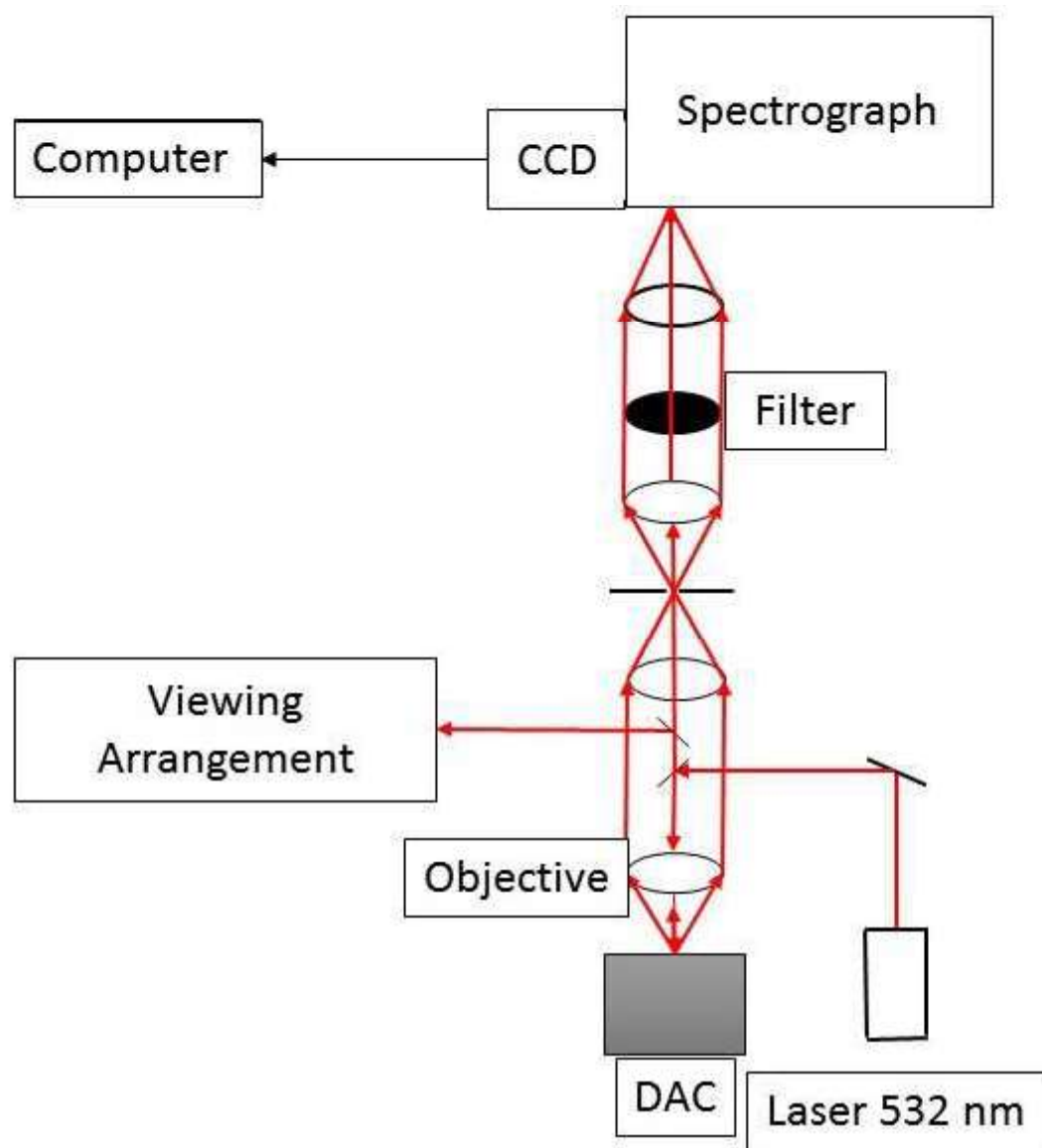
Figure 1.22: Schematics of Raman scattering setup in the laboratory

Figure 1.23: Raman Setup installed in the laboratory

1.13   High Pressure Angle Dispersion X-Ray Diffraction (ADXRD)

1.13.1   Theory of x-ray Diffraction

X-ray interacts electromagnetically with the electronic charge. Atomic form factor or *f(Q)*, is the measure of scattering amplitude of wave by an isolated atom. Mathematically, atomic form factor can be written as the fourier transform of electronic charge density, from real space to the momentum space Q as following:

$$f(Q) = \int \rho(r) \exp^{-iQ.r} dr$$

Where, ρ(r) is electron density of a atom.

So the resultant amplitude of scattered x-ray from the crystal structure is obtained by the summation of an individual atomic form factors. Atomic form factor decreases with increasing the diffraction angle, so the diffraction peaks which are observed at higher angle has low intensity.

Combined structural factor (S_{hkl}) for the structure is written as following:

$$S_{hkl} = \sum_{j=1}^{N} f_j \exp^{-2\pi i(hx_j + ky_j + lz_j)}$$

Where f_j is the form factor corresponds to the jth atom. Here *(hkl)* are Miller indices of a plane and *(xyz)* are the fractional coordinates of an atom.

Scattering intensity *I(Q)*, from structure is related to the structural factor by the following relation:

$$I(Q) = |S_{hkl}|^2$$

XRD scattering intensity also depends upon the temperature of the sample. As temperature increases, intensity (I) of scattered radiation decreases as shown by the Debye waller factor:

$$I = I_0 \exp^{\frac{-(16\pi^2 <u^2> \sin^2 \theta)}{3\lambda^2}}$$

Where, $<u^2>$ is an average of position square, which depends upon the thermal vibration of atom.

If the number of electrons are less in the atom such as hydrogen then determination of location for atom becomes difficult or nearly impossible using x-ray diffraction method. For low atomic number atoms, neutron diffraction is used because neutron interacts with atoms through nuclear absorption cross section. Because of these special properties, neutron diffraction is widely used for the investigation of hydrogen bonded systems. Also, nuclear absorption cross section of atoms does not change with the diffraction angle hence neutron diffraction experiment gives intense peak up to high diffraction angle. Recently, high pressure neutron diffraction experiment, which are generally limited due to less flux and focusing problem, is carried out up to ~50 GPa [174]. Neutrons also carry magnetic moment, so magnetic studies are also possible under pressure if a material has magnetic moment.

1.13.2 Experimental Setup for XRD

Structure plays an important role in influencing the properties of materials. Positions of atoms in the structure decide the band gap, electric properties *etc.* To locate the atoms in a structure, x-ray diffraction and neutron diffraction are employed. X-ray and neutron are
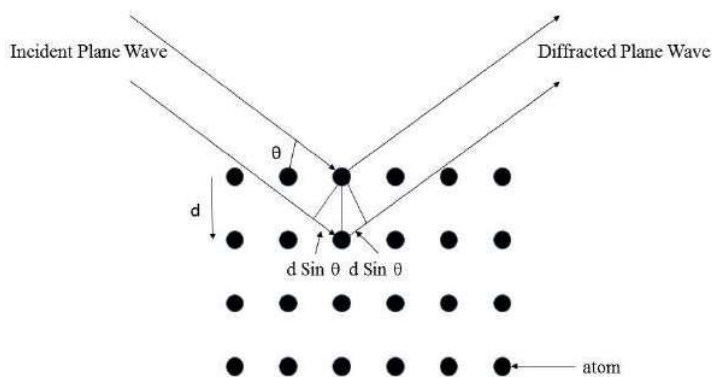
Figure 1.24: Schematics diagram of Bragg's diffraction

diffracted by atoms and diffracted beam interfere constructively or destructively depending upon the arrangement of atoms. Diffracted image is a map of atomic arrangement in the Fourier space. Decoding this, structure of a material is obtained. Diffraction peaks are used to determine the crystal structure system and atomic positions.

For x-ray diffraction, Bragg's condition ($2d_{hkl} \sin \theta_{hkl} = n \lambda$, where is λ is wavelength of incident x-ray radiation and d_{hkl} is spacing of lattice planes in the crystal structure) should be satisfied. Schematic diagram of diffraction from atomic plane is shown in the figure 1.24. There are two methods to satisfy the Bragg's condition. First, we may change the incident wavelength while keeping constant diffraction angle θ_{hkl}, that gives the energy dispersive x-ray diffraction (EDXRD). Second, by keeping wavelength λ fixed but changing angle θ_{hkl}, it is known as angle dispersive x-ray diffraction (ADXRD). There are advantages and disadvantages for both methods. EDXRD is fast and has better signal to noise ratio but the resolution is of the order of $\sim 10^{-2}$, whereas, ADXRD is slow but the resolution is better (of the order of $\sim 10^{-4}$). Generally, in laboratory for high pressure experiments, ADXRD is preferred because it provides better resolution. A ADXRD setup contains the x-ray source, sample mounting stage for DAC and a detector with the computer based reading setup. The schematic of typical high pressure ADXRD diffraction setup is shown in the figure 1.25.

For a polycrystalline sample, all crystal orientations (θ_{hkl}) are possible with equal probability, so x-ray radiation, scattered symmetrically about the primary x-ray beam. If Bragg's
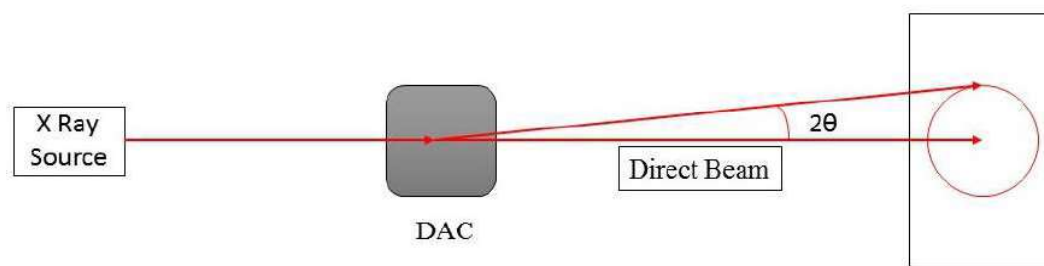
Figure 1.25: Basic schematic of x-ray diffraction
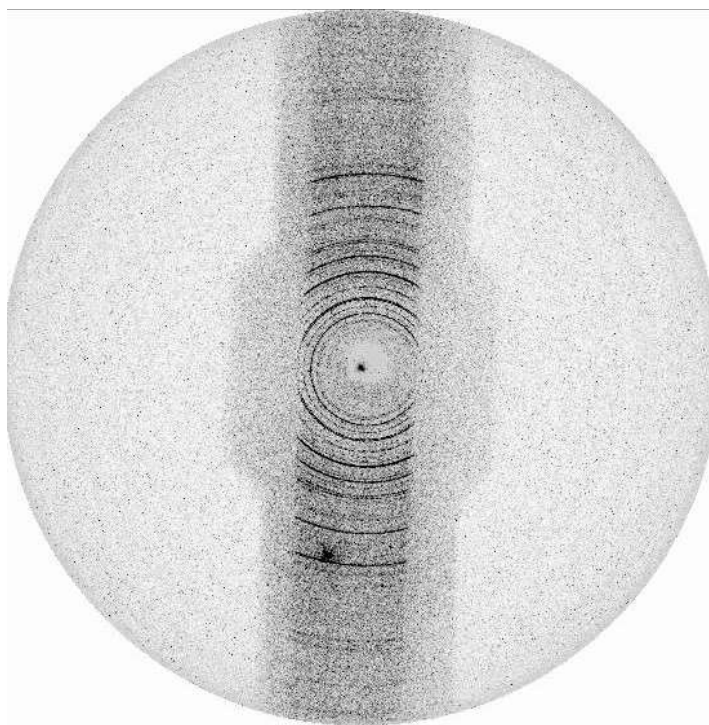
Figure 1.26: XRD image of Iodic acid on the image plate
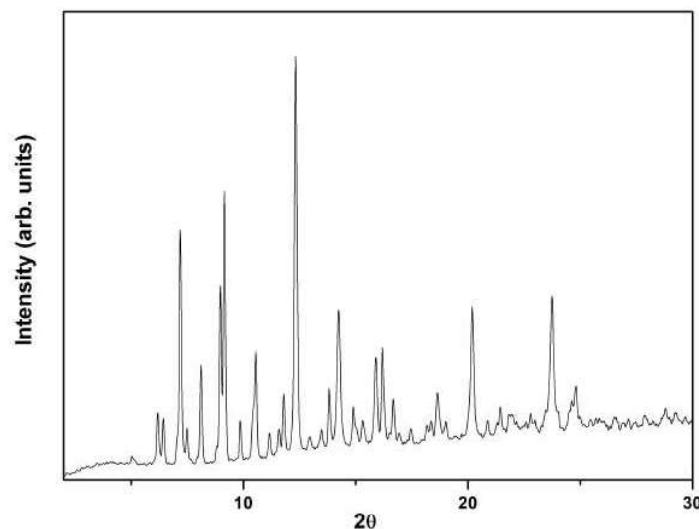
Figure 1.27: One dimensional conversion of XRD image on the detector

condition is fulfilled, diffraction rings are obtained on the flat detector as shown in the figures 1.25 and 1.26. These rings are integrated for the acquisition time period and one dimensional pattern (intensity Vs angle or d-spacing) is obtained as shown in the figure 1.27. There is a drawback of overlapping peaks of different phases in one dimensional pattern as planes have similar d-spacing. To overcome this problem, single crystal x-ray diffraction, which gives the structure and charge density with fair accuracy, is used. However, high pressure single crystal experiments are limited up to the low pressure range due to experimental limitations of loading and sustaining the crystal at high pressure without breaking. Recently, J. Ruiz-Fuertes $et.$ $al.$ has carried out high pressure single crystal studies up to 31 GPa [175].

Size of x-ray beam should be sufficiently smaller than gasket hole size. If it is not the case then diffraction pattern of gasket may interfere with that of the sample. Diamond Anvil Cell (DAC) is placed over the XY stage which can be moved to focus the x-ray beam on to the sample. Diffracted beam which comes out of the backing plate is recorded on the detector. Incident photons charge the semiconductor pixels on detector. Typical diffraction image plate is shown in the figure 1.26. This image is first calibrated for detector distance, wavelength, beam center position, polarization and orientation, with the help of program such as FIT2D [176]. The resultant diffraction pattern in one dimension is shown in the

figure 1.27. Integrated pattern is fitted with the model structure and the difference between the experimental and model is minimized by least square method using available program such as GSAS [177, 178]. Detailed description for crystal structure and x-ray diffraction analysis is given in the appendix C.

For x-ray generation, either laboratory based rotating anode generator or synchrotron source is used. For high pressure experiments, sample size is very small (few micron), so total intensity of scattered light is accordingly low. Synchrotron sources are many order of magnitude (10^{4-10}) more intense and has very less divergence compared to laboratory based source. In addition to this, selection of various wavelength ranging from 10 *pm* to 100 *pm* are also possible in synchrotron sources. However, rotating anode source may only provide few fixed wavelengths such as Cu = 1.5406 Å and Mo = 0.7093 Å *etc.*. Synchrotron radiation enable us to access large *k-space/θ* angle, which is important for diffraction analysis. While scattering power of the crystal vary with the λ^3 but larger wavelengths are easily absorbed by the materials. Due to these advantages, use of synchrotron sources is preferred for high pressure experiments. Along with the source, intensity and wavelength, efficiency of the detector also plays an important role. For higher wavelength, efficiency of the detector increases. Background/Compton scattering intensity increases for shorter wavelengths. For any high pressure x-ray diffraction experiments, source intensity, wavelength, detector efficiency should be considered according to the objectives. For studies included in this thesis, Indus synchrotron source facility at Indore, India and synchrotron source at ELLETRA, Italy are used.

1.14   A Brief Outline of the Subsequent Chapters

In this thesis, I have presented high pressure behaviour of some hydrogen bonded molecular solids. Chapter 2 includes high pressure study of deuterated α-glycine [9], the simplest amino acid. This chapter explains competing interactions of hydrogen bonds that result in conformational changes of molecular units in the crystal structure. Chapter 3 contains the

polymerization study of acrylamide under pressure [10]. This chapter discusses the mechanism of high pressure polymerization and role played by hydrogen bond during polymerization. Chapter 4 includes high pressure investigation of imidazole which is an important part of the biological enzyme systems. Ionic form and proton transfer mechanism in this compound under the influence of pressure is discussed and correlated with the experimental and theoretical observations [14]. Chapter 5 discusses the high pressure Raman and x-ray diffraction investigations of iodic acid which is the simplest and important oxoiodate and has strong second harmonic generation property. Iodic acid may be used as a model system to study and design more novel and useful oxoiodates.

Chapter 2

Hydrogen bond Vs Conformational Changes: Deuterated α-Glycine

2.1   Introduction

Amino acids are the basic building blocks of protein. The structure of protein is characterized by linear chains of amino acids which fold in different ways for the growth, repair and working of the body cells. Amino acids are classified in to two categories, essential amino acids, (ex. histidine, isoleucine, leucine) that can not be made by the human body itself so necessarily need to be taken through food and non-essential amino acids which are prepared by body itself. Glycine is a non-essential amino acid. Amino acids include functional groups amine ($-NH/D_2$) and carboxyl ($-COOH/D$), along with a side chain (R) which is specific to each amino acid as shown in figure 2.1. Amino acids are rich in varieties of hydrogen bonds (N-H- - -O, O-H- - -O, C-H- - -O, *etc.*). Hydrogen bonding interactions control secondary structures of protein and play an important role in stabilizing their structure in different conformations. These conformations impart amino acid with various unique properties and enable them function in biological and materials science applications such as food industries, drug and cosmetics.
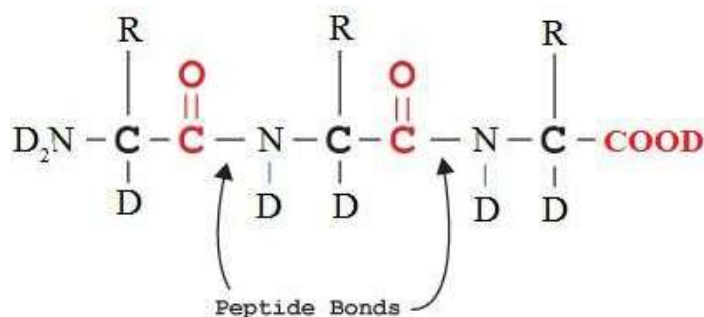
Figure 2.1: Chemical structure for amino acid
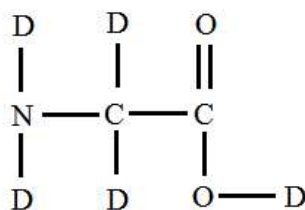
Figure 2.2: Chemical formula for α-deuterated Glycine

2.2   Motivation

High pressure is an important tool to study polymorphism in materials. As hydrogen bonds can be easily distorted in comparison to other stronger inter and intra molecular interactions, intermediate structures obtained at higher pressures can accommodate a variety of subtle structural rearrangements without drastic changes in the crystal symmetry. While the relevance of pressure range for various biological processes would be limited to less than 1 GPa, investigations of these amino acids under much higher pressures would be of significance for geophysical and material research applications. The knowledge of high pressure behaviour of hydrogen bonds in isolated amino acids forms a basic platform for understanding these interactions when these molecules are in different chemical environments, such as organic and inorganic complexes, dipeptides and proteins. For example in the case of Bis(glycinium) oxalate, an organic complex of glycine, high pressure investigations reveal drastic changes

in the hydrogen bonding network across 1.7 GPa. Across this pressure, when the glycine molecules (deuterated molecule shown in figure 2.2) reorient themselves across the structural transition, N-H- - -O hydrogen bonds were found to break and weaker hydrogen bonds are formed [179]. The high pressure behaviour of the N-H- - -O hydrogen bonds in this compound is found to be very similar to that of γ-glycine [180–185].

Amino acids have been investigated rather extensively in the recent years [180–214]. Table 2.1 gives an overview of high pressure investigations of various amino acids. Among the several amino acids which are studied under pressure, glycine is found to show significant changes in the hydrogen bonding interactions. Glycine, the simplest amino acid, has been studied under pressure in detail by several techniques such as x-ray diffraction, Raman spectroscopy, inelastic neutron scattering, *etc.* [180–189]. Glycine can exist as α, β and γ polymorphs and the corresponding crystal structures have different kinds of hydrogen bonding networks. All these polymorphs exist in zwitterionic form under ambient conditions as shown in figure 2.3 for α-deuterated glycine. High pressure x-ray diffraction studies report that α-glycine is more compressible within layers than normal to the layers and this behavior is attributed to the repulsive nature of interactions between CH_2 groups between the layers [182, 185]. The spectral changes of NH_3^+ and COO^- functional groups observed in the earlier Raman investigation had indicated a subtle transition across 3 GPa, which is possibly related to the changes in the intra-layer hydrogen bonding interactions [186]. β-glycine shows a reversible structural transition at pressures as low as $\sim$0.8 GPa and across the transition, some of the hydrogen bonds were found to change non monotonically which manifest as major changes in the spectra related to NH_3^+ and COO^- groups [185, 187, 188]. γ-glycine undergoes an irreversible structural phase transition across $\sim$3 GPa transforming the helical network of hydrogen bond to a layered hydrogen bonding network at higher pressures [180–185]. Once transformed from the helical network to a layered structure, helical structure is not restored on release of pressure, thus resembling the behaviour of biopolymers.

So far the high pressure investigations of undeuterated α-glycine have been done using x-ray diffraction (highest pressure studied so far is 6 GPa) [182, 185]. Raman spectroscopy
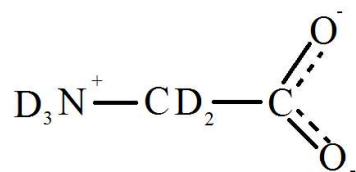
Figure 2.3: Zwitterionic form of α deuterated Glycine

(the highest pressure studied so far is 23 GPa), [186] inelastic neutron scattering (the highest pressure studied is 1 GPa) [189]. Recently, a high pressure neutron diffraction investigation on ϵ-glycine (a high pressure daughter product of γ-glycine) has been done up to 5.3 GPa [215]. However, high pressure neutron diffraction study of α-glycine, which can provide hydrogen bond parameters at high pressures is not available in the literature.

In the absence of neutron diffraction data, Raman spectroscopic investigations can be used as a complementary method, as it provides some insights into the nature of changes in hydrogen bonds in this compound under pressure. In the case of undeuterated α-glycine, some of the vibrational modes which can be used as a tool for understanding the nature of hydrogen bonds are not well resolved. In particular, the assignment of NH_3^+ torsional mode has been controversial as it is merged with the COO^- rocking mode. Also, only one N^+-H stretching band corresponding to the weak inter-layer hydrogen bond was observed. In contrast, the Raman spectra of deuterated α-glycine, other N-D stretching bands are also well resolved therefore high pressure study of deuterated α-glycine can provide additional information on the pressure induced changes in the hydrogen bonding interactions. Also shift in the vibrational frequency of NH_3^+ torsional mode on deuteration and its high pressure behaviour can be used to verify its assignment.

We have carried out high pressure Raman investigations of fully deuterated α-glycine up to 20 GPa. Using the high pressure behaviour of N-D stretching, C-D stretching and ND_3^+ torsional modes we report here the possible pressure induced changes in the intra-layer and inter-layer hydrogen bonds in α-glycine. We have also presented a brief comparison of the high pressure behaviour of hydrogen bonds in various amino acids and amides.

2.3   Experimental Details

Polycrystalline sample of fully deuterated α-glycine, procured from Newmax Chemicals with purity $\sim$99 % was characterized by Raman spectroscopic investigations and is found to be consistent with the Raman spectra reported for fully deuterated α-glycine [216, 217]. Polycrystalline sample was loaded into a hole of 200 μm in a pre-indented steel gasket of thickness 50 μm placed in a Mao-Bell type of Diamond Anvil Cell. No pressure transmitting medium was used so as to avoid any interaction with the sample. However, spectral changes in this soft solid at low pressures $\sim$3 GPa are found to be similar under hydrostatic as well as non hydrostatic conditions [186]. The effect of non-hydrostatic stresses at much higher pressures is mentioned while discussing the results. Pressure was calibrated using the ruby R-lines. Nd-YAG laser of 532nm was used as our excitation source. Raman scattered light was collected in the back scattering geometry and recorded using a CCD based HR460 Jobin Yvon spectrograph. Edge filter was used to get rid of the Rayleigh scattered light. Neon lines were used for calibration of Raman lines. Raman spectra of fully deuterated α-glycine under non hydrostatic pressure were recorded up to $\sim$20 GPa.

2.4   Result and Discussion

Raman spectra of fully deuterated α-glycine were recorded in the entire spectral region of interest excluding the spectral region of diamond peaks. These assignments were also cross checked with reported experimental values of undeuterated α-glycine, partially deuterated α-glycine, and fully deuterated α-glycine [185, 216, 217, 220]. Most of our assignments are based on the experimental values reported by Machida *et. al*, which were found to be consistence with their lattice dynamical calculation [220]. Table 2.2 gives the comparison of Raman mode frequencies observed in this study and the reported values of Machida *et. al.* [220] The

Compound	Techniques	Transation Pressure (GPa)	Structural or conformational change	Change in hydrogen bond
α-glycine	Raman [186], single-crystal X-ray(6.2 GPa) [182, 185], inelstic neutron scattering [189]	3	Subtle structural rearrangement(reversible)	No significant increase in interlayer N-H- - -O hydrogen bond; possible increase in C-H- - -O bond
β-glycine	Raman [187], X-ray [185, 188], inelastic neutron scattering [189]	0.8	Transform to $P2_1/c$(reversible)	Across the transtion, hydrogen bond is bifurcated
γ-glycine	Raman, [180, 181] X-ray, [182, 185] inelastic neutron scattering [189]	3	Transforms to Pn(irreversible)	From helical to layered network
L-alanine	Raman, [190, 191, 193] X-ray, [192, 193] neutron diffraction [194]	2	subtle change(reversible)	-
Mono-hydrated L-asparagine	Raman [201]	0.1, 0.2, 0.9	-	-
L-leucine	Raman [202]	0.5, 0.8, 3.6	-	-
Isoleucine	Raman [203]	2.3, 5	-	-
Methionine	Raman [204]	2.2	-	-
L-taurine	Raman [205, 206]	0.7, 5.2	-	-
D-threonine	Raman [218]	1.9-2.4 GPa and 5.1-6.0 GPa	3.5 GPa, 4.3 GPa	-
L-threonine	Raman [207, 219]	2, 8.2-9.2, 14-15.5	4.8, 6.0 (conformational changes)	-
L-Valine	Raman [208]	3	-	-
DL-Valine	Raman [197]	3	-	-
L-Cysteine	Raman, [211, 212] X-ray [196]	1.1,3(Raman) and 1.8 (X-ray)	Structural	Change in orientation and type of hydrogen bonding of sulfhydryl groups(Raman) No change in the orientation of the molecules (x-ray)
DL-Cysteine	Raman [211, 212]	0.1, 1.5, 2	Structural	-
DL-serine	Raman [197, 198], single crystal X-ray [198]	1.5, 8.6	Subtle change(reversible)	-
L-serine	Raman, [213] X-ray, [199, 214] Neutron diffraction [200]	5.4, 8.0	Structural	O-D- - -O-D chains are replaced by shorter O-D- - -O hydrogen bonds to caboxylate groups

Table 2.1: Comparison of high-pressure behaviour of various amino acids

Mode	(at 0.5 GPa)	(at 8.8 GPa)	(dν/dp at 0.5 GPa)	(dν/dp at 3 GPa)	Machida *et. al.* [220]
Lattice modes	-	144	-	-	72
-	-	160	-	-	84
-	-	179	-	-	107
-	147	212	4.5	-	144
-	-	242	-	-	151
COO$^-$ (torsion)	185	-	17.2	7.0	185
CCN δ (deformation)	330	-	7.1	3.4	328
ND$_3$ $^+$ τ (torsion)	360	-	2.0	6.1	344(calculated)
COO$^-$ ρ (rock)	459	-	4.6	2.9	456
COOω (wag)	530	-	1.4	-	527
COOδ (bend)	646	-	-0.2	1.8 (at 5 GPa)	643
CD$_2$ ρ (rock)	720	-	2.3	-	718
ND$_3$ $^+$ ρ (rock)	812	-	-4.9	0.3	807
ND$_3$ $^+$ ρ (rock)	872	-	2.0	2.0	807
-	919	-	-	-	-
C-C ν (stretch)	934	-	1.6	1.6	930
-	939	-	-	-	-
C-N ν (stretch)	954	-	3.1	3.1	950
-	964	-	-	-	-
CD$_2$ Γ (twist)	1021	-	1.5	1.5	1015
CD$_2$ δ (bend)	1080	-	1.8	1.8	1078
-	1087	-	-	-	1078
CD$_2$ ω (wag)	1135	-	0.2	1.00 (at 7 GPa)	1130
ND$_3$ $^+$ δ(A)assym. deformation	1178	-	1.8	-	1172
ND$_3$ $^+$ δ(S)assym. deformation	1198	-	-	-	1193
ND$_3$ $^+$ δ(A)assym. deformation	1213	-	-	-	1207
ND$_3$ $^+$ δ(A)assym. deformation	1178	-	1.8	-	1172
COO$^-$ ν (S) sym. stretch	1391	1409	4.5	2.1 (at 7 GPa)	1389
-	1407	-	5.5	3.7	1406
COO$^-$ ν (A) asym. stretch	1561	-	-	-	1545
-	2135	-	-	-	-
ND ν (S) sym. stretch	2164	-	4.5	3.0	-
CD$_2$ ν (S)(sym. stretch)	2185	-	5.4	3.7	-
CD$_2$ ν (A)(asym. stretch)	2265	-	6.1	5.2	-
ND ν (S) sym. stretch	2333	-	4.5	2.2	-

Table 2.2: Raman mode assignments of fully deuterated α-glycine

Raman spectra of fully deuterated α-glycine in the spectral region 50-1250 cm^{-1} at different pressures is given in figure 2.4. and the pressure induced changes of the Raman shifts in this spectral region are given in figure 2.5. Figures 2.6 (a) and (b) give the Raman spectra in the spectral region 1400-1700 cm^{-1} and 2100-2450 cm^{-1} respectively. The pressure induced changes in the Raman shifts of these modes are given figure 2.7. The rate of change of frequencies of various Raman modes at $\sim$0.5 GPa as well as at 3 GPa is given in table 2.2.

As seen from figure 2.4 and 2.5, the intensity of the CCN deformation mode (330 cm^{-1}) decreases and its frequency stiffens under pressure. The frequency of the ND$_3^+$ torsional mode (360 cm^{-1}) remains nearly constant and its intensity reduces up to 3 GPa which is similar to the behaviour of this mode for undeuterated α-glycine under pressure [186]. Also, this indicates that our assignment of this mode for ND$_3$ $^+$ torsional mode is indeed appropriate and its high pressure behaviour is discussed separately in the subsequent section. COO$^-$ bending mode softens up to 3 GPa and starts stiffening above 5 GPa. This behaviour is similar to that of undeuterated α-glycine. However the behaviour of COO$^-$ wag and COO$^-$ rock are found to be different from that of undeuterated α-glycine. In the case of undeuterated α-glycine COO$^-$ wag was found split, whereas in the deuterated analog COO$^-$ rock is found to split. CD$_2$ rock (720 cm^{-1}), ND$_3$ $^+$ rock (877 cm^{-1}), C-C stretch (937cm^{-1}), C-N stretch (949 cm^{-1}), CD$_2$ twist (1019 cm^{-1}), CD$_2$ bend (1082 cm^{-1}), ND$_3$ $^+$ asymmetrical deformation (1092 cm^{-1}), ND$_3$ $^+$ deformation (1133 cm^{-1}) shows stiffening with increasing pressure. As seen from these figures, COO$^-$ symmetric stretching mode is observed as doublet at 1391 cm^{-1} and 1407 cm^{-1} and these spectral features have been reported earlier for fully deuterated α-glycine [220]. These modes show pressure induced stiffening with a small slope change across 3 GPa. The relative intensity of the latter mode increases with pressure and at higher pressure they merge and appear as a single band.

As seen from figure 2.6, in the deuterated α-glycine, consists of three distinct bands (2135 cm^{-1}, 2185 cm^{-1}, 2265 cm^{-1}) corresponding to C-D bands. Apart from the symmetric and antisymmetric CD$_2$ stretching bands, additional band in the CD$_2$ stretch region (2135 cm^{-1}) is similar to the spectra of C-deuterated glycine and fully deuterated γ-glycine [181, 217].
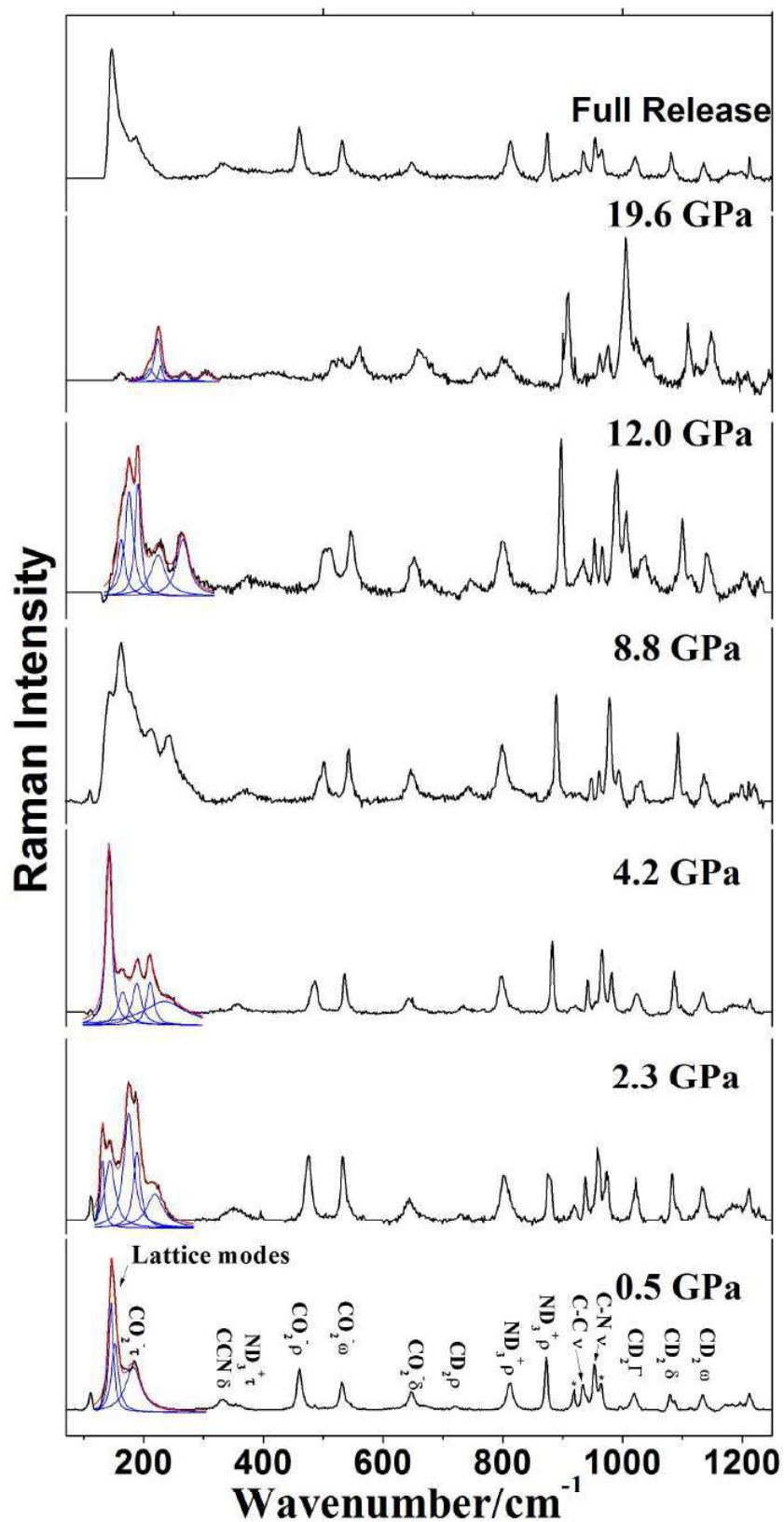
Figure 2.4: Raman spectra of fully deuterated α-glycine in the spectral region 50-1250 cm^{-1} at different pressures; various symbols given are as described in table 2.2.
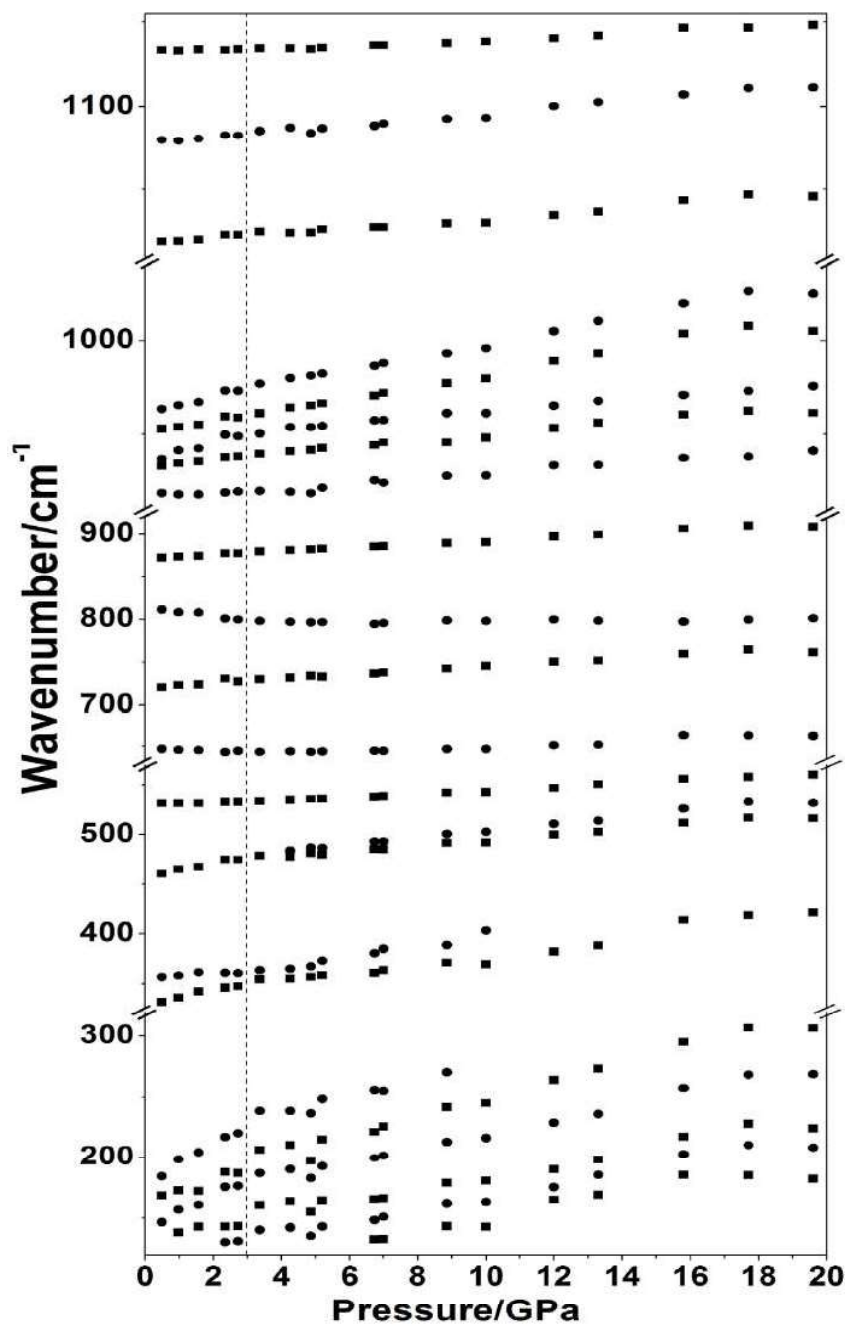
Figure 2.5: Pressure induced variation of Raman shifts in the spectral region 50-1250 cm^{-1}; various symbols given are as described in table 2.2.
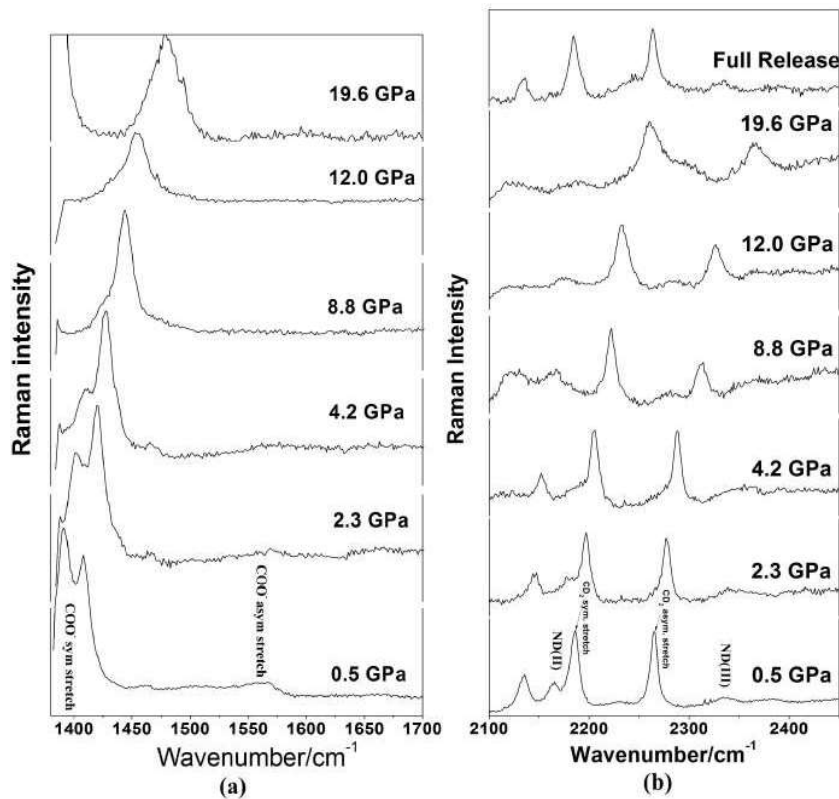
Figure 2.6: (a) Raman spectra of fully deuterated α-glycine in the spectral region 1400-1700 cm^{-1}; (b) Raman spectra of fully deuterated α-glycine in the spectral region 2100-2450 cm^{-1} at different pressures; ND(II) and ND(III) represent N-D stretching modes; CD (Sym) and CD (Asy) represent CD_2 symmetric and anti-symmetric stretching modes respectively.

CD_2 symmetric stretch (2185 cm^{-1}) and CD_2 asymmetric stretch (2265 cm^{-1}) monotonically stiffens with pressure.

Other bands expected in this region are the ND(I) and ND(II) stretching modes corresponding to the intra-layer hydrogen bonding interactions and ND(III) band corresponding to the inter-layer hydrogen bonding interactions. For undeuterated α-glycine these modes (NH(I); N-H3- - -O2 =2.77 Å; H3- - -O1=1.73 Å) and (NH(II); N-H4- - -O1 = 2.850 Å; H4- - -O1 = 1.83 Å), NH(III) = (N-H(3)- - -O2=3.08 Å; H(3)- - -O(2)=2.12 Å.) are expected at 2630, 2895 and 3145 cm^{-1} respectively.

Hydrogen bond parameters referred above are for undeuterated α-glycine [221] as so far these parameters have not been reported for deuterated α-glycine. The corresponding modes

ND(I), ND(II) and ND(III) for deuterated glycine (NH/ND = 1.34) are therefore expected at 1962 , 2160 cm^{-1} and 2335 cm^{-1} respectively.

At ambient pressure, a very weak mode was observed at 2000 cm^{-1}, which is possibly the ND(I) band corresponding to N-D3- - -O1, As it becomes too weak to be followed under pressure we have not discussed this mode under pressure. The mode observed at 2164 cm^{-1} is possibly ND(II) band corresponding to the hydrogen bond N-D4- - -O1. This band stiffens up to 4 GPa and is buried under the strong C-D stretching band at higher pressures. Weak band observed at 2335 cm^{-1} can be identified as ND(III), band corresponding to the bifurcated inter-layer hydrogen bonds forming antiparallel double layers. This mode shows pressure induced stiffening up to 20 GPa.
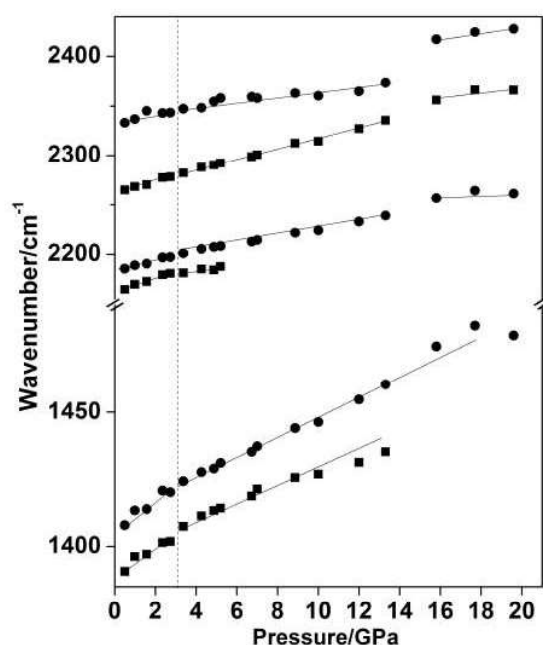
Figure 2.7: Variation of Raman shifts with pressure in spectral region 1400-2450 cm^{-1}.

Most of the observed Raman modes were found to become broader and weaker at high pressures up to 20 GPa. As no pressure transmitting liquid is used in these experiments, the broadening of the Raman modes and slope changes at higher pressures may also arise

from non-hydrostatic stresses. However, non-hydrostatic effects do not seem to result in any change in the crystal symmetry. All the observed pressure induced changes were found to be completely reversible on release of pressure. The effect of deuteration is not found to affect much the overall spectral changes under pressure. Also, at ambient pressure, deuterated glycine is found to contain two CO stretching modes and this observation is similar to that L-alanine [193]. It may be noted that in the undeuterated glycine only one CO symmetric stretching mode is observed. In the case of alanine, these spectral features have been attributed to zwitterionic nature of this compound being incomplete under ambient conditions. However, at higher pressures these modes merge into one mode, which indicate that glycine exists in zwitterionic form at even higher pressures. Also there was no C=O stretching band observed at higher pressures which is spectroscopic finger print for neutral form of glycine.

2.5 ND_3^+ Torsional Mode in α-glycine at Higher Pressures

The assignment of NH_3^+ torsional mode of α-glycine has been a controversial issue and several spectroscopic investigations at ambient conditions could not clearly identify this mode as it overlaps the COO^- rocking mode and both the modes are seen as a single broad band. However, using the high pressure behaviour of these modes, NH_3^+ torsional mode was identified in our earlier study of undeuterated α-glycine [186]. The mode at 359 cm^{-1}, whose high pressure behaviour is similar to that of undeuterated α-glycine, is assigned as ND_3^+ torsional mode and the ratio of NH_3^+/ND_3^+ modes is 1.37 which is very close to the ratio of square root of moment of inertia of these modes. As seen from figure 2.4 and figure 2.6, the intensity of the ND_3^+ torsional mode as well as CO_2^- torsional mode decreases considerably in the pressure range 0-3 GPa. The structural implications of variation of the intensity of NH_3^+ torsional mode, which may hold the key for understanding of high pressure behaviour of various hydrogen bonds in this compound, is discussed in the subsequent section. As the high pressure behaviour is similar for both deuterated and undeuterated α-glycine, these

discussions will be applicable to both the compounds.

2.6   Hydrogen Bonds in α-Glycine at Higher Pressures

Among the ND(I) and ND(II) bands which correspond to the intra-layer hydrogen bonds, ND(I) is too weak even under ambient conditions and hence we would be discussing only the high pressure behaviour of ND(II) stretching mode as shown in figure 2.6 (b). This mode shows pressure induced stiffening up to 4 GPa and above this pressure it is buried under the stronger C-D stretching band and hence unambiguous report of high pressure behaviour of this mode above this pressure is very difficult. However, up to 4 GPa the stiffening of this mode indicates medium strength hydrogen bond ND(II) does not show any signature of reduction in its length, if we use the spectroscopic signature of proper hydrogen bonds [22]. ND(III) band which corresponds to the inter-layer hydrogen bond is observed at 2335 cm^{-1} and this mode displays pressure induced stiffening at rate of 4.5 cm^{-1}/GPa at ambient conditions. The stiffening rate of this mode reduces to (half of its value at ambient conditions) 2.2 cm^{-1}/GPa at 3 GPa. It may noted that our Raman spectroscopic study of the undeuterated α-glycine [186] had shown pressure induced stiffening of the N$^+$-H stretching mode (3145 cm^{-1}) corresponding to the interlayer hydrogen bonds (N-H3- - -O= 3.08 Å; H3- - -O= 2.12 Å). The stiffening of the N$^+$-H stretching mode generally indicates increase of the corresponding hydrogen bond length and this correlation has been applicable in many systems [22]. However, in the case of bifurcated hydrogen bonds, one has to look in to the influence of the change in the hydrogen bond length as well as angle on the stretching mode of the corresponding covalent bond.

Dawson *et. al.* have reported single crystal x-ray diffraction study of undeuterated α-glycine at 2 GPa and 6.2 GPa [185]. Based on this study, they report the interlayer hydrogen bond N$^+$H(III) to be 2.183(15) Å at ambient conditions and 2.18 Å at 6.2 GPa and the variation is too small compared to the error bar. Powder x-ray diffraction study reported by Boldyreva *et. al.* up to 4 GPa indicate that maximum strain was in the direction of weak
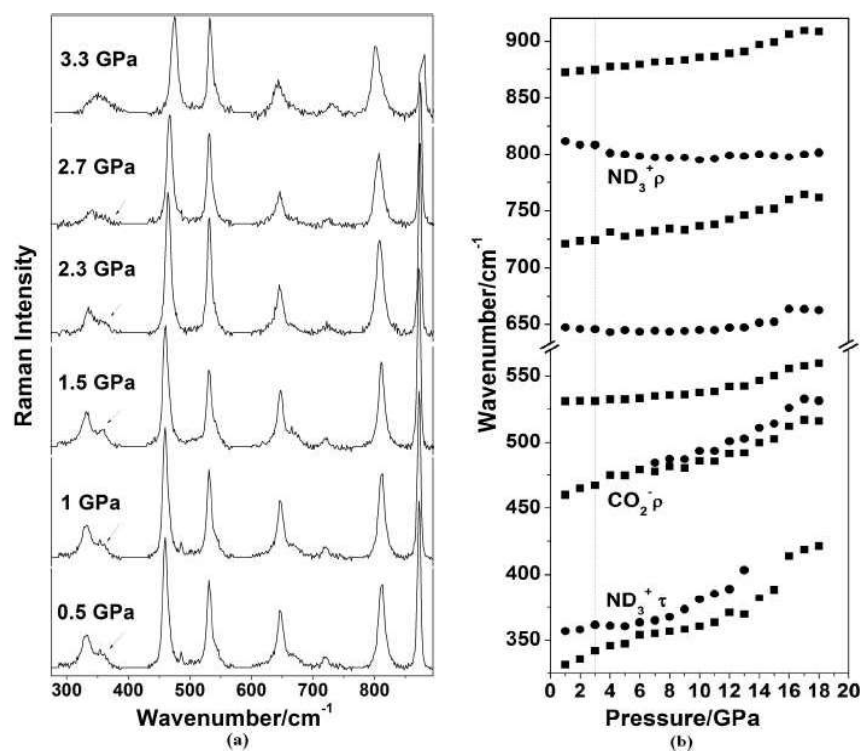
Figure 2.8: (a) Raman spectra in spectral region 200-850 cm^{-1} in the pressure range 0-3 GPa, the arrow indicates the ND$_3^+$ torsional mode; (b) Variation of Raman shifts with pressure in the spectral region 200-850 cm^{-1}.

hydrogen bond and minimum lattice strain were in the directions of strong hydrogen bonds in the structures. The hydrogen bond parameters reported in the x-ray diffraction studies can not be unambiguously used for spectroscopic correlation, as both the x-ray diffractions investigations did not refined the hydrogen atom positions. Alternatively we have tried to correlate other spectroscopic features which are related to the hydrogen bonds reported for other amino acids.

The variation in the intensity of NH$_3$ $^+$ torsional mode has been reported [222, 223] for some of the amino acids such as for α-glycine, L-alanine at different temperatures. When the temperature is lowered, these modes become sharp, split and well pronounced. There is considerable reduction and broadening of this mode when the temperature is increased. In the case of L-alanine, NH$_3$ $^+$ torsional vibration has been related to the restricted vibration of a symmetric top [222]. The distance between the top and neighbouring atoms in the

crystalline environment are changed considerably during torsional motion and the increase in the intermolecular distances has been correlated with the reduction in the intensity of the NH_3 $^+$ torsional modes for L-alanine. In general, high pressure behaviour resembles the effect of low temperature, and for some high symmetry systems it may be even identical. However, in the case of α-glycine, there is decrease in intensity at higher pressures as well as higher temperatures. Though in both the cases there is decrease in intensity, in the case of high temperature there is broadening of this mode and at higher pressures it becomes too weak to be observed.

The decrease in intensity of the ND_3 $^+$ torsional mode at higher pressure is also accompanied by discontinuous changes in some of the modes corresponding to the other COO^- and ND_3 $^+$ modes as can be seen from figure 2.8. This indicates that there may be a subtle structural rearrangement in the glycine molecule which can possibly influence the inter-layer hydrogen bond length. However, the pressure induced stiffening of the N-D stretching mode can not be unambiguously correlated with increase in the corresponding hydrogen bond length without the knowledge of hydrogen bond parameters at high pressures. Similarly, the molecular reorientation may also result in substantial changes in the C-H- - -O bond length. X-ray diffraction studies of undeuterated α-glycine have indicated possible reduction in the C-H- - -O hydrogen bond length. The hydrogen bonds C2-H1- - -O1 and C2-H1- - -O2 (H1- - -O1=2.488 Å; H1- - -O2=2.559 Å) at ambient conditions are found to strengthen at 6.2 GPa (H1- - -O1=2.25 Å; H1- - -O2=2.28 Å). However, C-H/C-D stretching modes are found to stiffen at higher pressures. As in general compression brings the molecules closer, vibrational modes under pressure stiffen under pressure in the absence of any structural transition. Upon increase in the hydrogen bond strength, the covalent C-D distances are expected to elongate, C-D modes are expected to soften (red shift) if we use spectroscopic behaviour of proper hydrogen bonds [224]. However, with more spectroscopic data available in the literature on various compounds, other types of (improper) hydrogen bonds which blue shift (stiffen) have also been reported [223]. In these hydrogen bonds, a reorganization of electron density distribution around the bond is found to be responsible for the contraction of the

covalent bond involved in the hydrogen bond formation. However, whether the pressure induced stiffening of C-H and N-H stretching bands is a consequence of compression or blue shifting hydrogen bonds [7, 22, 224, 225] is still a question which remains unanswered and hence neutron diffraction data or detailed theoretical calculations which can give hydrogen bond parameters would be required.

2.7   Conclusion

High pressure Raman studies suggest subtle structural rearrangements in fully deuterated α-glycine across 3 GPa. Under pressure, competing interaction of intra layer N-D- - -O hydrogen bond with the emerging interlayer C-D- - -O hydrogen bonds result in conformational changes of the molecular units with subtle structural modifications and inhibit any drastic change in the crystal symmetry. The pressure induced changes in ND_3^+ torsional mode are very similar to that of undeuterated glycine. The observed spectral changes are found to be completely reversible. As one can see from table 2.1, spectroscopic investigations of many amino acids have indicated structural rearrangements in the pressure range less than 5 GPa. Recent investigations on amides also show transitions around 3 GPa [226–228]. It would be of interest to see whether this pressure range is the threshold value of various amino groups to reorient themselves under pressure. In the case of γ-glycine, [180–185] L-serine [199, 213, 214] and L-Cysteine [196, 211, 212] pressure induced changes in the hydrogen bonding interactions are found to be quite significant while in other amino acids subtle rearrangements are reported. Amino acids constitute a variety of hydrogen bonds, linear, bifurcated, bent, *etc.*, In most of these amino acids pressure induced changes in these modes in terms hydrogen bonds have not been understood so far. In some of the amides such as PA66 (polyamide) which has NH_2 groups, NH stretching mode is found to soften under pressure and the overall N- - -O distances were found to reduce at higher pressures [226]. If the spectroscopic parameters are accompanied by corresponding hydrogen bond distances and angles, a very useful correlation can be obtained, which can be extended to compounds with various amino

groups such as amides, amines, *etc*. Neutron diffraction and detailed theoretical calculations would therefore be very useful to understand the high pressure spectroscopic behaviour of compounds with various amino groups and their hydrogen bonds.

Chapter 3

Hydrogen Bond Vs Polymerization: Acrylamide

3.1 Introduction

Compression of materials facilitates close packing, molecular reorientations and rearrangements, consequent variations in the nature of chemical bonding which can result in new structures and properties. Hydrogen bonded materials are found to undergo pressure induced structural changes with a wide range of variations in hydrogen bonds, from subtle rearrangements in the hydrogen bonding networks to drastic changes such as making and breaking of hydrogen bonds, proton disorder, symmetrization etc. [229–237] In the case of molecular solids with high carbon to hydrogen ratio, unsaturated bonds of the molecules tend to be saturated by linking to each other resulting in polymerization. Pressure induced polymerization can therefore be a promising alternative to synthetic chemical routes as there is no need of any initiator or solvent and one can obtain polymerization without any impurities. Hydrogen-bonded network in polymorphic compounds using high pressure can provide more information about the hydrogen bonding network and also help in the study of transformation between existing polymorphs. In addition, the resultant polymer obtained may have new properties which are not accessible through synthesis under ambient condition.
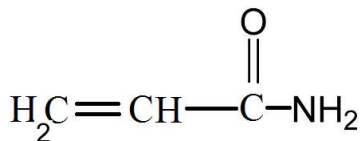
Figure 3.1: Chemical structure of acrylamide

3.2   Motivation

Polymerization of acrylamide by chemical methods, [238–240] shear deformation, x-ray ir-radiation and shock wave loading *etc.* have been reported in the literature [241–247]. Solid state polymerization under x-ray irradiation are reported to be brought about by absorption of radiation and generation of free radicals which react further to form polymer [241]. Under shear deformation, polymerization takes place in the presence of free radicals where mechan-ical stress are concentrated [243]. It would be of interest to investigate pressure induced polymerization of acrylamide to get an insight in to the possible mechanism of polymeriza-tion under pressure. High pressure Raman and infrared absorption studies are ideal to get a first hand information on polymerization of materials under pressure [248–250]. Except for a brief report of high pressure infrared absorption studies of acrylamide by Bradbury *et. al.* [242] which indicate solid state polymerization of acrylamide after successive compression and decompression cycles of ~5 GPa, no detailed high pressure investigations, in particular, Raman spectroscopic and structural investigations are available so far.

As acrylamide (shown in figure 3.1) is hydrogen bonded amide, its high pressure investi-gations are also important from the point of view of studying hydrogen bonds under pressure. It is well known pharmaceutical agent, carcinogen in food products, extensively used in indus-tries and biological procedures for DNA sequencing. Among many of the hydrogen bonded amides, formamide has been extensively studied under pressure using both spectroscopic and x-ray diffraction studies [251–253]. Single crystal X-ray diffraction study [253] of formamide suggests a new β phase with denser packing but same space group at pressure ~0.88 GPa by reconstruction of N-H- - -O hydrogen bond along with the formation of new C-H- - -O type hydrogen bonds. Acetamide [254] Polyamide PA 66 [255] and oxamide [256] are other
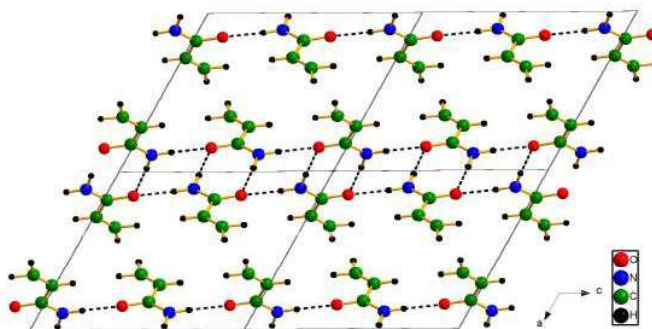
Figure 3.2: Crystal structure of acrylamide; dotted lines represent hydrogen bonds.

amides in which changes in the hydrogen bonding networks are indicated by Raman or infrared spectroscopic studies. Variations in hydrogen bonds of acrylamide are also reported in brief by an infrared absorption study carried out up to 5 GPa [242]. We have carried out high pressure Raman investigations of acrylamide up to ~17 GPa which give insight in to the structural changes brought about reconstruction of hydrogen bonds under pressure and onset of polymerization at further higher pressures.

3.3   Structural Details

At ambient conditions acrylamide (C_3H_5NO), exists in monoclinic structure with space group $P2_1/c$ with four formula units in per unit cell and with lattice constants are $\mathbf{a}$=8.408 Å, $\mathbf{b}$=5.792 Å, $\mathbf{c}$=9.777 Å, β=1180 34' [257]. Figure 3.2 shows the crystal structure of acrylamide. While molecular state of acrylamide is found mainly as trans monomer, solid state acrylamide exists in hydrogen bonded dimeric form where intra-dimer [N-H1- - -O, H1- - -O=2.947 Å] combine acrylamide molecules into centro-symmetric dimers and inter-dimer [N-H2- - -O, H2- - -O=2.847 Å] hydrogen bonds connect two nearest dimers [241].

3.4   Experimental Details

Polycrystalline samples of acrylamide purchased from Sigma-Aldrich Co. were loaded in the hole of diameter ∼120 μm of a stainless steel gasket which was pre-indented to a thickness ∼80 μm in a Mao-Bell type of diamond anvil cell (DAC). Experiments were carried out without pressure transmitting medium in order to avoid interaction with the sample. Diode pumped solid state laser of 532 nm wavelength was used to excite the sample. Pressure was monitored by the R-lines of ruby fluorescence and pressure was calculated for quasi-hydrostatic condition [153]. All measurements were recorded in backscattering geometry. Single stage Jobin-Yvon HR460 spectrograph with nitrogen cooled CCD and entrance slit of 100 μm were used to record spectra. Raman Spectra of polycrystalline acrylamide were recorded up to ∼17 GPa during compression. The spectra of retrieved samples of acrylamide after 10 successive cycles of compression-decompression to ∼5 GPa and ∼2 GPa and a single pressure cycle of 17 GPa were also recorded.

3.5   Results and Discussion

We have recorded Raman spectrum of acrylamide at different pressures (0.1 MPa -17 GPa) in the entire spectral region of interest from 200-3400 cm^{-1} except 1300-1400 cm^{-1} where strong Raman mode of diamond exists. The observed Raman spectrum at ambient conditions is consistent with the spectra reported earlier in the literature [239, 258–260] and the assignments of various modes have been taken from these references. Raman modes in the pressure range 0.1 MPa-2.8 GPa in the spectral region 200-1200 cm^{-1}, 1400-1800 cm^{-1} and 2800-3400 cm^{-1} are shown in figure 3.3. Figure 3.4 show high pressure Raman spectra (4 GPa-17 GPa) in the spectral region 200-1200 cm^{-1}, 1400-1800 cm^{-1} and 2800-3400 cm^{-1} respectively. Figure 3.5 gives the frequency versus pressure curve of all the Raman modes observed at different pressures. We also recorded Raman spectra of acrylamide retrieved after 10 compression-decompression pressure cycling of ∼5 GPa and ∼2 GPa. Figure 3.6 give the Raman spectra of the retrieved samples after successive compression-decompression

cycles of 2 GPa, $\sim$5 GPa and a single pressure cycle of $\sim$17 GPa which are in all the three spectral regions. In the following sections, we have catalogued all the pressure induced spectral changes in acrylamide.

3.5.1 Spectral Changes up to 2.8 GPa

As shown in figure 3.3 (a), up to 1.4 GPa, the discontinuous changes in the relative intensity of C-O torsional mode (508 cm^{-1}), splitting of CH$_2$ rock (1056 cm^{-1}) are some of the spectral changes noted in this spectral region. A shoulder peak emerges close to CH$_2$ deformation mode (1148 cm^{-1}) emerges at 2.6 GPa and is well resolved at further higher pressures. As shown in figure 3.3 (b), the decrease in the relative intensity of NH$_2$ deformational mode (1582 cm^{-1}) and increase in its width, splitting of C=O stretching mode (1680 cm^{-1}) are some of the spectral changes observed in the pressure range 1.4 - 2.8 GPa. New modes at 1450 cm^{-1} and 1648 cm^{-1} (marked as *) which emerge at $\sim$1.4 GPa are clearly visible at higher pressures. As shown in figure 3.3 (c), the relative intensity of the CH$_2$ (ν_s) symmetric stretching mode (3036 cm^{-1}) with respect to CH$_2$ asymmetric stretching mode (3105 cm^{-1}) and CH stretch (3013 cm^{-1}) decreases drastically up to 1.4 GPa. Above this pressure, new modes (3040 cm^{-1}, 3138 cm^{-1}) (which are marked as *) appear adjacent to both CH$_2$ symmetric and asymmetric stretching modes and their relative intensity increases at the cost of CH$_2$ stretching modes of the initial phase. NH$_2$ symmetric mode (3165 cm^{-1}) softens up to $\sim$2 GPa and shows a discontinuous jump to a higher value (3260 cm^{-1}) at 2.6 GPa and is too weak to be followed beyond 2.8 GPa.
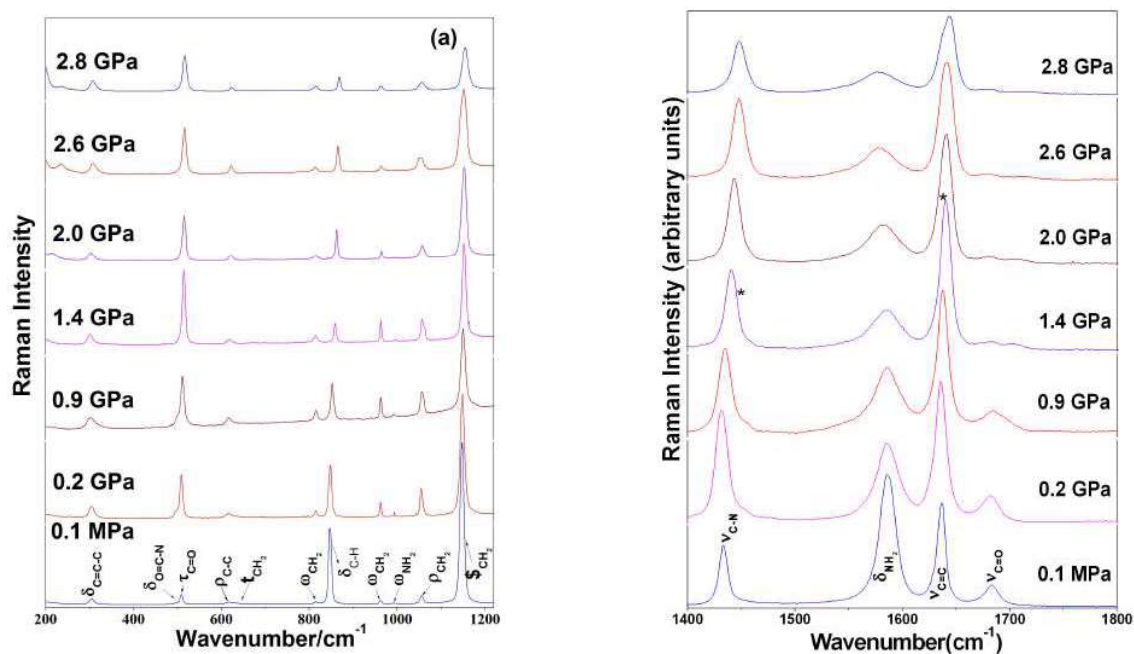
(a) 100-1200 cm^{-1}; τ torsion; δ bending (deformation); ρ Rocking; t twisting; ω wagging; $ scissoring;

(b) spectral region 1400-1800 cm^{-1}; δ bending (deformation) ; ν stretching; * indicates new peaks;
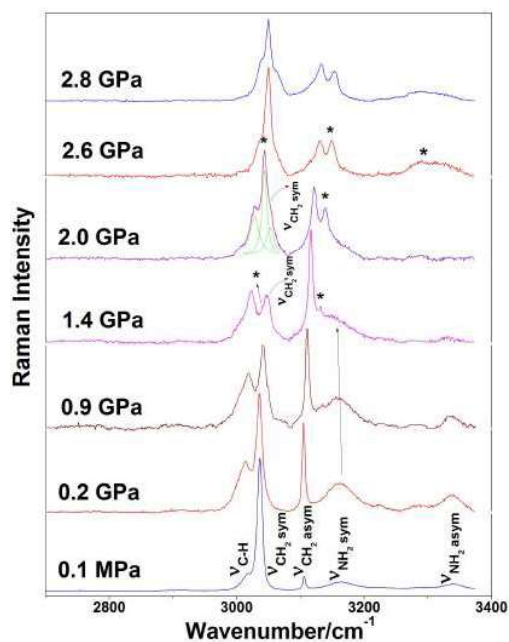
(c) in the spectral region 2800-3400 cm^{-1} ; ν stretching; * indicates new peaks; convoluted peaks are shown to distinguish the new peak.

Figure 3.3: Raman spectra of acrylamide in the pressure range 0.1 MPa - 2.8 GPa in the spectral region

3.5.2 Spectral Changes above 4 GPa

Figure 3.4 (a) shows emergence of several new modes (324 cm^{-1}, 531 cm^{-1}, 1078 cm^{-1}, 1109 cm^{-1} and 1148 cm^{-1}) at 4 GPa and the relative intensities of these new modes are found to increase with pressure. There are also discontinuous changes noted at 8 GPa in the pressure induced variation of relative intensity and Raman shifts of many of the observed Raman modes. As shown in figure 3.4 (b), NH$_2$ deformational mode is found to be highly asymmetric at pressures above 4 GPa and is found to soften and get merged with C-N stretching mode at $\sim$17 GPa. C=C stretch is found to split and is found to be highly asymmetric at pressures above 14 GPa. As seen from figure 3.4 (c), CH stretching and CH$_2$ symmetric modes are merged in to one broad band and relative intensity of the CH$_2$ asymmetric stretch is found to reduce at higher pressures. However, at 14 GPa, the relative intensity of the CH$_2$ asymmetric stretch is found with increased relative intensity. At $\sim$17 GPa a broad band emerges close to the CH stretching band. On release of pressure from $\sim$17 GPa, this broad band ($\sim$2900 cm^{-1}) appears with increased intensity in addition to the CH, CH$_2$ and NH$_2$ stretching modes of the ambient phase of acrylamide as shown in figure 3.6. The above mentioned pressure induced spectral changes are interpreted in terms of structural variations in acrylamide under pressure in the following sections.

Structural Transformations and Hydrogen Bonds Across 2.6 GPa

As one can see from the high pressure Raman spectra of acrylamide, NH$_2$ symmetric stretching mode (3165 cm^{-1}) shows red shift (softens) and is observed at 3136 cm^{-1} at 2.2 GPa and a discontinuous jump of $\sim$124 cm^{-1} to a higher value (3260 cm^{-1}) is noted at $\sim$ 2.6 GPa. In general, pressure induced softening of N-H stretching modes is correlated with the strengthening of N-H- - -O hydrogen bonds [261]. The softening of the NH$_2$ stretching modes in acrylamide and a discontinuous jump to a higher value suggests that N-H- - -O hydrogen bond which initially gets strengthened is broken and a relatively weaker bond is reconstructed at $\sim$2.6 GPa. However, it may be noted that correlation of vibrational modes with the strength of hydrogen bonds is highly system specific [7]. The above mentioned
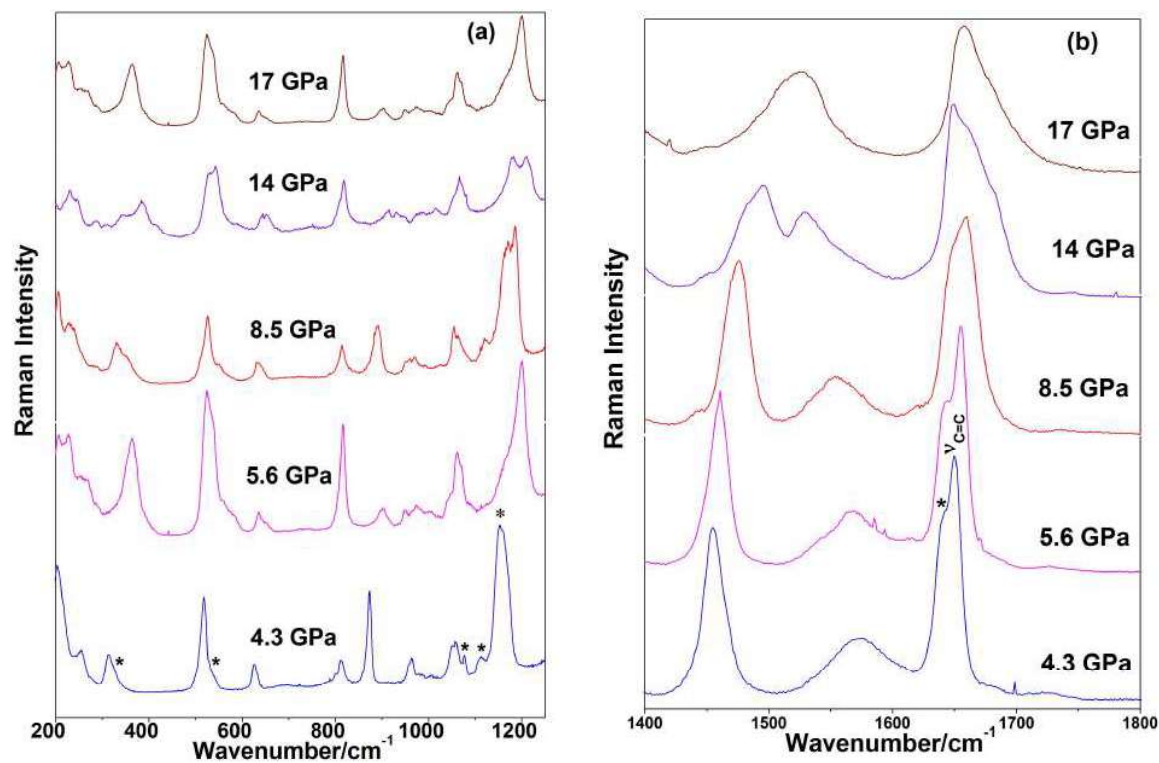
(a) Spectral region 100-1200 cm^{-1}; * indicates new peaks;

(b) Spectral region 1400-1800 cm-1 ;
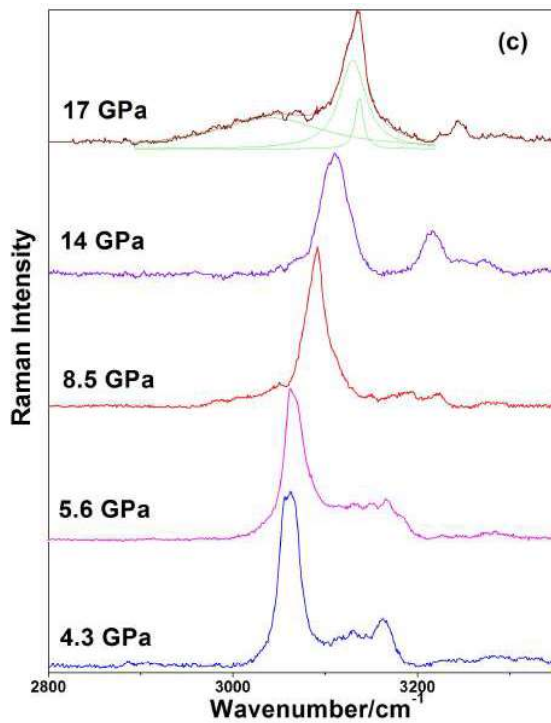
(c) in the spectral region 2800-3400 cm^{-1}

Figure 3.4: Raman spectra of acrylamide in the pressure range 4.3 - 17 GPa;

(a) 200-1200 cm^{-1}

(b) 1400-1800 cm^{-1};

(c) 2800-3400 cm^{-1}
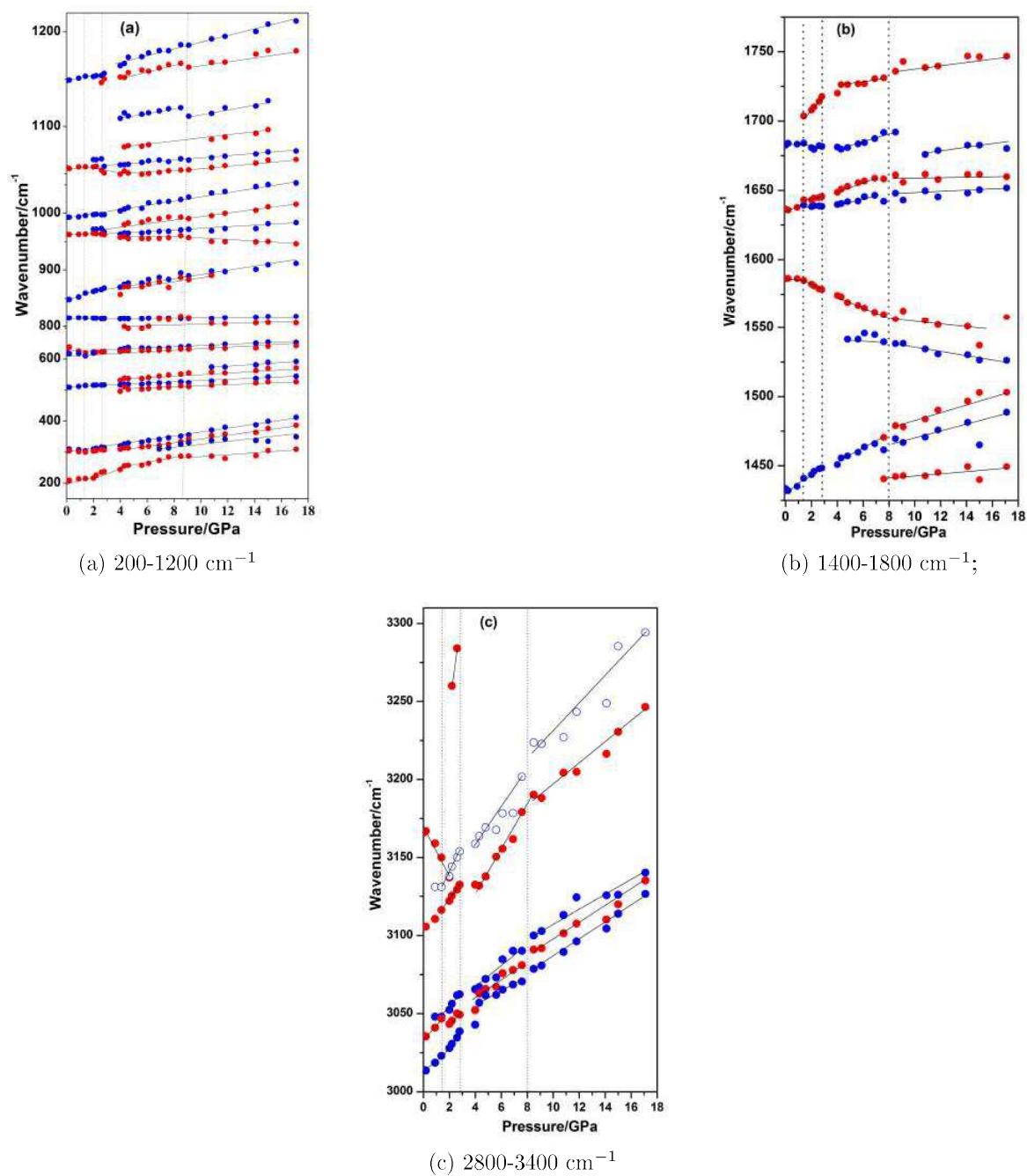
Figure 3.5: Pressure induced variation of Raman shifts in the spectral region; Lines are drawn as a guide to the eyes.

spectral changes indicates the new N-H- - -O hydrogen bonding network are formed at pressure ~2.6 GPa. Above 2.8 GPa, the relative intensity of NH_2 symmetric stretching mode is too low to be discernible. However, a qualitative idea of changes in the N-H- - -O hydrogen bonds may be revealed by the high pressure behavior of NH_2 bending mode. The variation in the NH_2 bending mode upon hydrogen bonding is expected to be opposite to that of the corresponding NH_2 stretching mode. The peak position of NH_2 bending mode in acrylamide is nearly constant up to 1.4 GPa. Above this pressure, there is a large pressure-induced broadening of this mode, and it becomes highly asymmetric at higher pressures. In the pressure range 1.4-2.6 GPa we note that higher wavenumber component of this mode remain nearly constant and the lower wavenumber component continue to soften. This suggest that the pressure-induced variation in the two hydrogen bonds which make up the acrylamide structure becomes diverse in the new phase, where one of the hydrogen bonds becomes weaker, and other may continue to remain stronger. In the new phase, it is also possible that reconstruction of N-H- - -O hydrogen bonds result in the strengthening of C-H- - -O interactions as reported for formamide [253]. However, without explicit determination of H-atom positions in the high pressure phase, possibly through neutron diffraction or theoretical calculations, it is difficult to ascertain the nature of changes in the C-H- - -O hydrogen bond.

The observed spectral changes in the NH_2 vibrational modes are also accompanied by the emergence of new modes adjacent to the CH_2 symmetric and anti-symmetric stretching modes (marked as ⋆ in figure 3.3 (c)) at 1.4 GPa. The relative intensity of these new modes with respect to the CH_2 symmetric and anti-symmetric stretching modes of the ambient phase increases up to 2.6 GPa. These spectral changes indicate that underlying structural transformation may involve changes in the site symmetry of the CH_2 molecular unit of acrylamide due to the reconstruction of hydrogen bonds which is initiated at ~1.4 GPa and completed at ~2.6 GPa. This may be because symmetry-dependent acrylamide molecules, which were connected by the N-H- - -O hydrogen bonds into centro-symmetric dimers, are no more symmetry dependent in the new phase.
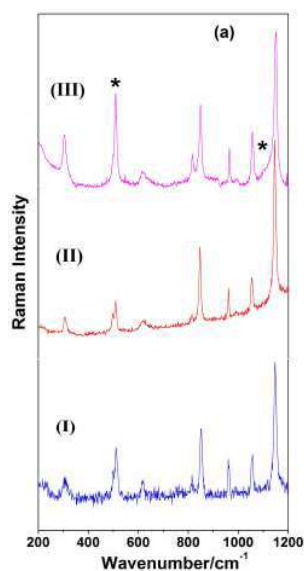
(a) 100-1200 cm^{-1};
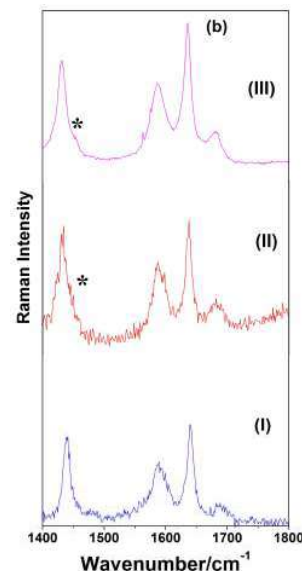
(b) 1400-1800 cm^{-1};
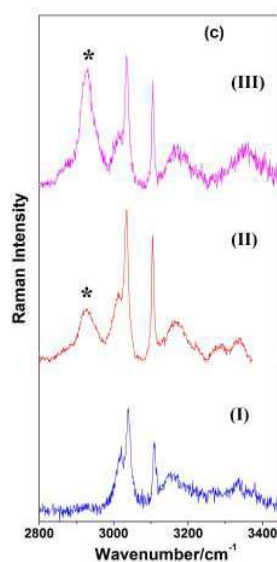
(c) 2800-3400 cm^{-1};

Figure 3.6: Raman spectra of the retrieved sample in the spectral region; **I** 10 pressure cycles of 2.0 GPa; **II** single compression-decompression cycle of 17 GPa; **III** 10 pressure cycles of 5 GPa.

3.5.3   Pressure-Induced Polymerization of Acrylamide

The spectral features which emerge at pressures above $\sim$4 GPa such as new modes at 324 cm^{-1}, 531 cm^{-1}, 1078 cm^{-1}, 1108 cm^{-1} and 1150 cm^{-1} (marked with $\star$ in figure 3.4) are very close to the Raman modes reported for a solid linear polyacrylamide [239]. The Raman modes observed at 1164 cm^{-1} and 1648 cm^{-1} (shoulder to the C = C mode) are analogous to polymer skeletal vibration [239, 262] and amide I band [262] of polyacrylamide, respectively. The relative intensity of the C = C mode of acrylamide is found to decrease significantly with respect to the amide I band at pressures above 4 GPa. A weak and broad band appearing at the lower side of the CH stretching modes at $\sim$17 GPa is analogous to the characteristic polymer band [239, 262, 263] with sp^3 hybridization. It may be noted that though many spectral features suggest onset of polymerization even at $\sim$4 GPa, the relative intensity of the characteristic polymer band is not found to increase much under compression until $\sim$17 GPa. However, on decompression from $\sim$17 GPa, as one can see from figure 3.6, the characteristic polymer peaks of polyacrylamide are observed with increased relative intensity. These observations suggest that significant proportion of acrylamide monomer undergoes polymerization during decompression. However, persistence of Raman modes of acrylamide shows that polymerization is not yet complete. Earlier infrared absorption studies of acrylamide have reported that repeated ten cycles of compression and decompression increases the fraction of polymer phase that can be retrieved from the monomer [242]. There were no details of the nature of the polymer phase reported in the above mentioned study. Polymer obtained by chemical methods (using ammonium persulfate as reaction initiator and tetramethyl-ethylenediamine as a catalyst) [238–240] with crosslinker was found to be a gel and the one without the crosslinker was a solid linear polymer. The polyacrylamide retrieved through pressure-induced polymerization is found to be a solid polymer rather than a gel as it is an addition polymerization. We have recorded the Raman spectra of the polymer phase after ten cycles of compression-decompression of acrylamide up to $\sim$5 GPa. One can see from figure 3.6 that higher fraction of polymer phase is obtained in this case as reported by the earlier infrared absorption study [242]. However, compression-decompression cycles of
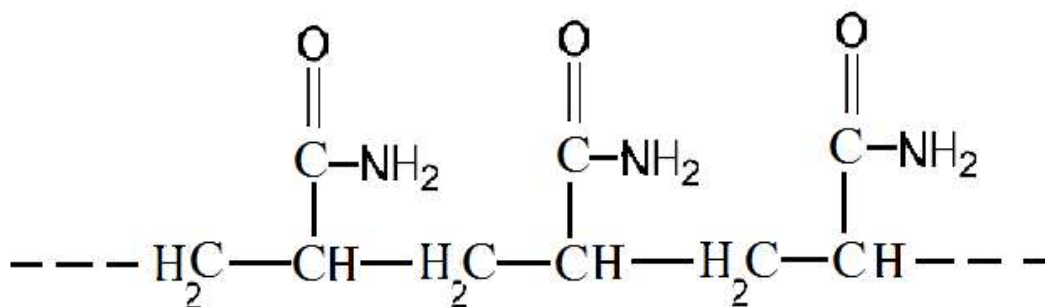
Figure 3.7: Molecular structure of polyacrylamide

acrylamide up to ∼2 GPa do not yield any polymer phase (figure 3.6). This indicates that transformation to the high pressure phase at pressures above 2.0 GPa may play a key role in the polymerization. The high pressure behaviour of acrylamide is similar to that of benzene, acetylene, etc, where significant fraction of the monomer is found to polymerize on release of pressure [42, 248]. In the case of benzene, it is reported that chain formation is inhibited because of very small inter-molecular volume, i.e. the open space, and this may be the reason for lower relative intensity of characteristic polymer band during compression [248]. On release of pressure, density is low, and intermolecular volume is sufficient to form bond and hence the characteristic C-H polymer band corresponding to the polymer was observed with increased intensity on full release of pressure. Molecular structure of polyacrylamide is shown in the figure 3.7.

High pressure investigations of polymerization in several materials reported so far indicate diverse mechanisms of polymerization under pressure [42, 248–250, 264]. A low density polyethylene is retrieved when ethylene is pressure cycled from 3 GPa whereas a high density crystalline polymer is obtained at 1 GPa when an optical catalyst is used [264]. In the case of acrylic acid, polymerization is noted at pressures above 8 GPa, and on release, it is found to have substantial fraction of oligomers of acrylic acid [249]. Benzene is reported to undergo complete polymerization after compression-decompression cycles of 50 GPa [248]. While some materials like ethylene irreversibly polymerize under compression, other materials like benzene undergo significant polymerization only on decompression. In the light

of these observations, high pressure x-ray/neutron diffraction studies of acrylamide will be helpful to understand the influence of the high pressure crystal structure and packing on the mechanism of polymerization in this material under pressure.

Recently, a high pressure infra-red study on acrylamide has shown initial strengthening of N-H- - -O hydrogen bonds under pressure. However, only subtle changes has been reported in N-H- - -O hydrogen bonds [265]. This study also confirms the onset of pressure induced polymerization across 4 GPa. In agreement to our result, multiple high pressure cycles produce greater fraction of polyacrylamide [265].

3.6 Conclusion

Our high pressure Raman investigations carried out up to ∼17 GPa under quasi-hydrostatic conditions reveal significant changes in the inter-molecular interactions in acrylamide under pressure. The spectral changes across 1.4-2.6 GPa indicate substantial structural variations which are brought about by the reconstruction of the N-H- - -O hydrogen bonding networks. Pressure-induced softening of the NH_2 stretching mode and observation of a new mode with a large blue shift at 2.6 GPa indicate breaking of the stronger N-H- - -O bond of the initial phase and formation of a relatively weaker N-H- - -O bond in the new phase. The spectral features observed at pressures above 4 GPa indicate possible onset of polymerization. The characteristic CH_2 polymer bands of polyacrylamide are discernible only at pressures ∼17 GPa. The increase in their relative intensity on release suggests that higher fraction of polymer is formed on decompression.

Chapter 4

Hydrogen Bond Vs Ionic Form: Imidazole

4.1 Introduction and Motivation

Imidazole ($C_3H_4N_2$), a white organic solid that is soluble in water has received much of its attention due to its relevance in the biological processes [11, 266] as well as materials research and applications. Imidazole is an integral constituent of amino acid histidine, histamine, biotin, alkaloids, nucleic acid and many other important biological molecules. Histidine, which has an imidazole side-chain, is associated with many protein and enzyme functions. Due to the presence of heterocyclic ring (figure 4.1) and its proton donor and acceptor properties, the derivatives of imidazole have promising applications in biology, electrode design, catalytic membranes, dye-sensitized solar cells, anion exchange membrane, a rare-earth metal free ferroelectric device, *etc.* [12, 267–269]. The mechanism of proton conductivity of imidazole in the solid phase has been explored in both crystalline and amorphous grain boundaries in recent years [11, 12, 270]. Under compression, when the intermolecular distances in a crystalline solid are reduced beyond a limit, steric repulsion necessitates structural transformations through molecular reorientations or rearrangements. As diffusion is hindered under pressure, further compression may lead to structural frustration, resulting in an amorphous
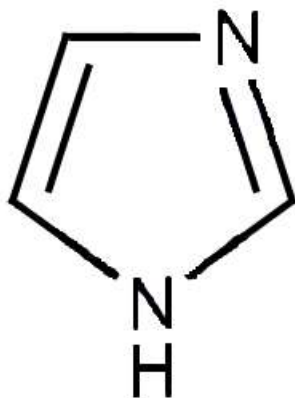
Figure 4.1: Chemical structure of imidazole

phase. [271] The study of pressure-induced structural transformations in imidazole would therefore be of interest in the context of its proton conductivity.

4.2   Crystal Structure

At ambient conditions, imidazole crystallizes in the α-phase (monoclinic, space group P2_1/c with four molecules per unit cell), and its lattice parameters are $\mathbf{a}$ = 7.732(4) , $\mathbf{b}$= 5.458(2) , $\mathbf{c}$ = 9.779(4) , and β = 117.26(3)(see figure 4.2) [13]. The strong intermolecular hydrogen bond N1-H4- - -N2 (H4- - -N2 = 1.83 , N1- - -N2 = 2.86 ; $\angle$ N1-H4- - -N2 = 173°), which is very close to the symmetrization limit, links imidazole molecules to form a layer. Though several molecular systems [272] with short hydrogen bonds have been investigated under pressure, due to high transition pressures, for example in the case of ice, [273] an unambiguous structural evidence of hydrogen bond symmetrization has been a challenge. A recent single crystal study on pyrazole, a heterocyclic system with N-H- - -N network, has reported asymmetric disorder of protons in N-H- - -N hydrogen bonds, leading to symmetry independent molecules favoring cationic and anionic forms at different sites under pressure [274]. Raman scattering measurements provide information on the structure and processes in the time scale of picoseconds and a short range spatial order, in comparison to the time-averaged diffraction measurements of a crystalline system with a long range order.
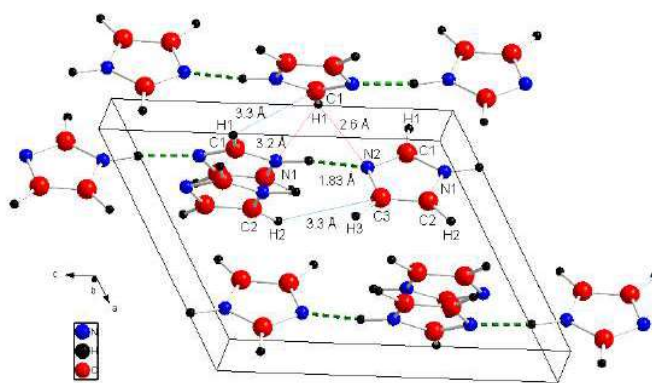
Figure 4.2: Crystal structure of imidazole

Hence, first-hand information on the nature of dynamic hydrogen bonds in low barrier hydrogen bonded systems can be provided by spectroscopic techniques, in particular Raman and infrared absorption studies [275]. Our present studies on imidazole up to 20 GPa aim to look for spectroscopic signatures of possible proton disorder when N-H- - -N distances reach the symmetrization limit (2.554 Å) under pressure.

Moreover, imidazole, being a molecular solid and rich in unsaturated bonds, may become saturated and transform to a polymeric phase under pressure [9, 249, 250]. Among the derivatives/complexes of imidazole which have been investigated under pressure, [250, 276, 277] carnosine is reported to undergo polymerization at pressures as low as ∼2.8 GPa [250]. As the polymer derivatives of imidazole are widely used in electrolytes and other electronic devices, it would be of interest to investigate the possible polymeric interactions in imidazole in the absence of any additional functional groups under pressure and explore its prospective applications.

Besides the material research and applications, imidazole plays an important role in the structure and function of many enzymes, peptides, proteins, and biomolecular complexes [11, 266]. Because of the proximity of heterocyclic rings in imidazole in its molecular solid form, C-H- - -π hydrogen bonding interactions are likely to play an important role under

compression [278,279]. Though C-H- - -π interactions are increasingly realized as the driving forces in the crystal packing of many organic solids and proteins, they are less studied in comparison to the strong O-H- - -O and N-H- - -O hydrogen bonding interactions. Study of imidazole under pressure would therefore be very useful for understanding the nature of C-H- - -π interactions.

We have carried out Raman spectroscopic studies and *ab-initio* calculations on imidazole up to 20 GPa and report here pressure-induced structural changes brought about by the competing N-H- - -N and C-H- - -X (N, π) hydrogen bonding interactions. Figures 4.3 (a,b), 4.4 (a,b) and 4.5 (a,b) show the Raman spectra in the pressure ranges 0.2-5.2 and 5.8-20.1 GPa. Raman shift versus pressure curves of the observed Raman modes at different pressures are given in figures 4.6 (a,b) and figure 4.7 (a,b). The vibrational modes of the crystalline imidazole at different volumes 367 Å^3 (0.1 MPa), 305 Å^3 (3.3 GPa), and 274 Å^3 (6.3 GPa) are shown in figure 4.8. The pressure-induced variation of the calculated lattice parameters and unit cell volume of imidazole up to 10 GPa are shown in figure 4.9. The *ab-initio* calculated N-H- - -N bond parameters, C-H bond lengths, and C-H- - -N, C-H- - -C hydrogen bond lengths and angles at various pressures are shown in figures 4.10, 4.11 and 4.12, respectively. Table 4.1 gives the observed lattice modes at ambient conditions and 10 GPa. The calculated C-H and N-H stretch frequencies and the associated C-H and N-H vibrations are given in table 4.2.

4.3   Experimental Methods

4.3.1   Raman Spectroscopy

Polycrystalline sample of imidazole purchased from Sigma-Aldrich Company was loaded in a hole of diameter ~100 μm drilled in a pre-indented stainless steel gasket of thickness ~60 μm in a Mao-Bell type diamond anvil cell. High pressure Raman spectra were collected in the back scattering geometry using single stage Jobin-Yvon HR460 spectrograph (resolution 4 cm^{-1}) with Liquid Nitrogen cooled CCD. Diode pumped solid state laser of 532 nm wave-

length was used as excitation source. Pressure was monitored by R-lines of ruby fluorescence. Experiments were carried out without any pressure transmitting medium in order to avoid interaction of the sample with the medium. The lattice region 50-200 cm^{-1} of imidazole under ambient conditions was recorded using T64000 spectrograph. The observed spectral changes at higher pressures are likely to be intrinsic rather than due to non-hydrostatic effect as there was no significant increase in the line width of ruby R-lines, which indicates that sample itself acts as a soft medium.

4.3.2   *Ab-initio* calculations

The density functional theory based *ab-initio* calculations were performed using Vienna ab initio Simulation Package (VASP) [280–283]. The exchange-correlation functional was treated with the generalized gradient corrected scheme of Perdew-Burke-Ernzerhof [280]. The interactions between valence electrons and core were treated within the frozen-core all electron projector-augmented-wave (PAW) approach and plane wave basis set was constructed using an energy cut-off of 500 eV. The Brillouin zone (BZ) integrations were carried out using a uniform 6x6x4 Monkhorst-Pack *k-point* grid. All free parameters of crystal lattice were optimized as a function of volume. The Raman spectra were calculated using the density functional perturbation theory as implemented in the Quantum-Espresso computer code [284]. For these calculations local density approximation used for exchange-correlation [285] since code does not allow GGA calculations. An energy cutoff of 160 Ry was used for plane wave expansion. The Brillouin zone was sampled using same Monkhorst-Pack k-point grid as in structural relaxations. The crystal structures were fully optimized before these calculations.

4.4 Result and Discussion

4.4.1 Raman Spectroscopy

Imidazole under ambient conditions is well characterized by Raman, infra-red, theoretical and inelastic neutron scattering methods [286–296]. Imidazole molecule ($C_3H_4N_2$) has (3 x 9) - 6 = 21 vibrational internal modes with C_s point group symmetry. Out of 21 there are 15 in-plane vibrations (A') and 6 are out-of-plane vibrations (A"). These internal modes include 4 stretching vibrations (Γ_{str} = 4 A') three C-H, one N-H stretch and remaining 17 (Γ_{bend} = 11 A'+ 6 A") are ring vibrations. In the monoclinic crystal structure ($P2_1/c$), there are 4 molecules per unit cell; hence there are 21 lattice vibrations (external modes) (6 A_g + 6 B_g+ 5 A_u+ 4 B_u, where A_g, B_g are Raman active and A_u, B_u are IR active). Therefore, in total, there are 12 Raman active external modes and 42 Raman active internal modes out of which about 30 internal modes were observed at ambient conditions as well as at high pressures. The assignment of the observed modes are based on our *ab-initio* calculations and is consistent with that given in the earlier studies [288–294].

Spectral Region 100 - 400 cm^{-1}

Table 4.1 lists the observed lattice Raman modes at ambient conditions and at higher pressures. As high pressure experiments were carried out using single stage spectrograph, except for the mode at 148 cm^{-1} which was observed at ambient conditions, all the other modes became observable only at higher pressures. The extrapolation of their values from ambient conditions recorded using T64000 triple spectrograph (table 4.1) suggests that they are the lattice modes which have stiffened under pressure and have become observable at higher pressures. The mode at 148 cm^{-1} shows relatively larger increase in the frequency ($d\nu/dP$ =27 cm^{-1}/GPa) compared to the other modes in this region. At pressures above $\sim$10 GPa, the relative intensity of the mode close to $\sim$196 cm^{-1} increases substantially with respect to the mode at 177 cm^{-1}(observed at 10 GPa) as can be seen in 4.3 (b).
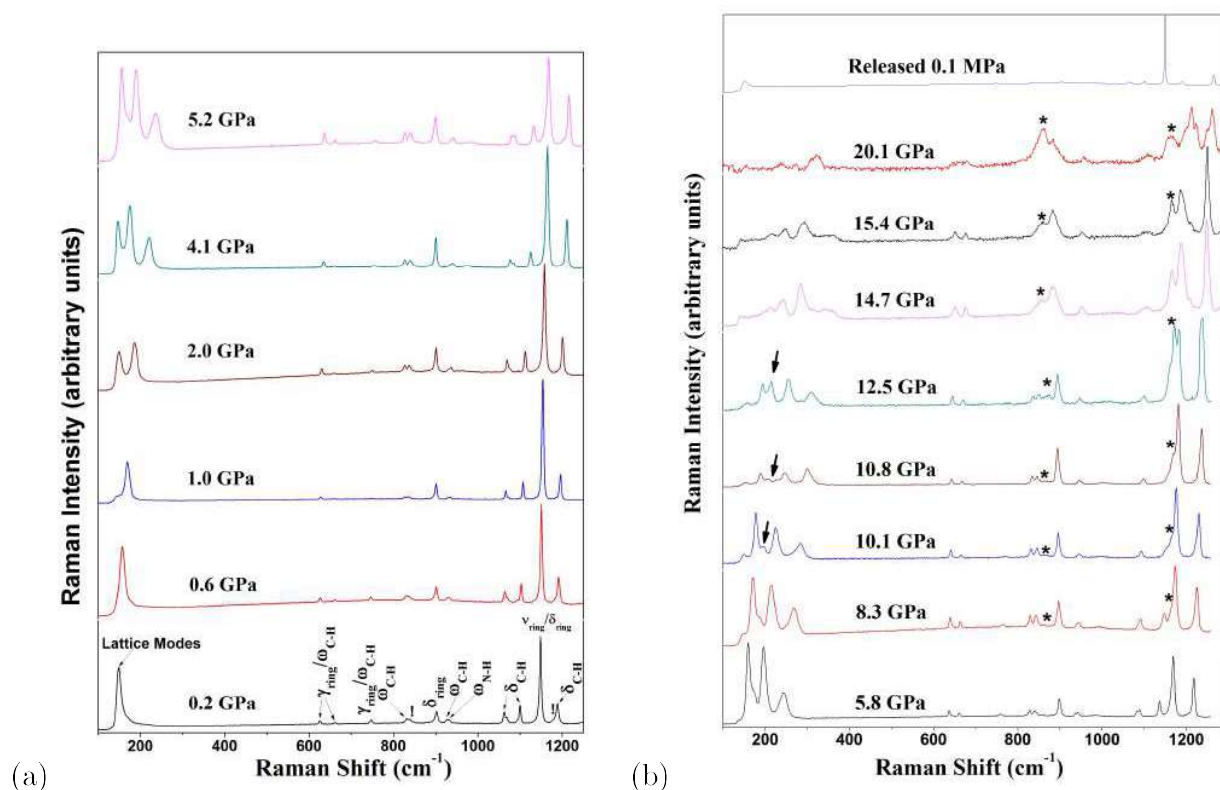
Figure 4.3: Raman spectra of imidazole in the spectral region 150 - 1250 cm^{-1}; (a) pressure range 0.2 - 5.2 GPa; (b) pressure range 5.8 - 20 GPa and on release to 0.1 MPa; δ bending (deformation); ρ rocking; ω wagging; ν stretching; γ pucker; ! unassigned modes; * indicates new peaks.

Observed at 0.1 MPa (cm^{-1})*	Modes at 10 GPa (cm^{-1})	Possible Assignment [291]	Reference [291]
148	282	Hydrogen bonding chain	153
143	227	-	148
112	196	Hydrogen bond bending	114
91/78	177	Hydrogen bond bending	91/78
42/55	150	Hydrogen bond stretching	45/55

Table 4.1: *Ambient spectrum was recorded using triple stage T64000 spectrograph while high pressure spectra were recorded using single stage HR460 spectrograph
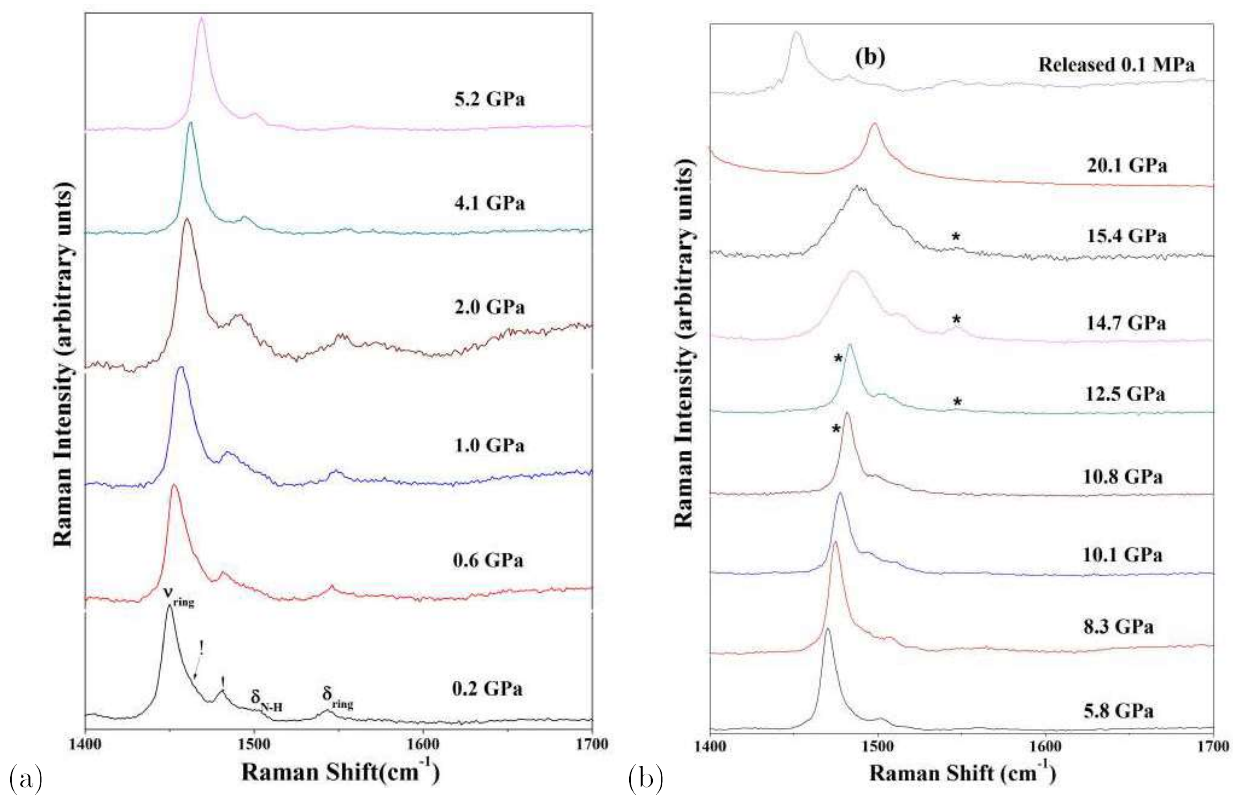
Figure 4.4: Raman spectra of imidazole in the spectral region 1400 - 1700 cm^{-1}; (a) pressure range 0.2 - 5.2 GPa; (b) pressure range 5.8 - 20 GPa and on release to 0.1 MPa; δ bending (deformation); ν stretching; ! unassigned modes;
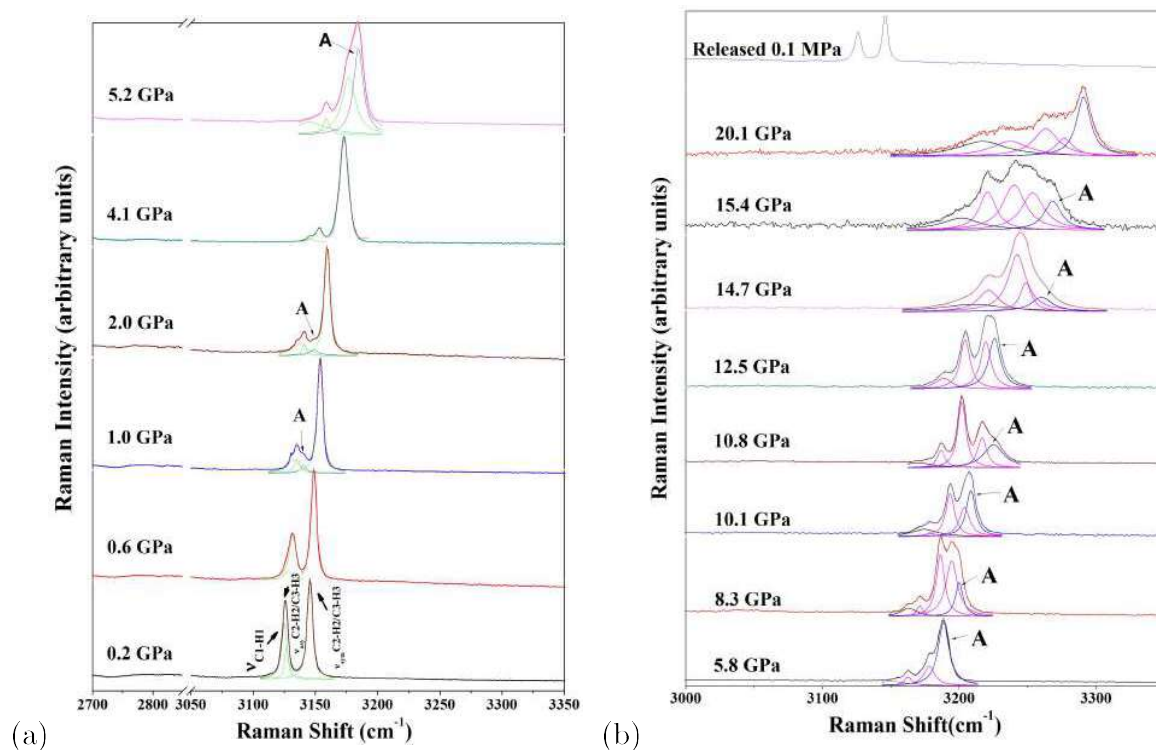
Figure 4.5: Raman spectra of imidazole in the spectral region 2700 - 3350 cm^{-1}; (a) in the pressure range 0.2 - 5.2 GPa; (b) in the pressure range 5.8 - 20 GPa and on release to 0.1 MPa; 'A' indicates the blue shifted C1-H1 symmetric stretching mode;
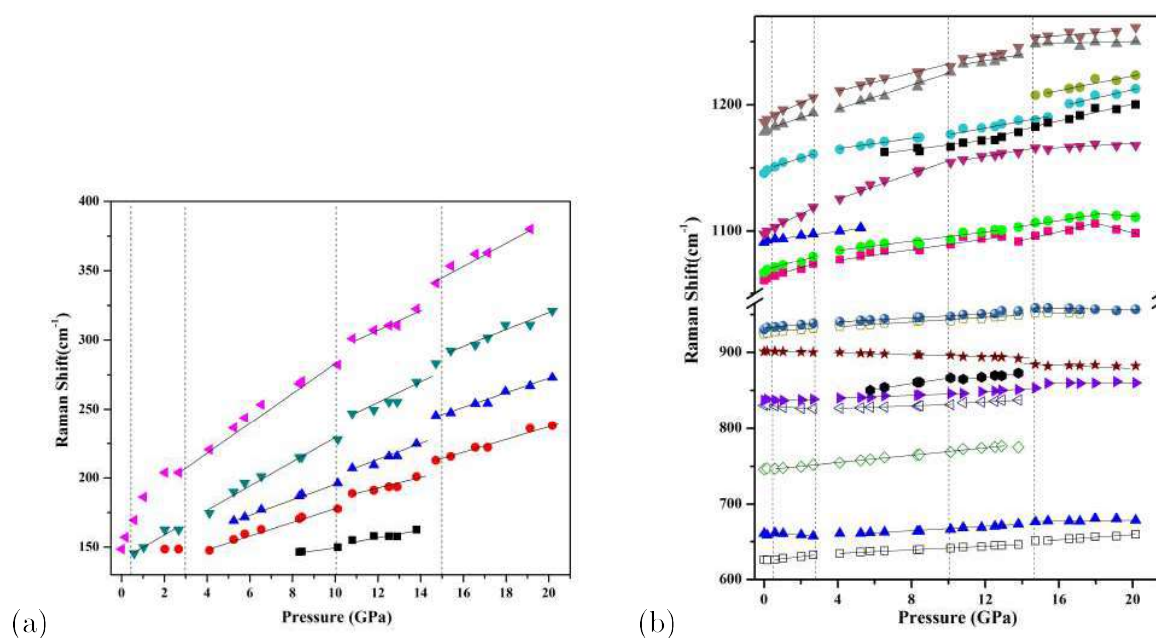
Figure 4.6: Frequency vs Pressure in the spectral region (a) 150-200 cm^{-1}; (b) 200-1250 cm^{-1}; lines are drawn as a guide to the eyes;

Spectral Region 600 - 1700 cm^{-1}

The Raman mode frequencies which shows increase with pressure in the pressure range of our study are R-pucker/C-H wag (623 cm^{-1}, 661 cm^{-1}, 742 cm^{-1}), 836 cm^{-1}(unassigned), C-H wag (924 cm^{-1}), N-H wag (930 cm^{-1}), C-H deformation (1060 cm^{-1} and 1066 cm^{-1}), 1097 cm^{-1} (unassigned), ring stretch/N-H deformation (1145 cm^{-1}), N-H bend (1178 cm^{-1}), C-H/N-H deformation (1186 cm^{-1}), ring stretch (1450 cm^{-1}) and ring deformation (1542 cm^{-1}) (figure 4.6 and figure 4.7). The mode frequencies which decrease with pressure are C-H wag (830 cm^{-1}) and ring bend deformation (901 cm^{-1}). N-H deformation (1500 cm^{-1}), 1480 cm^{-1}(unassigned) softens up to 0.5 GPa and stiffens at higher pressures.
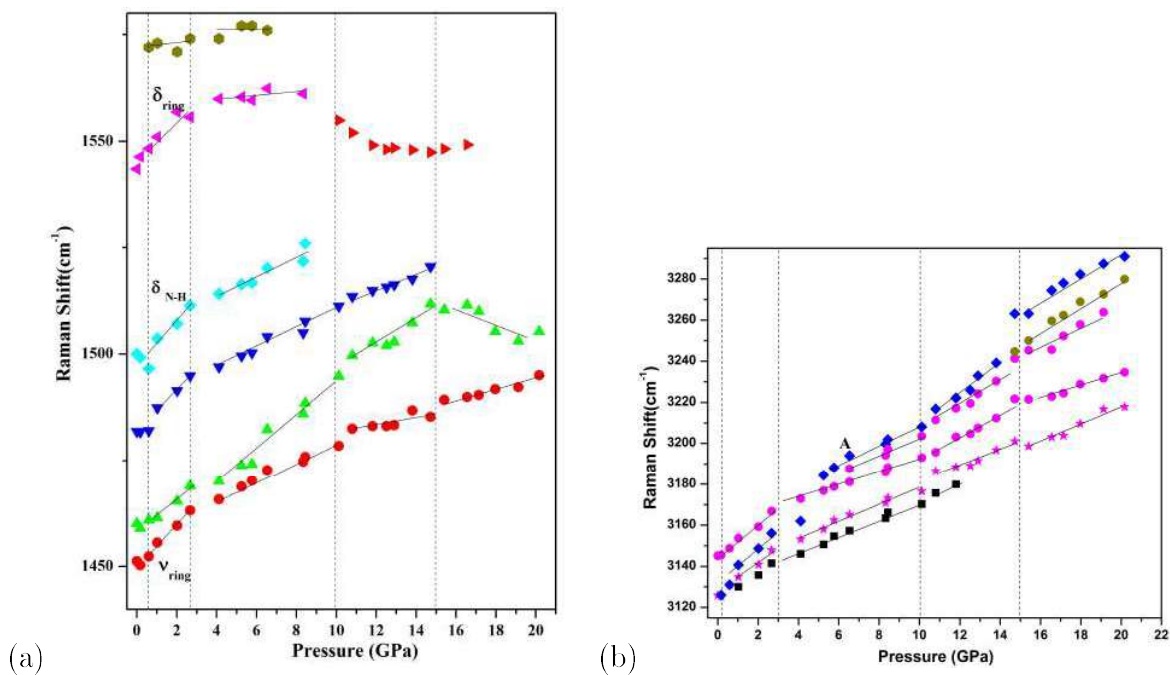
Figure 4.7: Frequency vs Pressure in the spectral region (a) 1400-1700 cm^{-1} and (b) 3000-3300 cm^{-1}; lines are drawn as a guide to the eyes; circles and stars indicate symmetric and antisymmetric stretching (C2-H2/C3-H3) modes respectively.

C-H wag (830 cm^{-1}) softens up to ∼2.6 GPa and shows stiffening at higher pressures, while C-H deformation mode (1090 cm^{-1}) remains observable only up to ∼5 GPa. As shown in figure 4.3 (a), the relative intensity of N-H bend (1178 cm^{-1}) and C-H/N-H deformation (1186 cm^{-1}) with respect to C-H wag (924 cm^{-1}) reduces with pressure and the rate of reduction is found to be higher at pressures above 10 GPa. At pressures above 8 GPa,

reduction in the intensity and softening of NH deformational modes were noted. Across this pressure, new modes $\sim$870 cm^{-1} and $\sim$1160 cm^{-1} emerge and show increase in the relative intensity at higher pressures. At pressures above 10 GPa, new modes close to the ring stretch (shoulder peak 1480 cm^{-1}) and 1550 cm^{-1} emerge and the latter one shows pressure induced softening up to 15 GPa (figure 4.7 (a)). Above this pressure, anomalous spectral changes such as appearance of relatively sharper mode around the ring stretch 1480 cm^{-1} riding over a broad band and disappearance of the new mode (1550 cm^{-1}) were noted.

Spectral Region 3000 - 3400 cm^{-1}

At ambient conditions, three vibrational modes C1-H1 symmetric stretch (3123 cm^{-1}), C2-H2/C3-H3 asymmetric stretch (3125 cm^{-1}) and C2-H2/C3-H3 symmetric stretch (3145 cm^{-1}) modes of imidazole are observed (figure 4.5(a,b)). C1-H1 (3123 cm^{-1}) shows significant reduction in the relative intensity with respect to the C2-H2/C3-H3 (3145 cm^{-1}) in the pressure range 0.5 to 2.5 GPa. At $\sim$1 GPa, a new mode emerges at $\sim$3140 cm^{-1} which gets buried under the C2-H2/C3-H3 mode across 2.6 GPa. Above this pressure, its relative intensity with respect to C2-H2/C3-H3 mode increases with pressure and is well resolved at 5.2 GPa and observed at 3185 cm^{-1}. At $\sim$6 GPa, another new mode, which is possibly due to splitting of C2-H2 and C3-H3 modes, emerges close to C2-H2/C3-H3 and becomes well resolved at higher pressures (figure 4.5 (b)). The C2-H2/C3-H3 asymmetric stretching mode frequency continues to increase with pressure. Across $\sim$15 GPa, a broad band with complex profile emerges around the CH stretching modes.

4.4.2 *Ab-initio Calculation*

The vibrational modes of the crystalline imidazole have also been calculated at different volumes 367 Å^3 (0.1 MPa), 305 Å^3 (3.3 GPa) and 274 Å^3 (6.3 GPa) and are shown in figure 4.8. The pressure induced variation of the lattice parameters and unit cell volume of imidazole up to 10 GPa are shown in figure 4.9. The variation in the cell parameters up to 3 GPa is close to the values reported in the experimental single crystal x-ray diffraction study
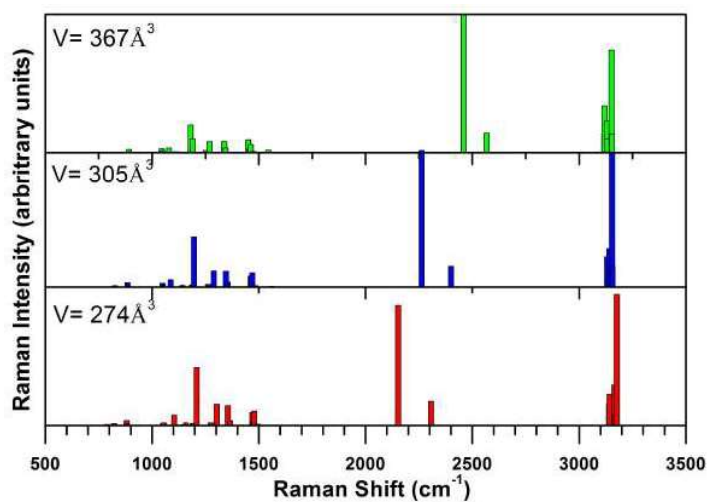
Figure 4.8: Calculated Raman spectra of imidazole at different volumes; 367 Å^3 ($\sim$ 0.1 MPa), 305 Å^3 ($\sim$ 3.3 GPa) and 274 Å^3 ($\sim$ 6.3 GPa).

	367Å^3 Theo. (cm^{-1})	0.1 MPa Exp.(cm^{-1})	305Å^3 Theo. (cm^{-1})	2.7 GPa Exp.(cm^{-1})	274Å^3 Theo. (cm^{-1})	6.5 GPa Exp.(cm^{-1})
N1-H4	2458/2567	-	2262/2399	-	2152/2306	-
C1-H1	3118/3117	3123	3142	3155	3177/3176	3194
C2-H2	3154/3156	3145	3156/3155	3167	3167	3187
C3-H3	3154/3156	3145	3156/3155	3167	3167	3181

Table 4.2: Experimental and Calculated Raman Modes at Different Volumes
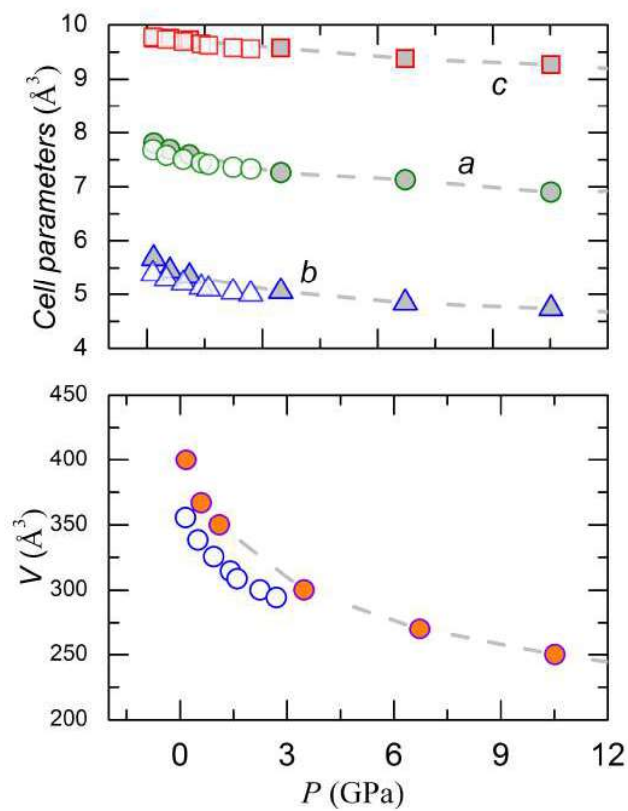
Figure 4.9: *Ab-initio* calculated values of lattice parameters and unit cell volume as a function of pressure; Here solid filled symbols represent calculated values; open symbols are from experimental data of Paliwoda *et. al.* [21]; lines are drawn as a guide to the eyes.

of imidazole [21]. The calculated bulk modulus using Birch-Murnaghan equation of state is ~9.8 GPa.

4.4.3 Structural Changes in the Pressure Range 0.1 MPa - 2.5 GPa

Based on single crystal x-ray diffraction study [21] on imidazole up to 3 GPa, an earlier report established the stability of α-phase up to 2.7 GPa. However a new polar β (orthorhombic) phase was shown to get isochorically recrystallized above 1.2 GPa at 500 K. It is also reported that at ~8-12 GPa, inter-molecular N - - -N distance would reduce to 2.554 Å for H atom to assume the centre position, which would facilitate H atom hopping. Our *ab-initio* calculations indicate non-monotonic changes in the N-H- - -N and some of the C-H- - -N and C-H- - -C parameters at 0.5 GPa suggesting subtle molecular rearrangements across this pressure. In the high pressure Raman spectra, reduction in the relative intensity of the C1-H1 stretching mode with respect to C2-H2/C3-H3 stretching mode are also noted. Across ~2.5 GPa, relative strengths of the calculated inter-layer and intra-layer bond parameters change considerably. This is due to relatively less variation in the compressibility along the **c** axis (intra-layer) with respect to **a** and **b** axis (inter-layer). The discontinuous changes in the Raman modes across ~2.5 GPa may therefore be due to variation in the intra-layer and inter-layer compression. Absence of any new spectral features indicate that there is no structural transformation across this pressure, which is consistent with the earlier single crystal x-ray diffraction study [21].

4.4.4 N-H- - -N Hydrogen Bond and Proton Disorder

The strong intermolecular N1-H4- - -N2 hydrogen bond in imidazole is very close to the symmetrization limit even at ambient conditions. Across 0.5 GPa, nonmonotonic changes in the computed N-H- - -N hydrogen bond parameters are noted (see figure 4.10). This is consistent with the observed discontinuity in some of the spectral features in our study. Though compression up to 0.5 GPa does not result in the strengthening of this hydrogen bond [21], increase in the N1-H4 covalent bond length, reduction in H4- - -N2 and N1-

- -N2 ($\angle$ N1-H4- - -N2) above this pressure indicate increase in its strength at further higher pressures. The computed N-H symmetric stretching Raman mode associated with this hydrogen bond is at ~ 2567 cm^{-1} at unit cell volume 367 Å^3 (close to ambient pressure) (figure 4.8). The lower value can be rationalized to be due to very short hydrogen bond distances [261]. As N-H stretching mode is not observable in the Raman spectra, we have calculated the frequency of this mode at three different unit cell volumes 367 Å^3 (0.1 MPa), 305 Å^3 (3.3 GPa), and 274 Å^3 (6.3 GPa) to understand its behavior under pressure (see figure 4.8 and table 4.2). The pressure induced softening of this mode and the elongation of the N1-H4 covalent bond length (figure 4.10) indicate that H4 moves closer to N2. In addition, N1- - -N2 distances also reduce close to the symmetrization limit.

Recently there have been a number of reports on the proton mobility in the N-H- - -N hydrogen bonded networks. Born-Oppenheimer molecular dynamics (BOMD) simulations on (Dih)2H$^+$ cation (Dih: 4,5-dihydro-1H-imidazole) indicate that the proton is localized at either side of the N-H- - -N network, and the central proton position is due to temporal averaging [297]. The possibility of the proton to tunnel in the N-H- - -N bridge is also reported to increase with the temperature through vibrationally assisted proton tunneling. A recent single crystal X-ray diffraction study [274] on pyrazole under pressure reported asymmetric disorder of protons in N-H- - -N hydrogen bonds, leading to disproportionation favoring the cations at one site and anions at another. Also, it is reported that high temperature increases the distofrtion of the structure and activate the defects [274]. Infrared spectroscopic signatures of proton tunneling in some N-H- - -N networks have also been reported in the literature [297, 298].

The ambient crystal structure of imidazole consists of imidazole molecule in the neutral form. However, at higher pressures, when N1-H4- - -N2 distances reduce close to the symmetrization limit, the energy barrier between the two hydrogen sites will decrease. This provides the opportunity for the hydrogen atom to oscillate rapidly from one well to the other resulting in a proton disorder [299] and emergence of ionic species of imidazole at higher pressures. As can be seen from figures 4.3, 4.4 and 4.5 at pressures $\sim$10 GPa, emer-
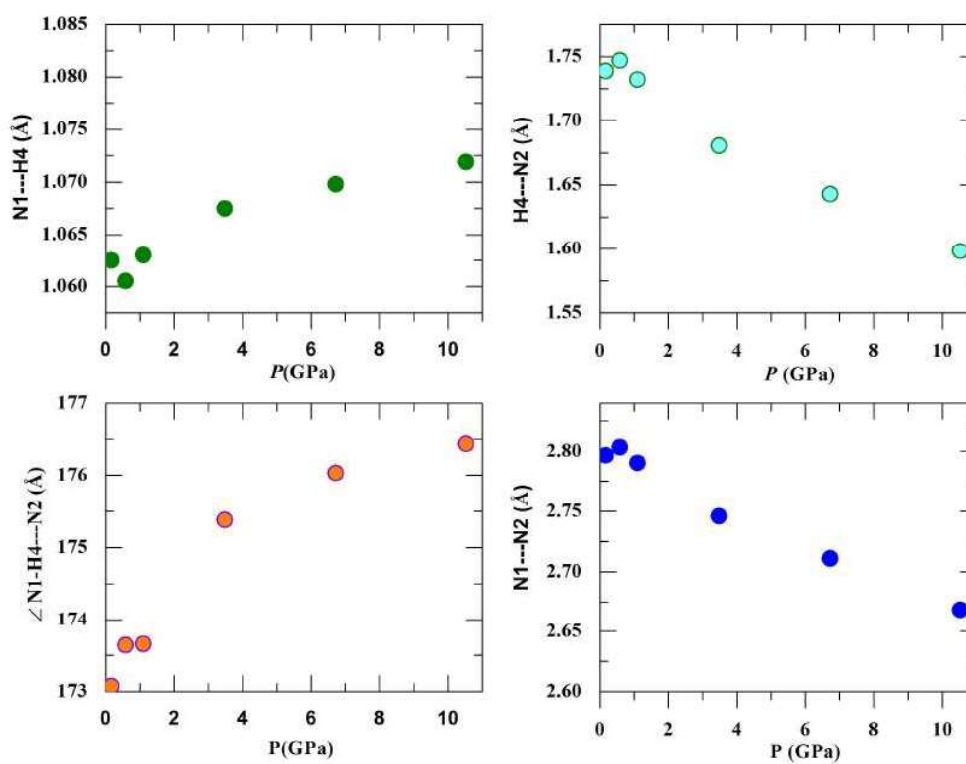
Figure 4.10: *Ab-initio* calculated values of N1-H4- - -N2 parameters as a function of pressure.
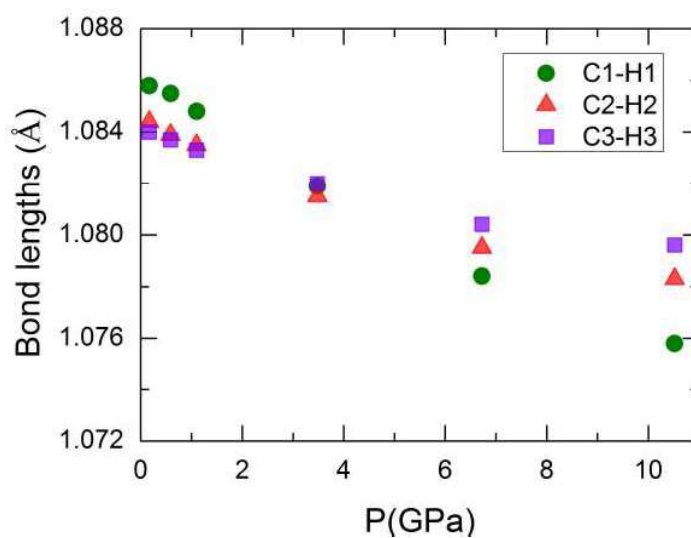
Figure 4.11: *Ab-initio* calculated values of C-H bond parameters as a function of pressure.
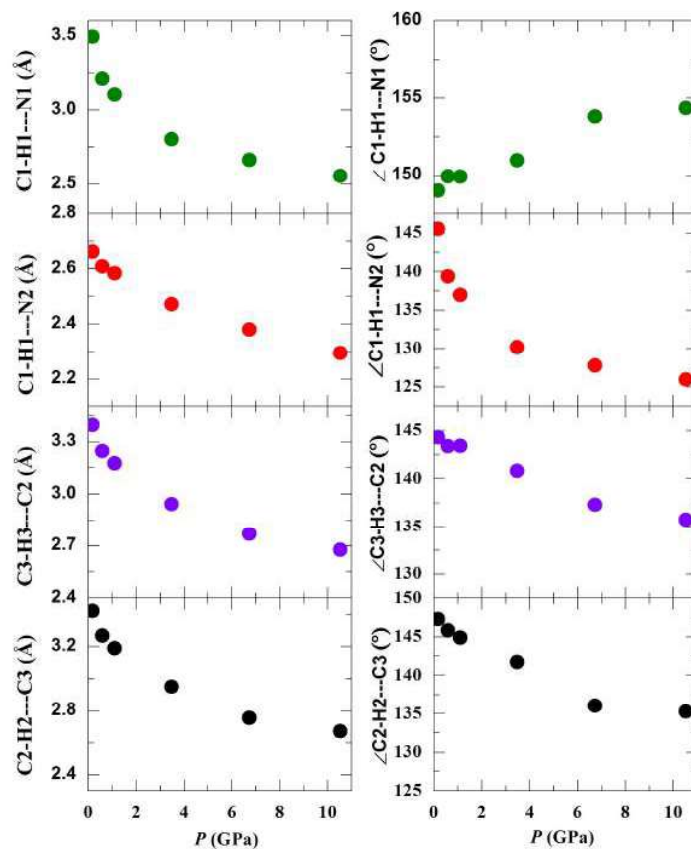
Figure 4.12: *Ab-initio* calculated values of C-H- - -N and C-H- - -C parameters as a function of pressure.

gence and increase in the intensity of the new modes, which resemble the characteristic peaks of the cationic form of imidazole [294], are noted. In addition, the intensity of the mode adjacent to $\sim$196 cm^{-1} (hydrogen bond vibration) [291] increases with respect to the mode at 177 cm^{-1}, which again indicates significant changes in the hydrogen bonded N-H- - -N chains. The new modes observed at 850, 1200, and 1550 cm^{-1} may correspond to N-H wag, C-H wag/H-N=C bend, and H-C=N def. modes of the cationic form of imidazole, respectively [294]. The observation of blue-shifted C-H stretch modes with increase in intensity is also consistent with the formation of imidazolium (cationic form of imidazole) across this pressure [294, 300].

The observed spectral features of cationic form of imidazole across 10 GPa therefore indicate the onset of proton disorder. The C-H stretching modes of anionic form of imidazole are reported to be at lower frequency compared to that of neutral and cationic form [294]. The large spread in the C-H stretching modes at pressures above 12 GPa may be due to the presence of mixed ionic forms of imidazole. However, high-pressure single crystal X-ray diffraction study of imidazole, in particular, above 10 GPa would be very helpful to throw light on this high pressure phase with hydrogen bond disorder [274]. As increase in the ionic conductivity of solid imidazole is attributed to amorphous grain boundaries [268], it would be of interest to determine the conductivity of this high pressure phase. However, all the observed spectral changes are completely reversible. It would also be of relevance to see if the cationic forms of imidazole can be retrieved on pressure release after pressurizing to pressures above 20 GPa, as imidazolium is the preferred state in most of the electronic devices.

C-H- - -X (X = N, π) Hydrogen Bonding Interactions Under Pressure

The cooperative C-H- - -π type interactions between the π electron clouds in the five-membered heterocyclic planar rings and the C-H bonds of the adjacent rings within the layer and between the layer are likely to strengthen when imidazole is compressed under pressure [278, 279, 301, 302]. Spectroscopic signatures of C-H- - -π interactions are diverse

due to varied acid-base interactions and are quite different from that of the strong O-H- -
-O and N-H- - -O interactions. While the latter ones are marked by red-shift of the O-H
or N-H stretch vibrations [303], C-H stretching modes often show blue-shift upon hydrogen
bond formation [304]. The origin of blue-shift has been attributed to dispersion interaction
or the negative sign of dipole moment derivative with respect to the stretching coordinate,
charge transfer, polarization, etc., depending upon the chemical nature of the donor and
acceptors [279, 305, 306].

The geometry of the C-H- - -π hydrogen bond is flexible, and hence the C-H bond may
point to the center of the aromatic ring or any atom of the ring for the interaction. The
range of distances between C-H and ring or any atom of the adjacent rings for the C-H- - -π
interactions to be significant can be 2.6-3.0 Å and angles 134.8^o - 171 ^{o} [278,279]. Among the
intralayer C-H- - -π interactions, the nonbonded C2-H2- - -C3 and C3-H3- - -C2 distances
and angles are 3.28 Å, 144.4^o and 3.292 Å, 143.75^o, respectively (see figure 4.12). These
distances reduce considerably under compression. The $\angle$ C-H- - -C angles also reduce but
are within the limit of 135° up to 10 GPa for C-H- - -π interactions to be significant. There
are also two interlayer nonbonded distances C1-H1- - -N2 (H1- - -N2 =2.66 Å, C1- - -N2 =
3.54 Å; $\angle$ C1-H1- - -N2 = 138°) and C1-H1- - -N1 (H1- - -N1 = 3.2 Å, C1- - -N1 = 4.18 Å; $\angle$
C1-H1- - -N1= 151°) at ambient conditions. In the case of C1-H1- - -N2 (H1- - -N2 = 2.66
Å, C1- - -N2 = 3.54 Å; $\angle$ C1-H1- - -N2 = 138°) interactions, C1-H1- - -N2 reduces to $\sim$125°,
which becomes highly bent and unfavorable for hydrogen bonding interactions though H1-
- -N2 distance decreases to $\sim$2.3 Å. In the case of C1-H1- - -N1 (H1- - -N1 = 3.2 Å, C1- -
-N1 = 4.18 Å; $\angle$ C1-H1- - -N1 = 151°) interactions, H1- - -N1 distance decreases to $\sim$2.5
Å, and the C1-H1- - -N1 angle increases to $\sim$155° at 10 GPa, which suggests that C1-H1- -
-N1 hydrogen bonding interactions becomes stronger than C1-H1- - -N2 interactions across
this pressure.

In the pressure range 0.5-2.5 GPa, there is drastic reduction in the intensity of the C1-H1
stretching Raman mode which is accompanied by the emergence of new blue-shifted mode
'A' whose relative intensity increases with pressure (see figure 4.5). The calculated value

of C1-H1 bond length shows relatively larger reduction of 0.01 Å compared to 0.006 Å for C2-H2 and 0.0044 Å for C3-H3. As shown in figure 4.11, the crossover of C-H bond lengths takes place at $\sim$ 2.5 GPa, above which the C1-H1 bond length becomes less than C2-H2 and C3-H3. Across the same pressure, crossover of the new mode 'A' with C2-H2/C3-H3 stretching modes suggests that mode A is the blue-shifted C1-H1 mode (3190 cm^{-1}) (see figure 4.5). It is to be noted that the calculated frequencies and the associated C-H vibrations are consistent with the experimental observations (see table 4.2). The observed splitting of the C2-H2/C3-H3 stretching modes in the Raman spectra at pressures above 6.5 GPa is understandable as the differences between the calculated C2-H2 and C3-H3 bond lengths also increase with pressure (see figure 4.11). The large blue-shift of C-H stretching modes (see figure 4.7) and the reduction in the C-H bond lengths along with the reduction in the H- - -N and H- - -C lengths (figure 4.12) suggest that C-H- - -X (X = N, π) hydrogen bonding interactions are 'blue-shifting hydrogen bonds' and are strengthened under pressure.

4.4.5   Polymerization Under Pressure

Though imidazole is rich in unsaturated bonds, no spectroscopic signature of polymerization was observed up to 15 GPa. Above this pressure, emergence of a broad band (shown in black color in figure 4.5) in the C-H stretch spectral region suggests onset of polymeric interaction or supramolecular assembly arising due to pressure-induced strengthening of C-H- - -N interactions. However, absence of any spectral feature of the polymer phase in the retrieved sample suggests that pressure induced polymerization of imidazole is far from complete up to 20 GPa or on release. This high pressure behavior is in contrast to that of its derivative, carnosine, which displays onset of polymerization at pressures as low as 2.8 GPa [250]. Among acetylene and its derivatives, formation of sp^3 species and emergence of polymeric phase is reported for acetylene [307] at pressures $\sim$3 GPa, in comparison to phenyl and diphenylacetylene, which show polymeric interactions at much higher pressures of 8.4 and 9 GPa, respectively [308]. Among the hydrogen bonded molecular solids with unsaturated bonds, the mechanism of pressure induced polymerization is found to be diverse.

In the case of acrylamide [9], polymerization was preceded by a structural transformation to a new phase approximately across 2.6 GPa through reconstruction of hydrogen bonds. However, the percentage of the polymer phase increased only during decompression. On the other hand, for acrylic acid [249], though onset of polymerization was noted at $\sim$8 GPa, the reversibility of the observed spectral changes indicated existence of strong compression-induced association between the monomers and the polymers/oligomers via hydrogen bonds.

4.5   Conclusion

At pressure around $\sim$10 GPa, reduction in the N- - -N distances to the symmetrization limit and the emergence of the new spectral features of the cationic form indicates the onset of proton disorder. Raman spectroscopic study on imidazole suggests that the polymeric interactions in this compound are largely inhibited by the competing N-H- - -N and C-H- - -X (X = N, π) hydrogen bonding interactions in the pressure range of our study.

Chapter 5

Hydrogen Bond Vs Halogen Bond: Iodic Acid

5.1 Introduction

Iodine, a member element of group VII in a periodic table, has large electronegativity which helps it to form stable oxides. Oxoiodate such as $LiIO_3$, $AgIO_3$, KIO_3 and HIO_3 are stable compounds of iodine with oxidation state V [309–312]. These compounds are transparent in spectral region starting from far infrared to visible region hence useful in laser, ferroelectric, piezoelectric and various other technological applications [15, 313–316]. Unit of IO_3^{n-} ions, where the iodine atom has a non-bonded pair of electrons, is building blocks of acentric crystals for second harmonic generation. Similarly, other halate ions (ClO_3^-, BrO_3^-) may also be synthesized for promising oxo-halate materials.

5.2 Motivation

Oxoiodate, crystallizes in diverse crystal structures at ambient conditions because of associated ion's electronegativity with respect to the IO_3^- iodine-oxygen framework. High pressure behavior of metal oxoiodates such as $LiIO_3$, KIO_3 and $AgIO_3$ have already been studied. High pressure studies of these metal oxoiodates showed existence of different crystal phases

under high pressure. High pressure x-ray diffraction studies of $AgIO_3$ showed that a first order phase transition exists at 2.7 GPa [309]. α - $LiIO_3$ is found to be stable upto the highest pressure studied of 75 GPa by Zang $et.$ $al.$ [310] but the different structure β-$LiIO_3$ showed first order phase transition at 5 GPa. Similarly, KIO_3 was studied by Bayarjargal $et.$ $al.$ upto 30 GPa [311] and by Shen $et.$ $al.$ [312] upto 35 GPa, both studies have concluded different results under pressure.

In contrast to other oxoiodates, high pressure studies of iodic acid (HIO_3) are not available in published literature. As hydrogen bond is important at a molecular scale due to its specificity, directionality and ability to accommodate changes with temperature and pressure easily. Iodic acid, which contains hydrogen atom instead of metal atom, with IO_3^- framework, is expected to show different behaviour under pressure.

In this work, iodic acid is investigated under compression and decompression cycle upto 36 GPa using Raman scattering and upto 23 GPa using x-ray diffraction techniques. Raman scattering investigates the nature of bonding at a molecular scale whereas x-ray diffraction probes long range structural order and atomic positions in the cell. Using these two techniques we can investigate the systems for new phase or conformational changes. Experimental results are validated with the help of ab $initio$ theoretical calculation for better understanding of results.

Structural changes with pressure are found to be reversible in nature. Further, we investigated the role of hydrogen bond enhanced 'halogen bond' interaction under pressure.

5.3   Crystal Structure

Iodic acid, a white colored solid crystallizes in orthorhombic crystal structure $P2_12_12_1$, space group 19 and lattice constants **a** = 5.544 Å, **b** = 5.8829 Å, **c** = 7.7434 Å with four formula per unit cell [317], as shown in figure 5.1. Ambient crystal structure of iodic acid is termed as α (alpha) phase in literature. A weak hydrogen bond O-H - - - O (O-H = 0.968 Å, O - - - O = 2.729 Å) join two units together and has a conclusive influence over optical properties [318].
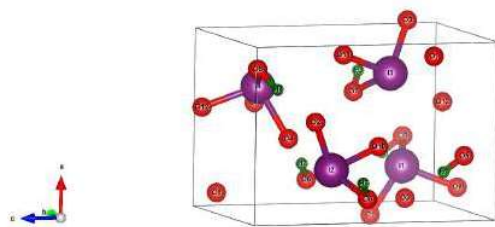
Figure 5.1: Ambient crystal structure of iodic acid

5.4   Experimental Details

Polycrystalline sample of iodic acid was purchased from Sigma-Aldrich Co. Sample was loaded in the hole of diameter $\sim$120 μm of a stainless-steel gasket which was pre-indented to a thickness of $\sim$80 μm in a Mao-Bell type of diamond anvil cell (DAC). Experiments were carried out without pressure transmitting medium to avoid the interaction of medium with the sample. Diode Pumped Solid State (DPSS) laser of 532 nm wavelength was used as Raman exciting source. Pressure was monitored using R-lines of ruby fluorescence and calculated for quasi-hydrostatic conditions. All measurements were recorded in the backscattering geometry using triple stage T64000 spectrograph. High pressure x-ray diffraction studies are carried out at BL-11 beamline at Indus-2 synchrotron upto $\sim$23 GPa. Synchrotron wavelength of 0.50517 Å was used for diffraction experiments to get access of large *k-space*.

5.5   Results and Discussion

Crystal structure of iodic acid has four formula per unit cell which gives 60 vibrational modes. Out of these, 57 are optic modes (36 internal and 21 are external modes) which are found to be Raman and/or IR active. Raman spectrum of iodic acid was recorded in the spectral range of 50-3500 cm^{-1}, excluding 1300-1400 cm^{-1} where vibrational modes of diamond exist as shown in figure 5.2. The relative intensity of O-H stretch modes ($\sim$ 2900 cm^{-1}) is found to be too weak to be followed under pressure. Vibrational mode assignment

is carried out on the basis of earlier published work [313]. Purchased sample was found to be partially dehydrated. Broad bands at $\sim$450 cm^{-1} and $\sim$540 cm^{-1} indicate that iodic acid has been partially dehydrated.

At $\sim$0.5 GPa, Raman spectra shows complete different pattern compared to the ambient pattern shown in figure 5.2. Raman spectra shows discontinuities in Raman frequencies at $\sim$0.5 GPa as shown in figure 5.3. At this pressure, IO$_3$ symmetric (733 cm^{-1} and 774 cm^{-1}) antisymmetric (812 cm^{-1}) show softening with discontinuous changes in slope with pressure. On comparison, Raman pattern at $\sim$0.5 GPa shows close resemblance with the ambient Raman spectra of I$_2$O$_5$ within I-O stretch modes range [319]. Ambient Raman spectra of I$_2$O$_5$ includes dominating I-O-I bond at $\sim$810 cm^{-1}. Similarly, Raman pattern of iodic acid at $\sim$0.5 GPa also show the dominating peak at $\sim$775 cm^{-1}. As IO$_3$ units modes are less affected by the crystal environment compared to the lattice modes, the nature of IO$_3$ modes can be used for determination of molecular conformation and bonding nature. Internal environment for iodic acid may be similar to I$_2$O$_5$ for I-O stretch bonds and this environment may have been generated through dehydration or conformational changes [319].

High pressure x-ray diffraction investigation were carried out up to $\sim$23 GPa (figure 5.5. Ambient x-ray diffraction pattern is found to be in good agreement with reported orthorhombic crystal structure of iodic acid [317] as shown in figure 5.4). However, x-ray diffraction pattern shows no changes in the pattern or intensity till the highest pressure 23.7 GPa. Behaviour in x-ray diffraction is a indication that phase transition may be related to the conformational changes of IO$_3$ molecular unit rather than drastic change in the lattice structure as it is very common for hydrogen bonded solids to have conformational changes under pressure. This result is in contrast to other metal oxoiodates where first order phase transition with pressure was observed with definite change in the x-ray diffraction pattern.
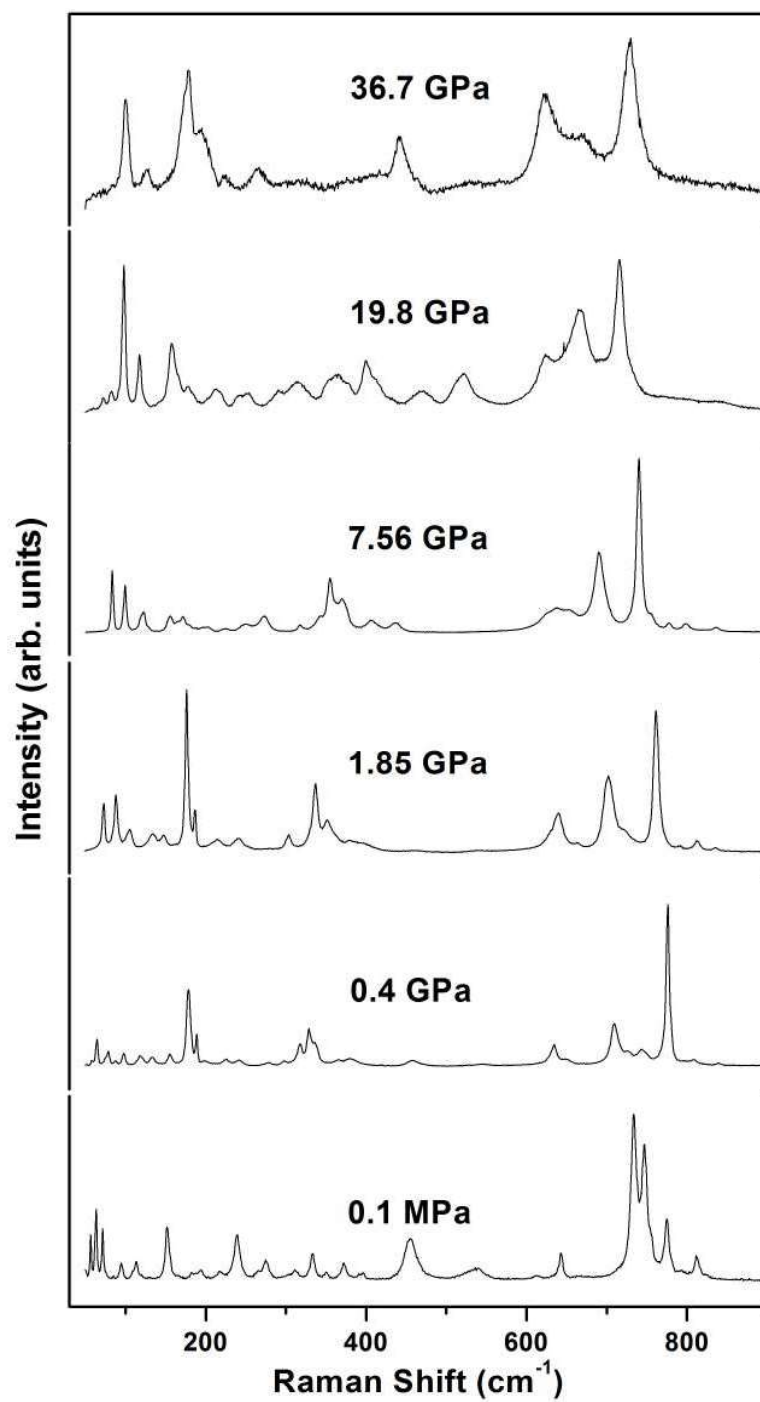
Figure 5.2: Raman spectra with pressure
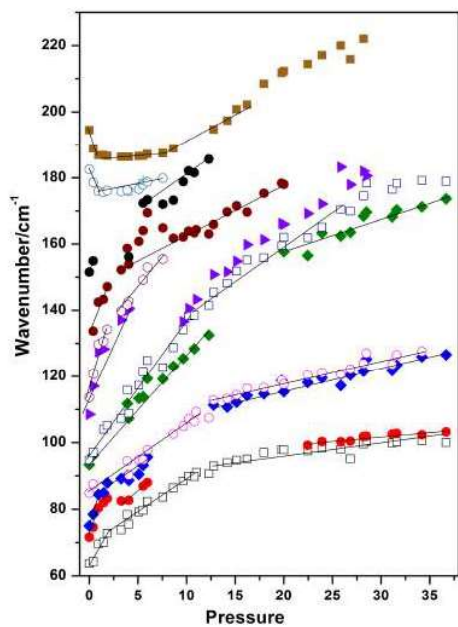
(a)
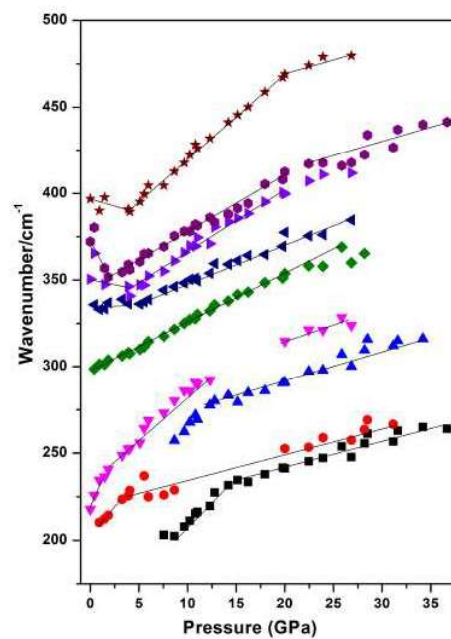
(b)
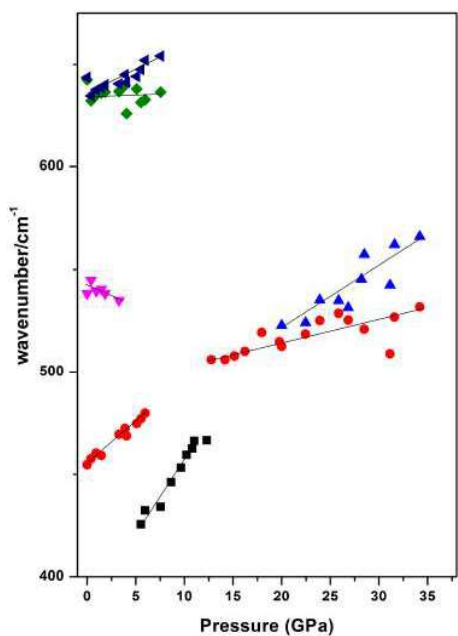
(c)
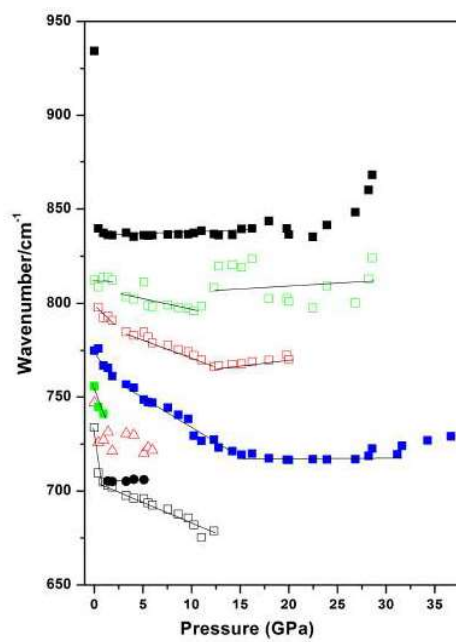
(d)

Figure 5.3: Raman spectra in the spectral range (a) 0-200 cm^{-1}; (b) 200-400 cm^{-1}; (c) 400-600 cm^{-1}; (d) 600-800 cm^{-1};

(a)   (b)
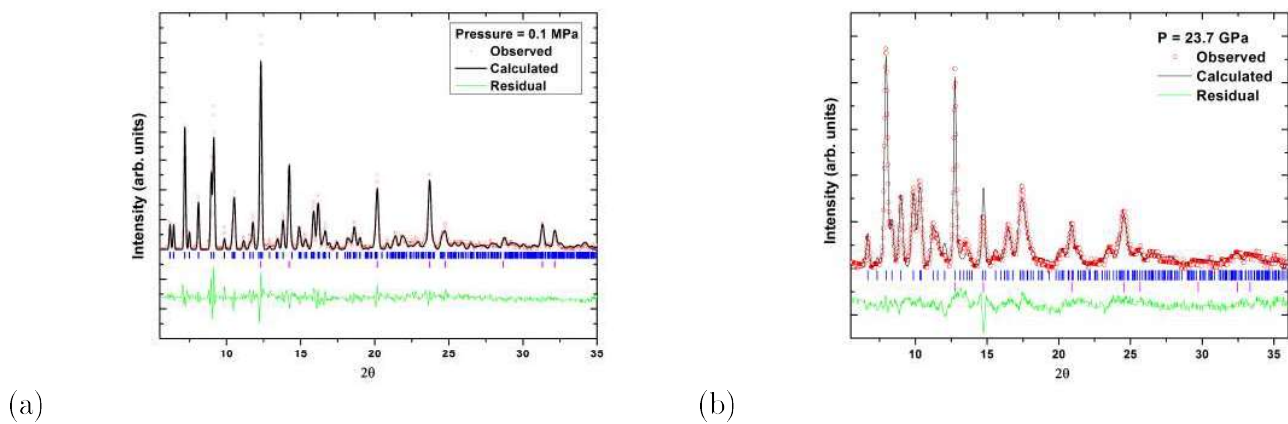
Figure 5.4: XRD pattern (a) at 0.1 MPa; (b) at 23.7 GPa;
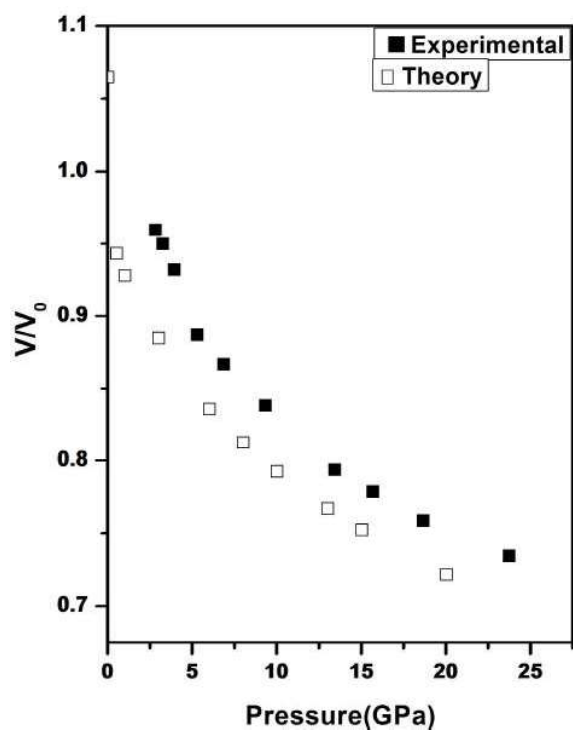
Figure 5.5: Experimental and theoretical data for volume and pressure

(a)

(b)
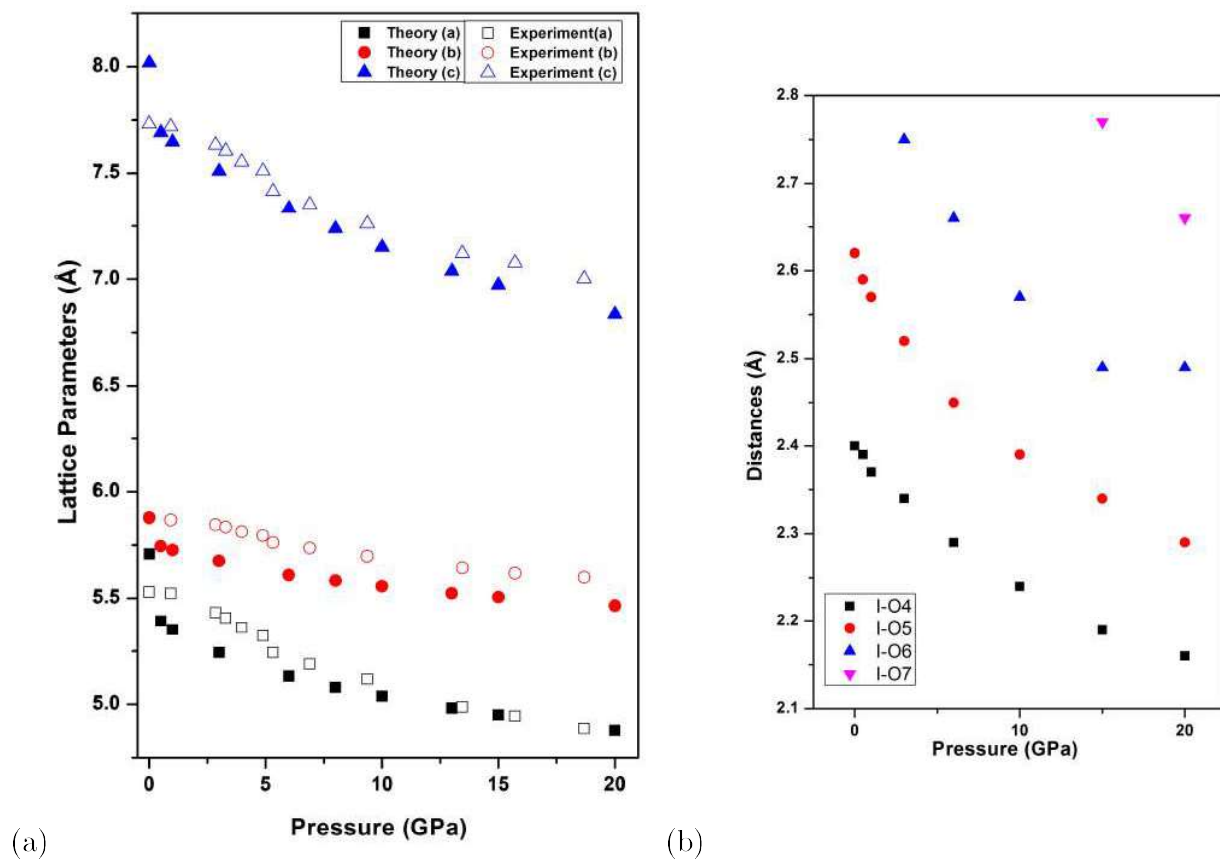
Figure 5.6: (a) Experimental and Theoretical comparison of lattice constants; (b) Interatomic distance of atoms; with pressure
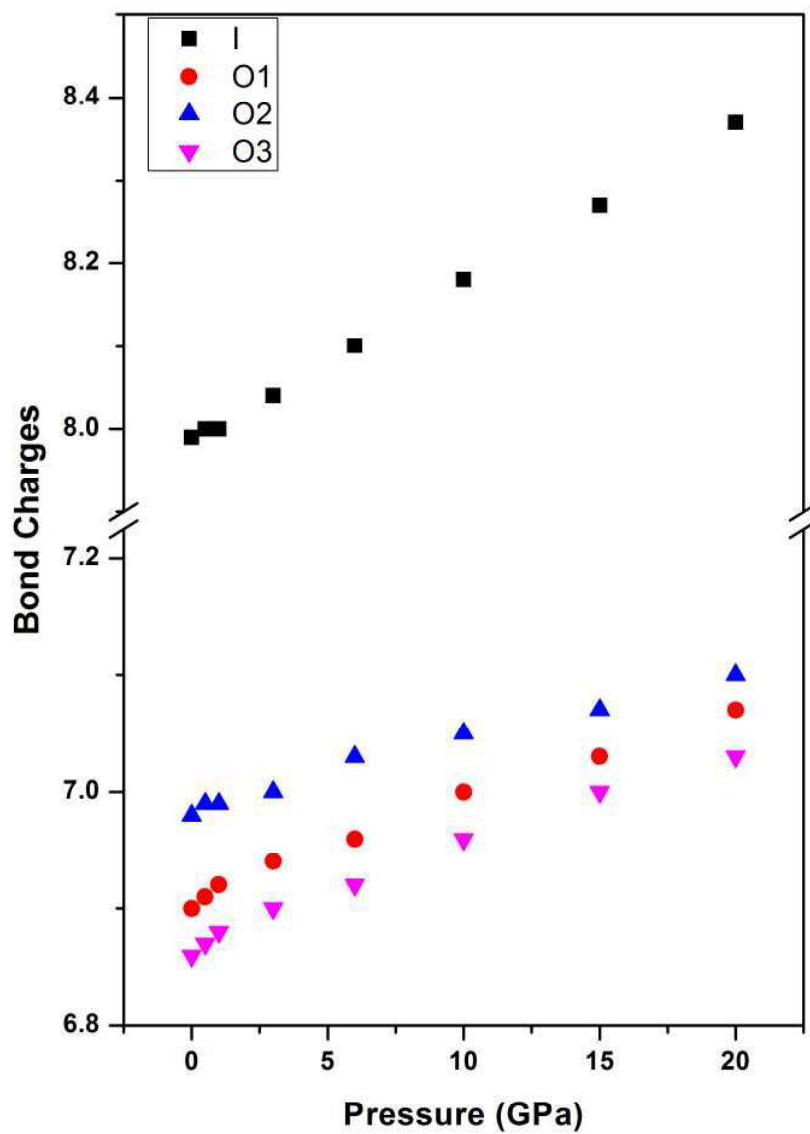
Figure 5.7: Bond charges on atoms

5.6   The Halogen Bond

Halogen bond R-X- - -Y (where X=F, Cl, Br, I and Y= N, O) is an interactions where X - - - Y bond gains in strength due to n $\rightarrow \sigma^*$ charge transfer. As result R-X force constant decreases while effective charge on the R atom increases which lead to a red-shifted with higher intensity of R-X modes [320]. Initially, HIO_3 has tetrahedral IO_3^- formation with bond lengths (I-O1 =1.7974 Å, I-O2 = 1.8978 Åand I-O3 = 1.7851 Å) and other nearest neighbor oxygen atoms are 2.7699 Å and 2.5094 Å distance away from the iodine atom as shown in figure 5.6. As pressure is raised, inter atomic distance reduces and at ∼0.5 GPa new oxygen atoms come close (within ∼2.4 Å) to iodine which is less then combined Van der Waal distance of iodine and Oxygen (3.51 Å). At ∼0.5 GPa theoretical results also confirms sudden change in bond charges (figure 5.7) because of possible charge transfer. As inter-atomic distance is favorable for making 'halogen bond', there is possibility of increasing effective co-ordination number from V to VI and VII of iodine within existing framework. Initially, iodine atom which is in the oxidation state V but due to the change in inter-distance between atoms (I and O) the possibility of interaction is open and electronic charge is distributed in such a way that force constant between existing I-O bonds is modified. Softening of various modes in I-O stretch region is observed under pressure. This softening in I-O stretch region is reported in all oxoiodates. Iodine has the greatest tendency to form 'halogen bond' however there is possibility that higher coordination compounds may have been formed for other oxoiodates under pressure. Raman spectra also shows discontinuous changes at ∼5 and ∼10 GPa. After ∼20 GPa I-O stretch mode shows stiffening under pressure. However, the x-ray diffraction does not show any change in pattern up to the highest pressure of ∼23 GPa. These observations indicate that these conformational changes also are not accompanied by any drastic structure changes

For I_2O_5, distance between I-O bond and the non-bonded I- - -O distance has been found to be critical for transition from 2D to 3D structure and phase transitions were driven by the increase of average coordination number of iodine from III in phase-I to IV in phase-II, and a mixed (IV and VI) in phase-III [319]. It is also reported that in the high pressure

phases, non bonded interaction distance between iodine and oxygen is approximately 2.5 Å - 2.8 Å that play an important role to form pseudo polymeric phase. I_2O_5 showed the polymerization above $\sim$23 GPa. In contrast to I_2O_5, iodic acid does not show any sign of polymerization till $\sim$36 GPa. This may be because of the presence of competing halogen and hydrogen bond.

All changes with pressure are found to be completely reversible. As changing co-ordination number result in altering electronic, optical properties of materials, this high pressure study may be helpful for designing the model iodine based nonlinear materials or high pressure sensor.

5.7 Conclusion

High pressure study has given evidences of presence of iodine based coordination compounds. These compounds of iodine display novel nonlinear effects that are useful for technological applications such as laser *etc.*. At $\sim$0.5 GPa due to conformational change, a new type of bond called 'halogen bond' come into existence. Though high pressure x-ray diffraction does not show any drastic change in pattern, formation of halogen bond is indicated by Raman scattering and *ab-initio* studies. Halogen and hydrogen bond play an important role to provide structural stability under pressure.

Chapter 6

High Pressure Studies of Niobium Oxynitrides

6.1 Introduction

Niobium nitrides have attracted considerable attention because of their interesting superconductive properties. Niobium oxynitride compound can be viewed as arising from NbN through substitution of N^{3-} by O^{2-} leading to the creation of cationic vacancies [321]. The doping changes the band gap of niobium oxides precursor and shifts its valence band edge bringing the changes in its various properties. As a result, superconducting niobium oxynitrides ($NbN_{0.98}O_{0.02}$, T_c=17.6K) has important applications as catalysis, dielectrics and glasses *etc.*. Further, doping by Al gives ($Nb_{0.89}Al_{0.11}N_{0.86}O_{0.14}$), Si gives ($Nb_{0.87}Si_{0.09}N_{0.87}O_{0.13}$) and Mg gives ($Nb_{0.95}Mg_{0.05}N_{0.92}O_{0.08}$). Doped niobium oxynitride also has cubic face centred structure derived from parent compound NbON. Since all doping elements has different atomic radii, hence doping is bound to affect the lattice constants or unit cell dimensions and ultimately physical properties of materials. High pressure is an important tool to investigate structural stability and also frequently used to search new structural phases. We have studied the high pressure behavior of these materials using angle dispersive synchrotron based x-ray diffraction.

6.2 Sample Preparation and Crystal Structure

Preparations of oxynitrides were done by ammonolysis of oxide precursor obtain through citrate route [322, 323]. Crystal structure of $NbN_{0.98}O_{0.02}$ and other doped oxynitrides is cubic face centered with space group 225 (F m3m). At ambient condition, lattice parameter determined for $NbN_{0.98}O_{0.02}$ using Rietveld refinement is ~ 4.43 Å which is consistent with earlier studies [324]. Observed changes in the lattice parameter for Nb(N,O) with Mg, Al and Si dopants are listed in table 6.1.

6.3 Experimental Details

High pressure XRD experiments were carried out at XRD1 beamline of Elettra synchrotron source using 0.6888 Å monochromatic x-rays. Sample along with the gold powder was loaded in $\sim 80\mu m$ diameter hole drilled in a pre-indented tungsten gasket. The pressure was raised in very fine steps using an indigenously developed membrane driven diamond anvil cell. Experiments were carried out without any pressure transmitting medium. The pressure inside the sample chamber was determined from the known equation of state of Gold.

6.4 Result and Discussion

Figure 6.1 shows angle dispersive x-ray diffraction patterns of $NbN_{0.98}O_{0.02}$ with pressure at a few representative pressures (total 170 diffraction patterns were recorded). Analysis of the diffraction patterns show that it remains in ambient cubic phase upto ~ 18 GPa pressure. On further application of pressure the diffraction patterns show sudden broadening of diffraction peaks. Cubic $NbN_{0.98}O_{0.02}$ diffraction peak (111) started broadening with pressure and at ~ 18 GPa three peaks were observed which could be identified as rhombhohedral (111) and (100) coexisting with the cubic phase. Similarly other cubic diffraction peaks (200), (220) etc. showed broadening with pressure. These observations suggest that the cubic structure is undergoing rhombohedral distortion, as the basic primitive rhombohedral unit of the
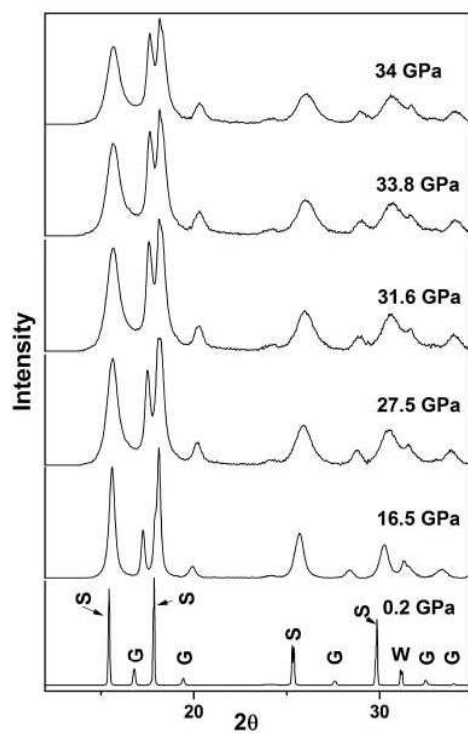
Figure 6.1: Angle dispersive x-ray diffraction patterns of $NbN_{0.98}O_{0.02}$ at a few pressures (total 170 diffraction patterns were recorded); S, G and W denote the diffraction peak from the sample, gold and tungsten gasket respectively
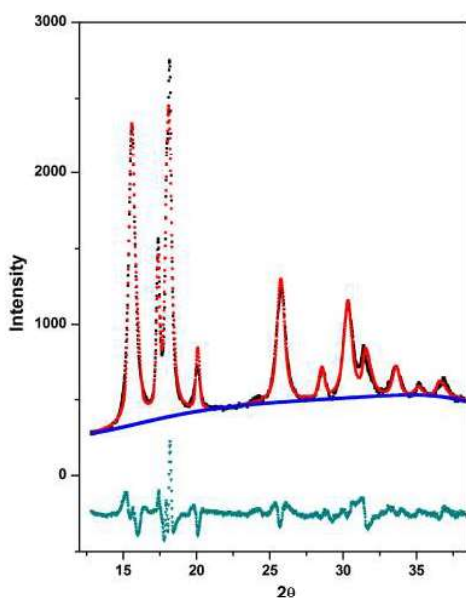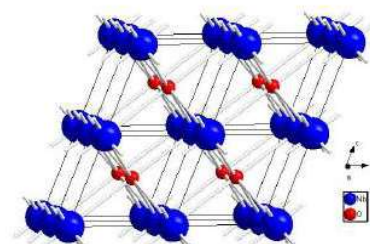
(a)   (b)

Figure 6.2: (a) Rietveld Refinement of Niobium Oxynitride ($NbN_{0.98}O_{0.02}$) in the high pressure rhombohedral structure at $\sim$34 GPa. measured data are represented by cross symbol, red line represent the calculated pattern, green line is the background and blue line represent the difference in calculated and measured patterns.; (b)Crystal structure of Rhombhohedral cell;

cubic structure having 60° angle shows a slight distortion. The Rietveld refinement of the patterns above transition pressure show that the angle changes to $\sim$59° (figure 6.2). This distortion in the primitive cell can be associated with the transition of cubic structure to the rhombohedral structure (R3m, 166). Rietveld refinement for rhombohedral phase at $\sim$34 GPa is given in Figure 6.2. Weighted R factor (wRp) for the rhombohedral phase refinement was found to be 0.0457. At transition pressure, volume dropped by 0.37 % per formula unit of $NbN_{0.98}O_{0.02}$ suggesting the transition to be of first order in nature.

(a)

(b)

(c)

(d)
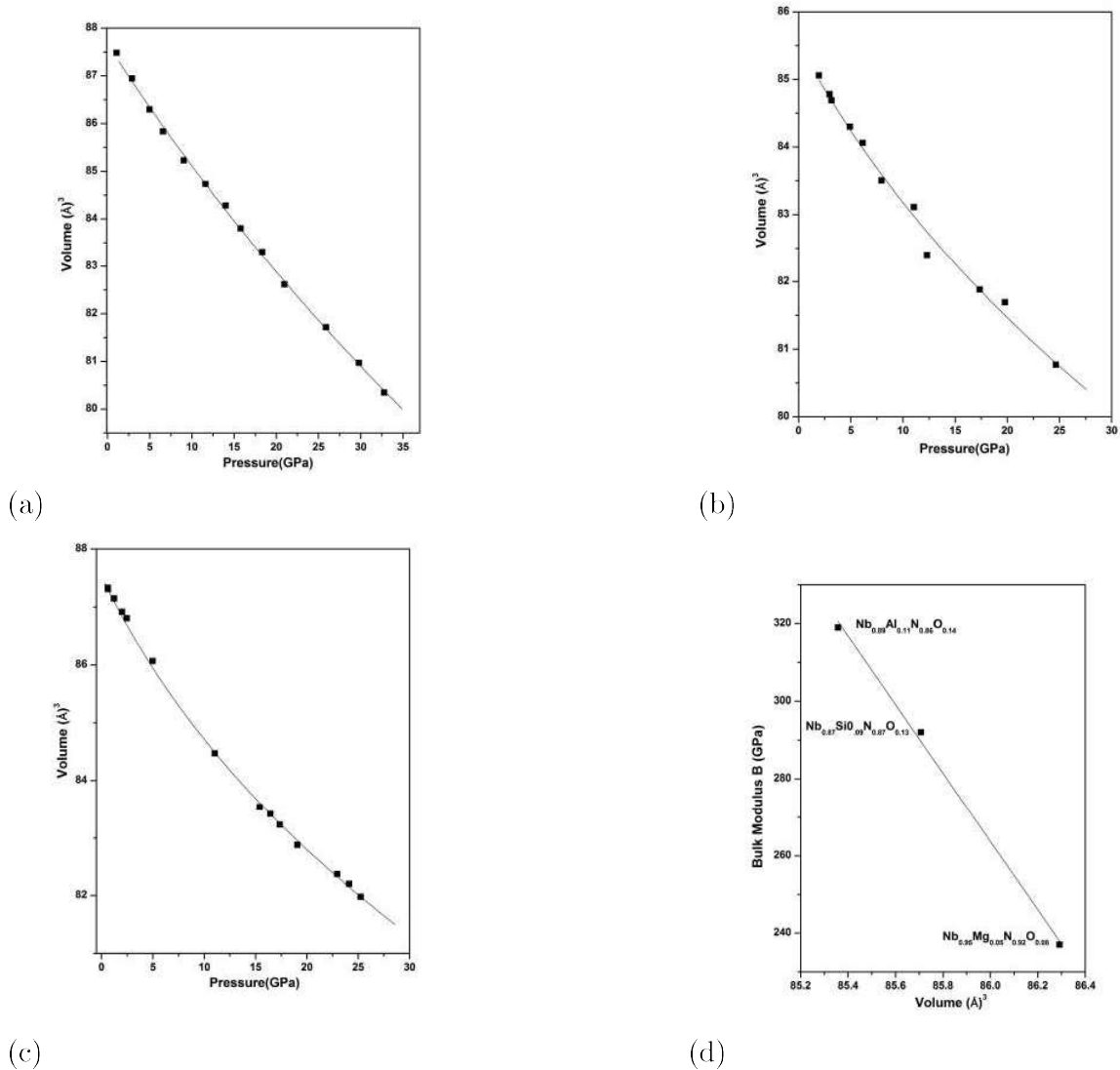
Figure 6.3:   (a) $Nb_{0.89}Al_{0.11}N_{0.86}O_{0.14}$ P-V curve; (b)$Nb_{0.87}Si_{0.09}N_{0.87}O_{0.13}$ P-V curve; (c)$Nb_{0.95}Mg_{0.05}N_{0.92}O_{0.08}$ P-V curve; (d) Variation of Bulk Modulus with volume;

Oxynitride	Lattice Constant(Å)	Bulk Modulus(B)	Derivative (B')	Bulk Modulus B (when B'=4)
$Nb_{0.95}Mg_{0.05}N_{0.92}O_{0.08}$	4.419 [322]	237.9	16.66	323.3
$Nb_{0.89}Al_{0.11}N_{0.86}O_{0.14}$	4.403 [323]	319.9	3.88	318.5
$Nb_{0.87}Si_{0.09}N_{0.87}O_{0.13}$	4.409 [322]	292.8	14.85	363.7

Table 6.1: B and B' of Mg, Al and Si doped Niobium oxynitrides

All other three oxynitrides viz. $Nb_{0.95}Mg_{0.05}N_{0.92}O_{0.08}$, $Nb_{0.89}Al_{0.11}N_{0.86}O_{0.14}$ and $Nb_{0.87}Si_{0.09}N_{0.87}O_{0.13}$ were pressurized up to $\sim$25 GPa, $\sim$32 GPa, $\sim$24 GPa respectively. The recorded diffraction patterns do not show any structural transition up to the highest pressures studied. Lattice parameters as function of pressure have been determined by Rietveld refinement. Measured P-V behavior is shown in figure 6.3 (a,b,c). Bulk modulii (B) and their pressure derivative (B') were determined by least square fitting to third order Brich-Murunaghan equation of state. Respective B and B' are listed in table 6.1 and also plotted in figure 6.3(d). As mentioned above, these oxynitrides are formed by replacing the oxygen atoms with the nitrogen and doping with Mg^{+2}, Al^{+3} and Si^{+4}. Ionic radii of Nb (0.70) and Mg (0.72) are comparable to each other while the ionic radii of Al (0.535 Å) and Si (0.40 Å) significantly differ from those of Nb and Mg. Understandably the lattice constant of $Nb_{0.95}Mg_{0.05}N_{0.92}O_{0.08}$ is the largest. Similar ratios of Nb/Al and Nb/Si concentrations along with comparability of ionic radii of Al and Si imply their similar lattice constants as shown in the figure 6.3 (d). Observed small difference in the lattice constants of $Nb_{0.87}Si_{0.09}N_{0.87}O_{0.13}$ and $Nb_{0.89}Al_{0.11}N_{0.86}O_{0.14}$ could be because of Nb vacancies in former.

6.5   Conclusion

High pressure investigations on niobium oxynitrides with doped samples (Mg, Al and Si) had shown that these compounds were stable up to the highest pressures studied ($\sim$ 30 GPa). Which is in contrast to $NbN_{0.98}O_{0.02}$ which showed phase transition under pressure. Ambient cell volume and bulk modulus of the doped oxynitrides were found to be dependent upon the atomic radius of the dopant elements. All high pressure changes were found completely

reversible under pressure.

Appendices

Appendix A1

The Radiation Emitted By An Oscillating Dipole

Maxwell's equation

$$divD = 4\pi\rho$$

$$curlH = \frac{4\pi}{c}J + \frac{1}{c}\frac{\partial D}{\partial t}$$

$$divB = 0$$

$$curlE + \frac{1}{c}\frac{\partial B}{\partial t} = 0$$

With the constitutive equations $D = \epsilon E$, $J = \sigma E$ and $B = \mu H$.

Because, $divB = 0$ and $divcurlV = 0$ for any vector, we define a vector $\mathbf{A}$, the vector potential as following:

$$B = curlA$$

With this the Maxwell's equation for curl E reads

$$curl\left(E + \frac{1}{c}\frac{\partial A}{\partial t}\right) = 0$$

Since curl grad$\xi = 0$, for any function ξ so parentheses of above equation can be written as

the gradient of some scalar function ϕ.

$$E + \frac{1}{c}\frac{\partial A}{\partial t} = -grad\phi$$

In terms of A and ϕ, the two inhomogeneous maxwell equation becomes

$$\nabla^2\phi + \frac{1}{c}\frac{\partial A}{\partial t} = -4\pi\rho$$

$$\nabla^2 A - \frac{1}{c^2}\frac{\partial^2 A}{\partial t^2} - \nabla\left(\nabla.A + \frac{1}{c}\frac{\partial\phi}{\partial t}\right) = -\frac{4\pi}{c}J$$

We can replace A and ϕ by gauge's transformation, $A \to A + \nabla\xi$ and $\phi \to \phi - \frac{1}{c}\frac{\partial\xi}{\partial t}$. These transformation will decouple the Maxwell equation's

$$\nabla^2\phi + \frac{1}{c^2}\frac{\partial^2 A}{\partial t^2} = -4\pi\rho$$

$$\nabla^2 A - \frac{1}{c^2}\frac{\partial^2 A}{\partial t^2} = -\frac{4\pi}{c}J$$

Above equations are inhomogeneous wave equation of the form

$$\nabla^2\psi + \frac{1}{c^2}\frac{\partial^2\psi}{\partial t^2} = -4\pi f(r,t)$$

where $f(r,t)$ is source function. Solution for such equation can be obtained by the Green's method

$$\Psi = \int \frac{\delta\left(t' + \frac{|r-r'|}{t} - t\right)}{|r-r'|}f(r',t')dr'dt'$$

Green's function is defined as

$$G(r,t;r',t') = \frac{\delta\left(t' + \frac{|r-r'|}{t} - t\right)}{|r-r'|}f(r',t')$$

For wave vector A,

$$A = \frac{1}{c} \int dr' \int dt' \frac{J(r',t')}{|r-r'|} \delta\left(t' + \frac{|r-r'|}{t} - t\right)$$

Assume $J(r,t) == J(r)exp(-i\omega t)$ and $A(r,t) = A(r)exp(-i\omega t)$ with

$$A(r) = \frac{1}{c} \int J(r')dr'$$

With $k = \frac{\omega}{c}$ and $|r - r'| \sim r$, equation becomes

$$A(r) = \frac{exp(ikr)}{cr} \int J(r')dr'$$

If $\rho(r,t) = \rho(r)\exp(-i\omega t)$ and $\int J dr' = - \int r'[\bigtriangledown.J(r')]$, with the help of continuity equation **A** is defined as following

$$A(r) = ikp\frac{\exp(ikr)}{r}$$

where p is electric dipole moment. Since $B = curl A$ and $E = \frac{i}{k} curl B$, these equation yield

$$B = k^2(\epsilon \times p)\frac{exp(ikr)}{r}$$

$$E = B \times \epsilon$$

For the radiation emitted per unit solid angle in the direction X, $\epsilon = \epsilon_x$ and $p = (\epsilon_x p_{ox} + \epsilon_y p_{oy} + \epsilon_z p_{oz}) \cos(\omega t)$

$$B = k^2(\epsilon_z p_{oy} - \epsilon_y p_{oz}) \cos \omega t \frac{exp(ikr)}{r}$$

$$E = k^2(\epsilon_y p_{oy} + \epsilon_z p_{oz}) \cos \omega t \frac{exp(ikr)}{r}$$

and the Poynting vector $S = E \times B$ gives

$$S = \epsilon_x k^4(p_{oy}^2 + p_{oz}^2) \cos^2 \omega t$$

As $k = \frac{\omega}{c}$, scattering intensity (I) for the oscillating dipole can be written as

$$I = \frac{16\pi^4 \nu^4}{3c^3} p_0^2$$

and the rate of radiation per unit solid angle in the X-direction is

$$\left(\frac{dI}{d\Omega} \right) = \frac{2\pi^3 \nu^4}{c^3} (p_{oy}^2 + p_{oz}^2)$$

Here polarizibility α is related to the dipole moment by the relation $p = \alpha E$. As it is clear that intensity of the emitted radiation varies as the fourth power of incident radiation frequency.

Appendix A2

A New Raman System Installed in the Purnima Laboratory

A new confocal Raman setup for high pressure experiments is installed in the laboratory. Image of installed spectrograph is shown in the figure A2.1. The basic design of optical setup for new system remains similar as described in the chapter 1. Few important instrument parameters and recorded spectra for iodic acid are shown in the table A2.1 and figure A2.2 respectively.

Spectrograph name	Andor
Grating (lines/mm)	1200, 1800, 2400
CCD	13.5μx13.5μ, 2048x512 pixel, Peltier Cooled, Newton
Dark Current	< 0.72 e^{-1}/pixel/hour
Focal Length	500 cm
Resolution	< 0.07 nm with 1200 grating
Stray Light Rejection	1.1E-4
f-number	$f/6.5$

Table A2.1: Important parameters for the new Raman set up installed in the laboratory

Figure A2.1: New Raman Setup installed in the laboratory
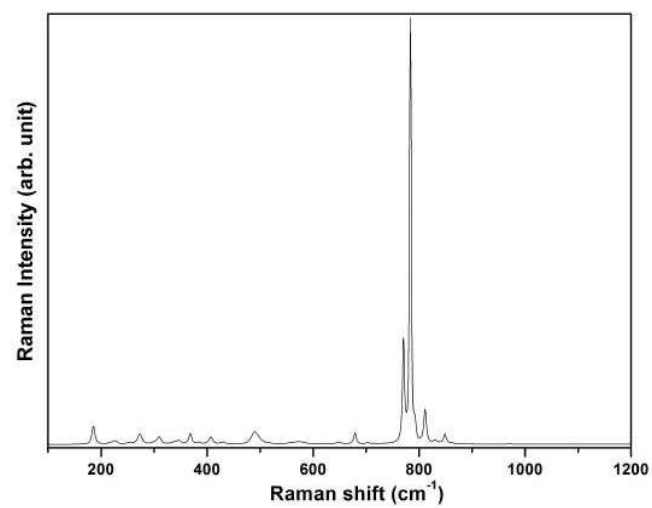
Figure A2.2: Raman spectra of Iodic acid collected in laboratory with Andor spectrograph

Appendix A3

Structural Determination Using Powder X-Ray Diffraction

The basic introduction of structural determination using x-ray diffraction method is given in the chapter 2. powder diffraction pattern contain diffraction rings that contain structural informations in Fourier space. The background of diffraction gives the information about the local structure, amorphous nature of the material. Diffraction peaks are characterized by the three parameters which are peak position, intensity and profile. All these parameters include the information of unit cell, arrangements of atoms within unit cell. Peak profile includes the instrument broadening.

The unit cell geometry determine the positions of diffraction peak. Each of the seven crystal system, diffraction peaks positions has its unique pattern. Position of atoms in the unit cell is determined by the relative intensity of the diffraction peaks. Also the number of atoms per unit cell, density and chemical formula unit are calculated with the help of diffraction pattern. Assigning the peak position to diffraction pattern corresponding to the seven crystal system is called indexing.

Crystal System	Lattice Parameters	Relation
Triclinic	$a \neq b \neq c$ and $\alpha \neq \beta \neq \gamma$	-
Monoclinic	$a \neq b \neq c$ and $\alpha \neq \beta = \gamma = 90$	$\frac{1}{d^2} = \frac{1}{\sin^2 \beta}\left(\frac{h^2}{a^2} + \frac{k^2 \sin^2 \beta}{b^2} + \frac{l^2}{c^2} - \frac{2hl\cos\beta}{ac} \right)$
Orthorhombic	$a \neq b \neq c$ and $\alpha = \beta = \gamma = 90$	$\frac{1}{d^2} = \frac{h^2}{a^2} + \frac{k^2}{b^2} + \frac{l^2}{c^2}$
Tetragonal	$a = b \neq c$ and $\alpha = \beta = \gamma = 90$	$\frac{1}{d^2} = \frac{h^2+k^2}{a^2} + \frac{l^2}{c^2}$
Cubic	$a = b = c$ and $\alpha = \beta = \gamma = 90$	$\frac{1}{d^2} = \frac{h^2+k^2+l^2}{a^2}$
Trigonal	$a = b = c$ and $\alpha = \beta = \gamma \neq 90$	$\frac{1}{d^2} = \frac{(h^2+k^2+l^2)+\sin^2\alpha+2(hk+kl+hl)\cos^2\alpha-\cos\alpha}{a^2(1-3\cos^2\alpha+2\cos^3\alpha)}$
Hexagonal	$a = b \neq c$ and $\alpha = \beta = 90 \neq \gamma = 120$	$\frac{1}{d^2} = \frac{4}{3}\left(\frac{h^2+hk+k^2}{a^2} \right) + \frac{l^2}{c^2}$

Table A3.1: Lattice parameters for seven crystal systems

A3.1   Indexing

Indexing the crystal system involve assigning (hkl) and space group to the structure. X-Ray diffraction is obtained by the constructive and destructive interference pattern from atomic planes of unit cells, identified by the Milller indices (hkl). In the two dimensional pattern, diffraction rings are obtained at angle 2θ (satisfy the Bragg's law condition $2d\sin\theta = n\lambda$) from center, are related to the Miller indices (hkl), which in turn related to inter planner spacing (d_{hkl}) and lattice constants $(a, b, c, \alpha, \beta, \gamma)$ as shown in the table A3.1.

A3.2   Rietveld Refinement

Ideally, x-ray diffraction peak should have a delta function profile. However, in reality these peaks are broadened and have certain profile due to finite crystal size, imperfections, thermal motion, stress, orientation and instrument broadening. In order to determine the correct structure we have to deconvolute these effects.

Intensity of diffracted pattern depends upon structural factor S_{hkl} which in turn relates

to the atomic position as following

$$I = |S_{hkl}|^2 = \sum_{j=1}^{N} f_j \exp^{-2\pi i (hx_i + ky_j + lz_k)}$$

Rietveld refinement is the process of minimizing the difference between observed pattern and model system. The residue (S) between observed and model is minimized by the least square method.

$$S = \Sigma w (I_o - I_c)^2$$

Here, I_o and I_c are observed and calculated intensity respectively while w is weight factor. Many mathematical program such as GSAS are available to solve the minimizing problem. According to this program, calculated intensity of the diffraction peak is given by

$$I_c = I_b + I_d + S_h \Sigma S_{ph} Y_{ph}$$

Here I_b represents the contribution from background, I_d is background due to diffused scattering. S_h and S_{ph} are scaling factor for particular x-ray and phase profile respectively. Y_{ph} is the intensity of the Bragg's peak, related to the square of structural factor.

$$Y_{ph} = |S_{ph}|^2 H(T - T_{ph}) K_{ph}$$

Here $S_{ph} = S_{hkl}$, and $H(T - T_{ph})$ is a profile function. K_{ph} is a correction and geometry factor which includes absorption, orientation, reflection multiplicity, Lorentz polarization factor *etc.*. In order to determine the crystal structure, first Le Bail method is used. This is done by the setting all calculated structure factor $S_c = 1$ and running the least square algorithm iteratively to obtain observed observed structure factor until the good fit is obtained. Here lattice and profile shape is refined in each step. Detailed atomic pattern is not taken into consideration but only the space group and lattice constants are used. The structural factor obtained in this method is used as the input for the Rietveld refinement.

In GSAS program there are several peak profiles listed. But for the high pressure exper-

iments pseudo-voiget profile is often used. It is the combination of Lorentzian and Gaussian functions, having many parameters to refine the Full Width at Half Maxima (FWHM).

To start with the refinement, first background of the observed pattern to fitted. For this purpose various polynomials of different degree are available in GSAS and can be used accordingly. With this least square method is used iteratively where atomic position, thermal, lattice parameters and profile functions are refined.

Quality of fit is decided by many indicators, out of which visual inspection is also included. R and R_{wp} factors defined by the calculated and observed intensity are an important mathematical indicators. These are defined as following

$$R_p = \frac{\Sigma|I_o - I_c|}{\Sigma I_o}$$

$$R_{wp} = \sqrt{\frac{S}{\Sigma w I_o^2}}$$

In addition to these goodness of fit χ^2 is used. χ^2 is defined by $\chi^2 = \frac{R_{wp}}{R_{exp}}$. where,

$$R_{exp} = \sqrt{\frac{n - p}{\Sigma w I_o^2}}$$

For good fit χ^2 should close be to unity.

Bibliography

[1] F. A. de G. Tom and E. W. Meijer. Material science: Supramolecular polymer. *Nat.*, pages 171–173, 2008.

[2] X. Yan, S. Li, J. B. Pollock, T. R. Cook, J. Chen, Y. Zhang, X. Ji, Yihua Yu, and P. J. Stang. Supramolecular polymers with tunable topologies via hierarchical coordination-driven self-assembly and hydrogen bonding interfaces. *Proc. Natl. Acad. Sci. USA*, 110 (39):15585–15590, 2013.

[3] D. E. Moilanen, I. R. Piletic, and M. D. Fayer. Water dynamics in nafion fuel cell membranes: The effects of confinement and structural changes on the hydrogen bond network. *J. Phys. Chem. C*, 111:8884–8891, 2007.

[4] G. D. Rose and R. Wolfenden. Hydrogen bonding, hydrophobicity, packing, and protein folding. *Annu. Rev. Biophys. Biomol. Struct.*, 22:381–415, 1993.

[5] F. C. Hawthorne and W. H. Baur. *Hydrogen Bonding in Minerals, Volume 1*. Springer Berlin Heidelberg, first edition, 1994.

[6] S. K. Sikka and S. M. Sharma. Pressure induced amorphisation of materials. *Curr. Sci.*, 63:317, 1996.

[7] S. K. Sikka. The hydrogen bond under pressure. *Phase Transt.*, 81(10):907–934, 2008.

[8] T. V. Neal, K. R. O.and Brinzari, J. B Wright, C. Ma, S. Giri, J. A. Schlueter, Q. Wang, P. Jena, Z. Liu, and J. L. Musfeldt. Pressure-induced magnetic crossover driven by hydrogen bonding in $cuf_2(h_2o)_2$(3-chloropyridine). *Sci. Rep.*, 4:6054, 2014.

[9] B. B. Sharma, C. Murli, R. Chitra, and S. M. Sharma. Hydrogen-bonding interactions in fully deuterated α-glycine at high pessures. *J. Raman Spect.*, 43:138–145, 2012.

[10] B. B. Sharma, C. Murli, and S. M. Sharma. Hydrogen bonds and polymerization in acrylamide under pressure. *J. Raman Spect.*, 44:785–790, 2013.

[11] J. T. Daycock, G. P. Jones, J. R. N. Evans, and J. M. Thomas. Rotation of imidazole in the solid state and its significance in deciding the nature of charge migration in biological material. *Nat.*, 218:672–673, 1968.

[12] S. Aftergut and G. P. Brown. Electronic properties of imidazole. *Nat.*, 191:379–380, 1961.

[13] B. M. Carven, R. K. McMullan, J. D. Bell, and H. C. Freeman. The crystal structure of imidazole by neutron diffraction at 20ºc and -150ºc. *Acta Crystallogr. Sect. B*, B33:2585–2589, 1977.

[14] B. B. Sharma, A. K. Verma, S. Thomos, C. Murli, and S. M. Sharma. Hydrogen bonds and ionic forms versus polymerization of imidazole at high pressures. *J. Phys. Chem. B*, 119:372–378, 2015.

[15] S. K. Kurtz and T. T. Perry. A powder technique for the evaluation of nonlinear optical materials. *J. Appl. Phys.*, 39(8):3798–3813, 1968.

[16] K. Nassau, J. W. Shiever, and B.E. Prescott. Transition metal iodates. i. preparation and characterization of the 3d iodates. *J. Solid State Chem.*, 7:186 âĂŞ 204, 1973.

[17] R. Liminga, S. C. Abrahams, and J. L. Bernstein. Pyroelectric $nd(io_3)_3.h_2o$. crystal structure of the transition-metal iodates. ii. *J. Chem. Phys.*, 62:755–763, 1975.

[18] S.C. Abrahams, J.L. Bernstein, and K. Nassau. Transition metal iodates. vii. crystallographic and nonlinear optic survey of the 4f-iodates. *J. Solid State Chem.*, 16:173–184, 1976.

[19] B. B. Sharma, P.S. Ghosh, H. K. Poswal, and C. Murli. High pressure raman and xrd investigation of iodic acid (hio$_3$), (to be submitted).

[20] A. Jayaraman. Diamond anvil cell and high-pressure physical investigations. *Rev. Mod. Phys.*, 55(1):65–108, 1983.

[21] D. Paliwoda, K. F. Dziubek, and A. Katrusiak. Imidazole hidden polar phase. *Cryst. Growth Des.*, 12:4302–4305, 2012.

[22] G. A. Jeffery. *An Introduction to Hydrogen Bonding*. Oxford University Press, New York, 1997.

[23] W. M. Latimer and W. H. Rodebush. Polarity and ionization from the standpoint of the lewis theory of valence. *J. Am. Chem. Soc.*, 42:1419–1433, 1920.

[24] L Pouling. *The Nature of the Chemical Bond*. Cornell University Press, Ithaca, 1939.

[25] Arunan Elangannan et al. *Definition of the hydrogen bond (IUPAC Recommendations 2011)*, volume 83. 1997.

[26] E. R. Lippincott and R. Schroeder. One-dimensional model of the hydrogen bond. *J. Chem. Phys.*, 23(6):1099–1106, 1955.

[27] A. D. Boese. Density functional theory and hydrogen bonds: Are we there yet? *ChemPhysChem*, 16:978–985, 2015.

[28] H. Yin, H. Li, G. Xia, C. Ruan, Y. Shi, H. Wang, M. Jin, and D. Ding. A novel non-fluorescent excited state intramolecular proton transfer phenomenon induced by intramolecular hydrogen bonds: An experimental and theoretical investigation. *Sci. Rep.*, 6:19774, 2016.

[29] Xin-Zheng Li, Brent Walker, and Angelos Michaelides. Quantum nature of the hydrogen bond. *P. Natl. A. Sci. USA*, 108(16):6369–6373, 2011.

[30] A Jayaraman. Ultrahigh pressure. *Rev. Sci. Instrum.*, 57:1013–1031, 1986.

[31] A. K. Singh, C. Balasingh, H. K. Mao, R. J. Hamely, and J. Shu. Analysis of lattice strain measured under non-hydrostatic pressure. *J. Appl. Phys.*, 83:7567 – 7575, 1998.

[32] P. Vinet, J. Ferrante, J. R. Smith, and J. H. Rose. A universal equation of state for solids. *J. Phys. C: Solid State*, pages L446–473, 1986.

[33] R. Jeanloz. Universal equation of state. *Phys. Rev. B*, 38:805–807, 1988.

[34] W. B. Holzapfel. *Equation of State and Scaling Rules for Molecular Solids Under Strong Compresion.* Pucci, R. and Piccitto, G., Elsevier, Amsterdam, 1991.

[35] S. J. Clark, G. J. Ackland, and J. Crain. Theoretical stability limit of diamond at ultrahigh pressure. *Phys. Rev. B*, 52:15035–15038, 1995.

[36] J. Sun, D. D. Klug, and R. Martonak. Structural transformations in carbon under extreme pressure: Beyond diamond. *J. Chem. Phys.*, 130(19):194512, 2009.

[37] L. Dubrovinsky, N Dubrovinskaia, E. Bykova, M. Bykov, V. Prakapenka, C. Prescher, K. Glazyrin, H. P. Liermann, M. Hanfland, M.and Ekholm, Q. Feng, L. V. Pourovskii, M. I. Katsnelson, J. M. Wills, and Abrikosov I. A. The most incompressible metal osmium at static pressures above 750 gpa. *Nat.*, 525:226–229, 2015.

[38] R. C. Liebermann. The future of high-pressure mineral physics. *Earth and Space Science News*, 86(40):365–373, 2005.

[39] R. J. Hamely and N. W. Aschroft. The revealing role of pressure in the condenced matter science. *Physica Today*, 51:26–32, 1998.

[40] G. Jaeger. The ehrenfest classification of phase transitions: Introduction and evolution. *Arch. Hist. Exact Sc.*, 53:51–81, 1998.

[41] A. P. Drozdov, M. I. Eremets, I. A. Troyan, V. Ksenofontov, and S. I. Shylin. Conventional superconductivity at 203 kelvin at high pressures in the sulfur hydride system. *Earth and Space Science News*, 525:73–76, 2015.

[42] C. C. Trout and J. V. Badding. Solid state polymerization of acetylene at high pressure and low temperature. *J. Phys. Chem. B*, 104:8142–8145, 2000.

[43] L. Ciabini, M. Santoro1, F. A. Gorelli1, R. Bini, V. Schettino, and S. Raugei. Triggering dynamics of the high-pressure benzene amorphization. *Nat. Mat.*, 6:39–43, 2007.

[44] Z. Zhao, H. Zhang, H. Yuan, S. Wang, Y. Lin, Q. Zeng, G. Xu, Z. Liu, G. K. Solanki, K. D. Patel, Y. Cui, H. Y. Hwang, and W. L. Mao. Pressure induced metallization with absence of structural transition in layered molybdenum diselenide. *Nat. Comm.*, 6, 2015.

[45] R. P. Dias and I. F. Silvera. Observation of the wigner-huntington transition to metallic hydrogen. *Science*, 355:715–718, 2017.

[46] W. J. Nellis, A. L. Ruoff, and I. F. Silvera. Has metallic hydrogen been made in a diamond anvil cell? *Arxiv, arXiv:1201.0407[cond-mat.other]*, 2012.

[47] M. I. Eremets, M. Emets, and I. A. Troyan. Conductive dense hydrogen. *Nat. Mat.*, 10:927–931, 2011.

[48] Y. Meng, R. Hrubiak, E. Rod, R. Boehler, and G. Shen. New developments in laser-heated diamond anvil cell with in-situ synchrotron x-ray diffraction at high pressure collaborative access team. *Rev. Sci. Instrum.*, 86(7):072201–, 2015.

[49] C. S. Yoo, N. C. Holmes, M. Ross, D. J. Webb, and C. Pike. Shock temperature and melting of iron at earth core condition. *Phys. Rev. Lett.*, 70:3931–3934, 1993.

[50] R. Cauble, D. W. Phillion, T. J. Hoover, J. D. Kilkenny, and R. W. Lee. Demonstration of 0.75 gbar planar shock in x-ray driven colliding foils. *Phys. Rev. Lett.*, 70:2102–2105, 1993.

[51] L. C. Mingand and W. A. Bassett. Laser heating in diamond anvil press up to 2000°c sustained and 3000°c pulsed at pressure up to 260 kilobar. *Rev. Sci. Instrum.*, pages 1115–1118, 1974.

[52] S. Pasternak, G. Aquilanti, S. Pascarelli, R. Poloni, B. Canny, M. V. Coulet, and L. Zhang. A diamond anvil cell with resistive heating for high pressure and high temperature x-ray diffraction and absorption studies. *Rev. Sci. Instrum.*, 79(8):085103, 2008.

[53] Z. Jenei, H. Cynn, K. Visbeck, and W. J. Evans. High-temperature experiments using a resistively heated high-pressure membrane diamond anvil cell. *Rev. Sci. Instrum.*, 84:095114, 2013.

[54] A. I. Schiferl, C. katz, C. Vanderborgh, L. C. Schmidt, R. L. Mills, E. F. Skelton, S. B. Qadri, A. W. Webb, and W. T. Elam. *In Proceedings of The Xth AIRAPT Conference, Amsterdem*, 1986.

[55] R. Boehlar, M. Nicol, C. S. Zha, and M. L. Jhonson. *In Proceedings of The Xth AIRAPT Conference, Amsterdem*, 1986.

[56] R. Boehlar. Temperature in earth core from melting point measurements of iron at high static pressure. *Nat.*, 363:534–536, 1993.

[57] N. A. Lanzillo, J. B. Thomas, B. Watson, M. Washington, and S. K. Nayak. Pressure-enabled phonon engineering in metals. *P. Natl. Acad. Sci. USA*, 111(3):8712–8716, 2014.

[58] D. Pan, L. Spanu, B. Harrison, D. A. Sverjensky, and G. Galli. Dielectric properties of water under extreme conditions and transport of carbonates in the deep earth. *P. Natl. Acad. Sci. USA*, 110(17):6646–6650, 2013.

[59] M. Grimsditch and P. Vavassori. The diffracted magneto-optic kerr effect: What does it tell you? *J. Phys.: Condens. Mat.*, 16(9):R275, 2004.

[60] V. V. Shchennikov and S. V. Ovsyannikov. High-pressure thermopower of sulfur. *Physics of the Solid State*, 45(4):619–622, 2003.

[61] N. Kimura, M. Endo, T. Isshiki, S. Minagawa, A. Ochiai, H. Aoki, T. Terashima, S. Uji, T. Matsumoto, and G. G. Lonzarich. de haas van alphen effect in zrzn$_2$ under pressure: Crossover between two magnetic states. *Phys. Rev. Lett.*, 92:197002, 2004.

[62] H. Yamada, K. Nishikawa, M. Honda, T. Shimura, K. Akasaka, and K. Tabayashi. Pressure-resisting cell for high-pressure, high-resolution nuclear magnetic resonance measurements at very high magnetic fields. *Rev. Sci. Instrum.*, 72(2):1463–1471, 2001.

[63] K. Koyama, S. Hane, K. Kamishima, and T. Goto. Instrument for high resolution magnetisation measurements at high pressure, high magnetic field and low temperature. *Rev. Sci. Instrum.*, 62:2988–2990, 1991.

[64] J. Sanchez-Benitez, S. Tancharakorn, M. K. Hutchison, and K. V. Kamenev. High-pressure cell for a squid magnetometer with a plug for in-situ pressure measurements. *J. Phys.: Conference Series*, 121(12):122001, 2008.

[65] M. Matsui, K. Komatsu, E. Ikeda, A. Sano-Furukawa, H. Gotou, and T Yagi. The crystal structure of δ-al(oh)$_3$: Neutron diffraction measurements and ab-initio calculations. *Am. Mineral.*, 96(5-6):854–859, 2011.

[66] A. Sano-Furukawa, K. Komatsu, C. B. Vanpeteghem, and E. Ohtani. Neutron diffraction study of δ-alood at high pressure and its implication for symmetrization of the hydrogen bond. *Am. Mineral.*, 93(10):1558–1567, 2008.

[67] R. Iizuka, K. Komatsu, H. Kagi, T. Nagai, A. Sano-Furukawa, T. Hattori, H. Gotou, and T. Yagi. Phase transitions and hydrogen bonding in deuterated calcium hydroxide: High-pressure and high-temperature neutron diffraction measurements. *J. Solid State Chem.*, 218:95 – 102, 2014.

[68] E. Kermarrec, J. Gaudet, K. Fritsch, R. Khasanov, Z. Guguchia, C. Ritter, K. A. Ross, H. A. Dabkowska, and B. D. Gaulin. Ground state selection under pressure in the quantum pyrochlore magnet yb$_2$ti$_2$o$_7$. *Nat. Commun.*, 8:14810, 2017.

[69] P. S. Salmon and A. Zeidler. Network under pressure: the development of in-situ high-pressure diffraction for glassy and liquid materials. *J. Phys.: Condens. Matter*, 27:133201, 2015.

[70] M. Woiska, S. Grabowsky, P. M. Dominiak, K. Woniak, and D. Jayatilaka. Hydrogen atoms can be located accurately and precisely by x-ray crystallography. *Science Advances*, 2(5), 2016.

[71] C. Balny. What lies in the future of high-pressure bioscience? *BBA - Proteins Proteom.*, 1764(3):632 – 639, 2006.

[72] P. M. Oger, I. Daniel, and A. Picard. In-situ raman and x-ray spectroscopies to monitor microbial activities under high hydrostatic pressure. *Annals of the New York of science*, 1189:113–120, 2010.

[73] T. Armbruster, T. Kohler, E. Libowitzky, A. Friedrich, R. Miletich, M. Kunz, O. Medenbach, and J. Gutzmer. Structure, compressibility, hydrogen bonding, and dehydration of the tetragonal mn^{3+} hydrogarnet, henritermierite. *Am. Mineral.*, 86(1-2):147–158, 2001.

[74] A. Kartusiak. High-pressure x-ray diffraction study on the structure and phase transition of 1,3-cyclohexanedione crystals. *Acta. Cryst.*, B46:246–256, 1990.

[75] A. Katrusiak. High-pressure x-ray diffraction study of 2-methyl 1,3-cyclopentanedione crystals. *High Pressure Res.*, 6(3):155–167, 1991.

[76] A. Katrusiak. High-pressure x-ray diffraction study of dimedone. *High Pressure Res.*, 6(5):265–275, 1991.

[77] A. Katrusiak. High-pressure x-ray diffraction study of dimedone. *Phys. Rev. B*, B48:2992, 1993.

[78] D. V. Korabelnikov and Yu. N. Zhuravlev. Positive and negative linear compressibility and electronic properties of energetic and porous hybrid crystals with nitrate anions. *Phys. Chem. Chem. Phys.*, 18:33126–33133, 2016.

[79] Andres C., Marc T., and Pietro C. Stability of the different alooh phases under pressure. *J. Phys.: Condensed Matter*, 28(18):185401, 2016.

[80] A. Katrusiak. High-pressure x-ray diffraction study of pentaerythritol. *Acta. Cryst.*, B51:873–879, 1995.

[81] E. Magos-Palasyuk, K. J. Fijalkowski, and T. Palasyuk. Chemically driven negative linear compressibility in sodium amidoborane, na(nh$_2$bh$_3$). *Sci. Rep.*, 6:28745, 2016.

[82] T. Ito, H. Hirata, and S. Fujita. Effect of hydrogen bonding on the anisotropy of the hydrostatic compressibility of polymer crystals. *J.Polym. Sci.*, 17:1237–1250, 1979.

[83] E. V. Boldyreva, T. P. Shakhtshneider, M. A. Vasilchenko, H. Ahsbahs, and H. Uchtmann. Anisotropic crystal structure distortion of the monoclinic polymorph of acetaminophen at high hydrostatic pressures. *Acta. Cryst.*, B56:299–308, 2000.

[84] E.V. Boldyreva, T.P. Shakhtshneider, H. Ahsbahs, H. Uchtmann, E.B. Burgina, and V.P. Baltakhinov. The role of hydrogen bonds in the pressure-induced structural distortion of 4-hydroxyacetanilide crystals. *Pol. J. Chem.*, 76(9):1333–1346, 2002.

[85] E.V. Boldyreva, H. Ahsbahs, and H.-P. Weber. A comparative study of pressure-induced lattice strain of α and γ-polymorphs of glycine. *Zeitschrift fur Kristallographie*, 218:231–236, 2003.

[86] E.V. Boldyreva, T.P. Shakhtshneider, H. Ahsbahs, H. Sowa, and H. Uchtmann. Effect of high pressure on the polymorphs of paracetamol. *J. Therm. Anal. Calorim.*, 68(2):437–452, 2002.

[87] P. W. Bridgman. Recent work in the field of high pressures. *Rev. Mod. Phys.*, 18:1–93, 1946.

[88] T. Yan, K. Wang, X. Tan, J. Liu, B. Liu, and B. Zou. Exploration of the hydrogen-bonded energetic material carbohydrazide at high pressures. *J. Phys. Chem. C*, 118(40):22960–22967, 2014.

[89] G. M. Borstad, I. G. Batyrev, and J. A. Ciezak-Jenkins. Cyanoacetohydrazide under pressure: Chemical changes in a hydrogen-bonded material. *J. Phys. Chem. B*, 120(17):2712–2719, 2016.

[90] S. Kitagawa and K. Uemura. Dynamic porous properties of coordination polymers inspired by hydrogen bonds. *Chem. Soc. Rev.*, 34:109–119, 2005.

[91] B. H. Ye, M.-L. Tong, and X.-M. Chen. Metal-organic molecular architectures with 2,2'-bipyridyl-like and carboxylate ligands. *Coordin. Chem. Rev.*, 249(5-6):545–565, 2005.

[92] S. Kitagawa, R. Kitaura, and S.-I. Noro. Functional porous coordination polymers. *Angewandte Chemie - International Edition*, 43(18):2334–2375, 2004.

[93] C. Janiak. Engineering coordination polymers towards applications. *Dalton T.*, (14):2781–2804, 2003.

[94] A.M. Beatty. Open-framework coordination complexes from hydrogen-bonded networks: Toward host/guest complexes. *Coordin. Chem. Rev.*, 246(1-2):131–143, 2003.

[95] S. Nandi, D. Chakraborty, and R. Vaidhyanathan. A permanently porous single molecule h-bonded organic framework for slective co_2 capture. *Chem. Commun.*, 52:7249–7252, 2016.

[96] J. Tian, Zi-Yue Xu, H. Wang, S.-H. Xie, Da-Wen Xu, Y.-H. Ren, H. Wang, Y. Liu, and Z.-T. Li. Supramolecular metal-organic frameworks that display high homogeneous and heterogeneous photocatalytic activity for h_2 production. *Nat. Commun.*, 7:11580, 2016.

[97] G. Gilli and P. Gilli. *The Nature of Hydrogen Bond*. Oxford University Press, 2009.

[98] W. B. Holzapfel. On the symmetry of the hydrogen bonds in ice vii. *J. Chem. Phys.*, 56(2):712–715, 1972.

[99] I. Errea, M. Calandra, C. J. Pickard, J. R. Nelson, R. J. Needs, Y. Li, H. Liu, Y. Zhang, Y. Ma, and F. Mauri. Quantum hydrogen-bond symmetrization in the superconducting hydrogen sulfide system. *Nat.*, 532:81–84, 2016.

[100] D. Duan, F. Tian, Z. He, X. Meng, L. Wang, C. Chen, X. Zhao, B. Liu, and T. Cui. Hydrogen bond symmetrization and superconducting phase of hbr and hcl under high pressure: An ab-initio study. *J. Chem. Phys.*, 133(7):074509, 2010.

[101] L. E. Bove, R. Gaal, Z. Raza, A. A. Ludl, S. Klotz, A. M. Saitta, A. F. Goncharov, and P. Gillet. Effect of salt on the h-bond symmetrization in ice. *P. Natl. A. Sci. USA*, 112(27):8216–8220, 2015.

[102] A. Hushur, M. H. Manghnani, J. R. Smyth, Q. Williams, E. Hellebrand, D. Lonappan, Y. Ye, P. Dera, and D. J. Frost. Hydrogen bond symmetrization and equation of state of phase d. *J. Geophys. Res: Sol. Ea.*, 116(B6), 2011.

[103] A. R. Ubbelohde and K. J. Gallagher. Acid base effects in hydrogen bond in crystals. *Prog. Theor. Phys.*, 67, 1955.

[104] A. C. Legon and Millen D. J. Systematic effect of d substitution on hydrogen-bond length in gas phase dimer b- - -hx and a model for its interpretation. *Chem. Phys. Lett.*, 147, 1988.

[105] Z. Men, W. Fang, D. Li, Z. Li, and C. Sun. Raman spectra from symmetric hydrogen bonds in water by high-intensity laser-induced breakdown. *Sci. Rep.*, 4, 2014.

[106] L. Bondesson, K. V. Mikkelsen, Y. Luo, P. Garberg, and H Agren. Hydrogen bonding effects on infrared and raman spectra of drug molecules. *Spectrochim. Acta Part A: M*, 66(2):213–224, 2007.

[107] H. G. M. Edwards, I. B. Hutchinson, R. Ingley, J. Parnell, P. Vitek, and J. Jehlicka. Raman spectroscopic analysis of geological and biogeological specimens of relevance to the exomars mission. *Astrobiology*, 13(6):543–549, 2013.

[108] X. Zhang, Q. H. Tan, J. B. Wu, W. Shi, and P.-H. Tan. Review on the raman spectroscopy of different types of layered materials. *Nanoscale*, 8:6435–6450, 2016.

[109] A. Singh, D. Gangopadhyay, R. Nandi, P. Sharma, and R. K. Singh. Raman signatures of strong and weak hydrogen bonds in binary mixtures of phenol with acetonitrile, benzene and orthodichlorobenzene. *J. Raman Spect.*, 47:712–719, 2016.

[110] S. H. Gordon, X. Cao, A. Mohamed, and J. L. Willett. Infrared spectroscopy method reveals hydrogen bonding and intermolecular interaction between components in polymer blends. *J. Appl. Polym. Sci.*, 97:813–821, 2005.

[111] M. Tasumi. *Introduction to Experimental Spectroscopy Fundamental and Practical Methods*. John Wiley, Chennai, first edition.

[112] J.R.E. Dunsmuir and A.P. Lane. Effects of hydrogen bonding on the infrared spectra of some complex ammonium halides. *Spectrochim. Acta Part A: M*, 28(1):45–50, 1972.

[113] G. B. Tolstorozhev, M. V. Belkov, I. V. Skornyakov, O. K. Bazyl, V. Ya. Artyukhov, G. V. Mayer, O. I. Shadyro, P. V. Kuzovkov, S. D. Brinkevich, and S. N. Samovich. Infrared spectroscopy of hydrogen bonds in benzoic acid derivatives. *J. Appl. Spectrosc.*, 81(1):109–117, 2014.

[114] C. J. Fecko, J. D. Eaves, J. J. Loparo, A. Tokmakoff, and P. L. Geissler. Ultrafast hydrogen-bond dynamics in the infrared spectroscopy of water. *Science*, 301:698–1702, 2003.

[115] G. Nielsen and H. Schwalbe. Protein nmr spectroscopy: Hydrogen bonds under pressure. *Nat. Chem.*, 4:693–695, 2012.

[116] T. Okuchi, G. D. Cody, H. K. Mao, and R. J. Hemley. Hydrogen bonding and dynamics of methanol by high-pressure diamond-anvil cell nmr. *J. Chem. Phys.*, 122(24):244509, 2005.

[117] M. Elias, D. Liebschner, J. Koepke, C. Lecomte, B. Guillot, C. Jelsch, and E. Chabriere. Hydrogen atoms in protein structures: High-resolution x-ray diffraction structure of the df phase. *BMC Research Notes*, 6(308), 2013.

[118] M. Woinska, S. Grabowsky, P. M. Dominiak, K. Wozniak, and D. Jayatilaka. Hydrogen atoms can be located accurately and precisely by x-ray crystallography. *Science*, 2(5), 2016.

[119] C. J. Sahle, C. Sternemann, C. Schmidt, S. Lehtola, S. Jahn, L. Simonelli, S. Huotari, M. Hakala, T. Pylkkanen, A. Nyrow, K. Mende, M. Tolan, K. Hamalainen, and M. Wilke. Microscopic structure of water at elevated pressures and temperatures. *P. Natl. A. Sci. USA*, 110(16):6301–6306, 2013.

[120] J. R. Asay and M. Shahinpoor. *High-Pressure Shock Compression of Solids*. Springer, New York, 1993.

[121] A. N. Dremin. Shock wave chemistry. *High Pressure Res.*, 1(5-6):361–364, 1989.

[122] P. W. Bridgman. *The Physics of High Pressure*. Dover Publications, New York, 1931.

[123] P. W. Bridgman. Compressibilities and electrical resistance under pressure, with special reference to intermetallic compounds. *P. Natl. A. Sci. USA*, 70(7):285–317, 1935.

[124] P. W. Bridgman. The physics of high pressure. *Bell Lab*, 1949.

[125] A. Van Valkenburg. Diamond high pressure window. *Diamond Research*, pages 17–19, 1964.

[126] K. Syassen. Ruby under pressure. *High Pressure Res.*, 28:75–126, 2008.

[127] R. A. Forman, G. J. Piermarini, J. D. Barnett, and Block S. Pressure measurement made by the utilization of ruby sharp-line luminescence. *Science*, 176(4032):284–285, 1972.

[128] G.J. Piermarini, S. Block, and J.D. Barnett. Hydrostatic limits in liquids and solids to 100 kbar. *J. Appl. Phys.*, 44:5377–5382, 1973.

[129] S. Klotz, J. C. Chervin, P. Munsch, and G. Le Marchand. Hydrostatic limits of 11 pressure transmitting media. *J. Phys. D: Appl. Phys.*, 42, 2009.

[130] R. J. Angel, M. Bujak, J. Zhao, G. D. Gatta, and S. D. Jacobsen. Effective hydrostatic limits of pressure media for high-pressure crystallographic studies. *J. Appl. Cryst.*, 40:26–32, 2007.

[131] W. A. Bassett. Diamond anvil cell, 50th birthday. *High Pressure Res.*, 29:163–186, 2009.

[132] P. V. Bridgman. *Proc. Roy. Soc.*, 203:1–17, 1950.

[133] L. B. Craig, G. Malcolm, K. Stefan, P. Julien, S. Thierry, J. N. Richard, S. L. John, and H. Gerard. Toroidal anvils for single-crystal neutron studies. *High Pressure Res.*, 25(4):229–231, 2005.

[134] A. Sano-Furukawa, T. Hattori, H. Arima, A. Yamada, S. Tabata, M. Kondo, A. Nakamura, H. Kagi, and T. Yagi. Six-axis multi-anvil press for high-pressure, high-temperature neutron diffraction experiments. *Rev. Sci. Instrum.*, 85(11):113905, 2014.

[135] C. E. Weir, E. R. Lippincott, A. Van Valkenburg, and E. N. Bunting. Infrared studies in the 1- to 15-micron region to 30,000 atmospheres. *J. Res. Natl. Bur. Stand.*, 63A:55–62, 1959.

[136] A. W. Lawson and T. Y. Tang. A diamond bomb for obtaning powder picture at high pressure. *Rev. Sci. Instrum.*, 21:815, 1950.

[137] H. K. Mao and P. M. Bell. *Carniegie Institute of Wasington Year Book*, volume 77. Carniegie Institute of Wasington, 1978.

[138] L. Merrill and W. A. Bassett. Observation of the wigner-huntington transition to metallic hydrogen. *Rev. Sci. Instrum.*, 45:0034–6748, 1974.

[139] S. Scandolo, G. L. Chiarotti, and E. Tosatti. Stability of diamond at megabar pressures. *Phys. Stat. Sol. b*, 198:447–453, 1996.

[140] G. Huber, K. Syassen, and W. B. Holzapfel. Pressure dependence of 4f levels in europium pentaphosphate up to 400 kbar. *Phys. Rev. B*, 15:5123–5128, 1977.

[141] D. He, Y. Zhao, T. U. Sheng, R. B. Schwartz, J. Quian, H. K. Mao, J. Z. Hu, J. Shin, and J. Xu. Bulk mettalic glass gasket for high pressure. *Rev. Sci. Instrum.*, 74:3012 – 3016, 2003.

[142] J. C. Jemieson and M. H. fritz, J. N.Manghnani. *High Pressure Research in Geophysics.* 1982.

[143] G. N. Pegg. *High Pressure High temperature*, volume 12. 1980.

[144] C. S. Zha, H. K. Mao, and R. J. Hamely. Elasticity of mgo and a primary scale to 55 gpa. *Proc. Natl. Acad. Sci. USA*, 97:13494–13499, 2000.

[145] H. K. Mao, P. M. Bell, J. W. shaner, and D. J. Steinberg. Specific pressure measurement of cu, mo, pd, and ag and calibration of the ruby r_1 fluorescence pressure gauge from 0.06 gpa and 1 mbar. *J. Appl. Phys.*, 49:3276–3283, 1978.

[146] P. M. Bell, J. A. Xu, and H. K. Mao. *Static Compression of Gold and Copper and Calibration of the Ruby Pressure Scale to Pressure to 1.8 megabar (static RNO)*. Plenum New York, 1986.

[147] H. K. Mao, J. Xu, and P. M. Bell. Calibration of ruby pressure gauge to 800 kbar under quasi-hydrostatic conditions. *J. Geophys. Res.:Sol. Ea*, 91:4673–4676, 1986.

[148] D. C. Akobuije, W. J. Nellis, A. Soldatov, and I. F. Silvera. The ruby pressure standard to 150 gpa. *J. Appl. Phys.*, 98(11):114905, 2005.

[149] W. B. Holzapfel. Refinement of the ruby luminescence pressure scale. *J. Appl. Phys.*, 93(3):1813–1818, 2003.

[150] Sharma et. al. Theoritical analysis of r-lines shifts of ruby subjected todifferent deformation conditions. *Phys. Rev. B*, 43:879–893, 1991.

[151] J. A. Xu, H. K. Mao, and P. M. Bell. High pressure ruby and diamond fluoscrence observations at 0.21 to 0.55 terapascal. *Science*, 232:1404–1406, 1986.

[152] W. L. Vos and J. A. Schoutan. On the temperature correction to ruby pressure scale. *J. Appl. Phys.*, 69:6744–6746, 1991.

[153] M. I. Eremets. *High Pressure in Experiment*. Oxford University Press, U. K., 1999.

[154] A. Yuichi and K. Haruki. Pressure calibration of diamond anvil raman gauge to 310 gpa. *J. Appl. Phys.*, 100(4):043516, 2006.

[155] J. W. Otto, J. K. Vassiliou, and G. Frommeyer. Nonhydrostatic compression of elastically anisotropic polycrystals. i. hydrostatic limits of 4:1 methanol-ethanol and paraffin oil. *Phys. Rev. B*, 57:3253–3263, 1998.

[156] Y. Shen, R. S. Kumar, M. Pravica, and M. F. Nicol. Characteristics of silicone fluid as a pressure transmitting medium in diamond anvil cells. *Rev. Sci. Instrum.*, 75(11):4450–4454, 2004.

[157] D. D. Ragan, D. R. Clarke, and D. Schiferl. Silicone fluid as a highâĂŘpressure medium in diamond anvil cells. *Rev. Sci. Instrum.*, 67(2):494–496, 1996.

[158] K. Murata, H. Yoshino, H. O. Yadav, Y. Honda, and N Shirakawa. Pt resistor thermometry and pressure calibration in a clamped pressure cell with the medium, daphne 7373. *Rev. Sci. Instrum.*, 68(6):2490–2493, 1997.

[159] P. M. Bell and H. K. Mao. *Carniegie Institute of Wasington Year Book*, volume 80. Carniegie Institute of Wasington, 1981.

[160] D.H. Liebenberg. A new hydrostatic medium for diamond anvil cells to 300 kbar pressure. *Phys. Lett. A*, 73(1):74 – 76, 1979.

[161] R. LeSar, S. A. Ekberg, L. H. Jones, R. L. Mills, L. A. Schwalbe, and D. Schiferl. Raman spectroscopy of solid nitrogen up to 374 kbar. *Solid State Commun.*, 32(2):131 – 134, 1979.

[162] H. K. Mao and P. M. Bell. Observations of hydrogen at room temperature (25c) and high pressure. *Science*, 203:1004–1006, 1979.

[163] H. K. Mao, B. Chen, J. Chen, K. Li, J. F. Lin, W. Yang, and H. Zheng. Recent advances in high-pressure science and technology. *Matter and Radiation at Extremes*, 1:59–75, 2016.

[164] Mao. H. K., C. Kao, and R. J. Hemley. Inelastic x-ray scattering at ultrahigh pressures. *J. Phys.: Condens. Matter*, 13:7847, 2001.

[165] A. Polian. Brillouin scattering at high pressure: An overview. *J. Raman . Specto.*, 34:633–637, 2003.

[166] M. Guthrie. Future directions in high-pressure neutron diffraction. *J. Phys.: Condens. Matter*, 27:153201, 2015.

[167] Y. Hiki and T. Kosugi. Ultrasonic measurements under extreme conditions. part ii.- measurements under high pressure. *J. Phys. Soc. Japan*, 21:23, 1982.

[168] K Ohsumi, S. Sueno, I. Nakai, M. Imafuku, H. Morikawa, M. Kimata, M. Nomura, and O. Shimomura. Exafs measurements under high pressure by diamond anvil cell. *J. Phys. Colloques*, 47:189–192, 1986.

[169] K. Kothapalli, A. E. Bohmer, W. T. Jayasekara, B. G. Ueland, P. Das, A. Sapkota, V. Taufour, Y. Xiao, E. Alp, S. L. Budko, P. C. Canfield, A. Kreyssig, and A. I. Goldman. Strong cooperative coupling of pressure-induced magnetic order and nematicity in fese. *Nat. Comm.*, 7(12728), 2016.

[170] G. Landsberg and L. Mandelstam. Eine neue erscheinung bei der lichtzerstreuung in krystallen. *Naturwissenschaften*, 16:557–558, 1928.

[171] A. Smekal. Zur quantentheorie der dispersion. *Naturwissenschaften*, 11:873–875, 1923.

[172] C. V. Raman. A new radiation. *Indian J. Phys.*, 2:387–398, 1928.

[173] A. F. Goncharov. Raman spectroscopy at high pressure. *Int. J. of Spectr.*, 2012:617528–617542, 2011.

[174] I. N. Goncharenko. Neutron diffraction experiments in diamond and sapphire anvil cells. *High Pressure Res.*, 24(1):193–204, 2004.

[175] J. Ruiz-Fuertes, A. Hirsch, A. Friedrich, B. Winkler, L. Bayarjargal, W. Morgenroth, L. Peters, G. Roth, and V. Milman. High-pressure phase of lapo$_4$ studied by x-ray diffraction and second harmonic generation. *Phys. Rev. B*, 94:134109, 2016.

[176] A. P. Hammersley. Fit2d: An introduction and overview. *ESRF Internal Report, ESRF97HA02T*, 1997.

[177] A.C. Larson and R.B. Von Dreele. General structure analysis system (gsas). *Los Alamos National Laboratory Report LAUR*, pages 86–748, 2000.

[178] B. H. Toby. Expgui, a graphical user interface for gsas. *J. Appl. Cryst.*, 34:210–213, 2001.

[179] A. K. Mishra, C. Murli, N. Garg, R. Chitra, and S. M. Sharma. Pressure-induced structural transformations in bis(glycinium)oxalate. *J. Phys. Chem. B*, 114:17084–17091, 2010.

[180] S. V. Goryainov, E. N. Kolesnik, and E. V. Boldyreva. A reversible pressure-induced phase transition in β-glycine at 0.76 gpa. *Physica B Condens. Matter*, 357:340àĂŞ347, 2005.

[181] A. K. Mishra, C. Murli, and S. M. Sharma. High pressure raman spectroscopic study of deuterated γ-glycine. *J. Phys. Chem. B*, 112:15867–15874, 2008.

[182] E. V. Boldyreva, H. Ahsbahs, and H. P. Weber. A comparative study of pressure-induced lattice strain of α- and γ polymorphs of glycine. *Z. Kristallogr.*, 218:231–236, 2003.

[183] E. V. Boldyreva, S. N. Ivashevskaya, H. Sowa, H. Ahsbahs, and H. P. Weber. Effect of high pressure on the crystalline glycine: a new high-pressure polymorph formation. *Doklady Phys. Chem.*, 396:111, 2004.

[184] E.V. Boldyreva, S. N. Ivashevskaya, H. Sowa, H. Ahsbahs, and H.P. Weber. Effect of hydrostatic pressure on the γ polymorph of glycine. a polymorphic transition into a new δ form. *Z. Kristallogr.*, 220:50–57, 2005.

[185] A. Dawson, D. R. Allan, S. A. Belmonte, S. J. Clark, W. I. F. David, P. A. McGregor, S. Parson, C. R. Pulham, and L. Sawyer. Effect of high pressure on the crystal structures of polymorphs of glycine. *Cryst. Growth Des.*, 4:1415–1427, 2005.

[186] C. Murli, S. Karamakar, S.M. Sharma, and S. K. Sikka. α glycine under high pressures: a raman scattering study. *Physica B Condens. Matter*, 339:23–30, 2003.

[187] S. V. Goryainov, E. N. Kolesnik, and E. V. Boldyreva. A reversible pressure-induced phase transition in β-glycine at 0.76 gpa. *Physica B Condens. Matter*, 357:340–347, 2005.

[188] N. A. Tumanov, E. V. Boldyreva, and H. Ahsbahs. Structure solution and refinement from powder or single-crystal diffraction data pros and cons: An example of the high-pressure β-polymorph of glycine. *Powder Diffr.*, 23:307–316, 2008.

[189] H. N. Bordallo, E. V. Boldyreva, A. Buchsteiner, M. M. Koza, and S. Landsgesell. Structure-property relationships in the crystals of the smallest amino acid: an incoherent inelastic neutron scattering study of the glycine polymorphs. *J. Phys. Chem B.*, 112:8748–8759, 2008.

[190] A. M. R. Teixeira, P. T. C. Freire, A. J. D. Moreno, J. M. Sasaki, A. P. Ayala, J. M. Filho, and F. E. A. Melo. High-pressure raman study of l-alanine crystal. *Solid State Commun.*, 116:405–409, 2000.

[191] R. O. Gonclaves, P. T. C. Freire, H. N. Bordallo, J. A. Lima, Jr. Lima, F. E. A. Melo, J. M. Filho, D. N. Argyriou, and R. J. C. Lima. High-pressure raman spectra of deuterated l-alanine crystal. *J. Raman Spectrosc.*, 40:958–963, 2009.

[192] J. S. Olsen, L. Gerward, P. T. C. Freire, J. Mendes, F. E. A. Melo, and A. G. Souza. Pressure-induced phase transformation in l-alanine crystals. *J.Phys. Chem. Solids*, 69:1641–1645, 2008.

[193] N. A. Tumanov, E. V. Boldyreva, B. A. Kolesov, A. V. Kurnosov, and R. Q. Cabrera. Pressure-induced phase transitions in l-alanine. *Acta Crystallogr.*, B66:458–471, 2010.

[194] N. P. Funnell, A. Dawson, D. Francis, A. R. Lennie, W.G. Marshall, S. A. Moggach, J. E. Warren, and S. Parsons. The effect of pressure on the crystal structure of l-alanine. *CrystEngComm.*, 12:2573–2583, 2010.

[195] V. S. Minkov, A. S. Krylov, E. V. Boldyreva, S. V. Goryainov, S. N. Bizyaev, and A. N. Vtyurin. Pressure-induced phase transitions in crystalline l- and dl-cysteine. *J. Phys. Chem. B*, 112:8851–8854, 2008.

[196] S. A. Moggach, D. R. Allan, S. J. Clark, S. Gutmann, M. J.and Parsons, C. R. Pulham, and L. Sawyer. High-pressure polymorphism in l-cysteine: the crystal structures of l-cysteine-iii and l-cysteine-iv. *Acta Crystallogr B.*, 62:296–309, 2006.

[197] C. Murli, R. Vasanthi, and S. M. Sharma. Raman spectroscopic investigations of dl-serine and dl-valine under pressure. *Chem. Phys.*, 331:77–84, 2006.

[198] E.V. Boldyreva, E.N. Kolesnik, T.N. Drebushchak, H. Sowa, H. Ahsbahs, and Y.V. Seryotkin. A comparative study of the anisotropy of lattice strain induced in the crystals of dl-serine by cooling down to 100 k, or by increasing pressure up to 8.6 gpa. a comparison with l-serine. *Z. Kristallogr.*, 221:150–161, 2006.

[199] T. N. Drebushchak, H. Sowa, Y. V. Seryotkin, E. V. Boldyreva, and H. Ahsbahs. L-serine iii at 8.0 gpa. *Acta Cryst.*, E62:4052–4054, 2006.

[200] S. A. Moggach, W. G. Marshall, and S. Parsons. High-pressure neutron diffraction study of l-serine-i and l-serine-ii, and the structure of l-serine-iii at 8.1 gpa. *Acta Cryst.*, B62:815–825, 2006.

[201] A. J. D. Moreno, P. T. C. Freire, F. E. A. Melo, M.A.A. Silva, I. Gudes, and J. M. Mendes. Pressure-induced phase transitions in monohydrated l-asparagine aminoacid crystals. *Sol. Stat. Comm.*, 103:655–658, 1997.

[202] P. F. F. Filho, P. T. C. Freire, F. E. A. Melo, V. Lemov, J. M. Filho, P. S. Pizani, and D. Z. Rossato. Pressure-induced phase transitions in l-leucine crystal. *J. Raman. Spectrosc.*, 40:46–51, 2009.

[203] A.S. Sabino, G.P. De Sousa, C. Luz-Lima, P.T.C. Freire, F.E.A. Melo, and J. M. Filho. High-pressure raman spectra of l-isoleucine crystals. *Solid State Commun.*, 149:1553–1556, 2009.

[204] J. A. Lima, P. T. C. Freire, F. E. A. Melo, V. Lemos, J. M. Filho, and P. S. Pizani. High pressure raman spectra of l-methionine crystal. *J. Raman. Spectrosc.*, 39:1356–1363, 2008.

[205] R. J. C. Lima, A. M. R. Teixeira, P. T. C. Freire, J. M. Sasaki, A. P. Ayala, F. E. A. Melo, and J. M. Filho. High-pressure raman study of taurine crystal. *J. Raman. Spectrosc.*, 32:27–32, 2001.

[206] J. M. de Souza, R. J. C. Lima, P. T. C. Freire, J. M. Sasaki, F. E. A. Melo, J. Mendes, and D. W. Jones. Raman spectra of deuteriated taurine single crystals. *Spectrochim. Acta A*, 61:1525–1527, 2005.

[207] B. L. Silva, P. T. C. Freire, F. E. A. Melo, J. M. Filho, M. A. Pimenta, and M. S. S. Dantas. High-pressure raman spectra of l-threonine crystal. *J. Raman. Spectrosc.*, 31:519–522, 2000.

[208] J. Herminio da Silva, V. Lemos, P. T. C. Freire, F. E. A. Melo, J. M. Filho, J. A. Lima Jr., and P. S. Pizani. Stability of the crystal structure of l-valine under high pressure. *Phys. Stat. Sol. B*, 246:553–557, 2009.

[209] E. V. Boldyreva. Combined x-ray diffraction and raman spectroscopy studies of phase transitions in crystalline amino acids at low temperatures and high pressures: selected examples. *Phase Transit.*, 82:303–321, 2009.

[210] E. V. Boldyreva. High-pressure diffraction studies of molecular organic solids. a personal view. *Acta Cryst. A*, 64:218–231, 2008.

[211] V. S. Minkov, E. V. Goryainov, S. V.and Boldyreva, and C. H. GÃűrbitz. Raman study of pressure-induced phase transitions in crystals of orthorhombic and monoclinic polymorphs of l-cysteine: dynamics of the side chain. *J. Raman. Spectrosc.*, 41(10):1748–1758, 2010.

[212] V. S. Minkov, N. A. Tumanov, R. Q. Cabrera, and E. V. Boldyreva. Low temperature/high pressure polymorphism in dl-cysteine. *CrystEngComm.*, 12:2551–2560, 2010.

[213] E. N. Kolesnik, S. V. Goryainov, and E. V. Boldyreva. Different behavior of l- and dl-serine crystals at high pressures: Phase transitions in l-serine and stability of the dl-serine structure. *Doklady Phys. Chem.*, 404:169–172, 2005.

[214] E.V. Boldyreva, H. Sowa, Yu.V. Seryotkin, T.N. Drebushchak, H. Ahsbahs, V. Chernyshev, and V. Dmitriev. Pressure-induced phase transitions in crystalline l-serine studied by single-crystal and high-resolution powder x-ray diffraction. *Chem. Phys. Lett.*, 429:474–478, 2006.

[215] S. A. Moggach, W. G. Marshall, D. M. Rogers, and S. Parsons. How focussing on hydrogen bonding interactions in amino acids can miss the bigger picture: a high-pressure neutron powder diffraction study of ϵ-glycine. *CrystEngComm*, 17:5315–5328, 2015.

[216] K. Machida, A. Kagayama, Y. Saito, Y. Kuroda, and T. Uno. Vibrational spectra and intermolecular potential of the α-form crystal of glycine. *Spectrochim. Acta A*, 33:569–574, 1977.

[217] S. A. S. Ghazanfar, D. V. Myers, and J. T. Edsall. Raman spectra of carbon-deuterated glycine in various ionic forms. *J. Am. Chem. Soc.*, 86:3439–3444, 1964.

[218] R.O. Holanda, P.T.C. Freire, J.A.F. Silva, F.E.A. Melo, J. M. Filho, and J.A. Lima Jr. High pressure raman spectra of d-threonine crystal. *Vib. Spectrosc.*, 67:1 – 5, 2013.

[219] R.O. Holanda, J.A. Lima Jr., P.T.C. Freire, F.E.A. Melo, J. Mendes Filho, and A. Polian. New pressure-induced phase transitions of l-threonine crystal: A raman spectroscopic study. *J. Mol. Struct.*, 1092:160 – 165, 2015.

[220] K. Machida, A. Kagayama, and Y. Saito. Polarized raman spectra and intermolecular potential of α-glycine-c-d2 and dl-alanine α,β-d4 crystals. *J. Raman. Spectrosc.*, 8:133–138, 1979.

[221] P. G. Jonsson and A. Kvick. Precision neutron diffraction structure determination of protein and nucleic acid components. iii. the crystal and molecular structure of the amino acid α glycine. *Acta Cryst.*, B28:1827–1833, 1972.

[222] B. A. Kolesov and E. V. Boldyreva. Self-trapped n-h vibrational states in the polymorphs of glycine, l- and dl-alanine. *J. Raman. Spectrosc.*, 41:670–677, 2010.

[223] C. Murli, S. Thomas, S. Venkateswaran, and S. M. Sharma. Raman spectroscopic investigation of α-glycine at different temperatures. *Physica B*, 364:233–238, 2005.

[224] J. V. H. Benjamin, W. A. Szostak, D. N. Shchepkin, Z. Havlas, and P. Hobza. The nature of improper, blue-shifting hydrogen bonding verified experimentally. *J. Am. Chem. Soc.*, 123:12290–12293, 2001.

[225] S. K. Sikka. On some hydrogen bond correlations at high pressures. *High Press. Res.*, 27:313–319, 2007.

[226] P. Colomban, G. Sagon, M. Lesage, and J. M. H. Ramirez. Micro-raman study of the compressive behaviour of advanced pa66 polyamide fibres in a diamond-anvil cell. *Vib. Spectrosc.*, 37:83–90, 2005.

[227] P. Colomban. Nanomechanics of advanced polymer fibres. *Compos. Sci. Technol.*, 69:1437–1441, 2009.

[228] P. Colomban and G. Gouadec. Raman and ir micro-analysis of high performance polymer fibres tested in traction and compression. *Compos. Sci. Technol.*, 69:10–16, 2009.

[229] S. V. Goryainov and E. V. Kolesnik, E. N.and Boldyreva. A reversible pressure-induced phase transition in β-glycine at 0.76 gpa. *Physica B: Cond. Matter*, 357(3-4):340–347, 2005.

[230] A. K. Mishra, C. Murli, and S. M. Sharma. High pressure raman spectroscopic study of deuterated γ-glycine. *J. Phys. Chem. B*, 112(49):15867âĂŞ15874, 2008.

[231] A. F. Goncharov, M. R. Manaa, J. M. Zaug, R. H. Gee, L. E. Fried, and W. B. Montgomery. Polymerization of formic acid under high pressure. *Phys. Rev. Lett.*, 94:065505, 2005.

[232] A. Katrusiak. Macroscopic and structural effects of hydrogen-bond transformations. *Crystallogr. Rev*, 5:133–175, 1996.

[233] A. Katrusiak. Macroscopic and structural effects of hydrogen-bond transformations. *NATO Sci. Peace Secur.*, 5:1993, 2010.

[234] A. Katrusiak. Macroscopic and structural effects of hydrogen-bond transformations: some recent directions. *Crystallogr. Rev*, 9:87–89, 2003.

[235] E. V. Boldyreva. High-pressure diffraction studies of molecular organic solids. a personal view. *Acta Cryst.*, 64:218–231, 2008.

[236] E. V. Boldyreva. High-pressure studies of the hydrogen bond networks in molecular crystals. *J. Mol. Struct.*, 700:151–155, 2004.

[237] E. V. Boldyreva. High-pressure-induced structural changes in molecular crystals preserving the space group symmetry: anisotropic distortion/isosymmetric polymorphism. *Cryst. Eng.*, 6:235–254, 2003.

[238] N. G. Golubeva and A. O. Velikanov. Raman spectroscopy study of the process of polymerization of polyacrylamide gel. *J. Appl. Spectrosc.*, 53(6):954–957, 1990.

[239] M. K. Gupta and R. Bansil. Laser raman spectroscopy of polyacrylamide. *J. Polym. Sci.*, 19:353–360, 1981.

[240] T. L. Rapp, W. K. Kowalchyk, K. L. Davis, E. A. Todd, and M. D. Liu, K. L.and Morris. Acrylamide polymerization kinetics in gel electrophoresis capillaries a raman microprobe study. *Anal. Chem.*, 64:2434–2437, 1992.

[241] A. Usanmaz. Crystal structure effect in radiation-induced solid-state polymerization of acrylamide. *Turk. J. Chem.*, 21:304–312, 1997.

[242] M. G. Bradbury, S. D. Hamann, and M. Linton. Solid-phase polymerizations at high pressures. *Aust. J. Chem.*, 23:511–523, 1970.

[243] A. A. Zharov. The polymerisation of solid monomers under conditions of deformation at a high pressure. *Russ. Chem. Rev.*, 53:140, 1984.

[244] L. V. Babare. *Fiz. Goreniya Vzryva*, 17:133, 1981.

[245] T. A. Fadner and H. Morawetz. Polymerization in the crystalline state. i. acrylamide. *J. Polym. Sci.*, 45:475–501, 1960.

[246] B. W. Dodson and C. A. Jr. Arnold. Shock-induced activation of acrylamide polymerization. *J. Phys. Chem.*, 87:3023–3024, 1983.

[247] N. P. Chistotina and A. A. Zharov. Transformations of acrylamide and polyacrylamide at high pressures and large shear deformations. *Bull. Russ. Acad. Sci.*, 41:944–949, 1992.

[248] L. Ciabini, M. Santoro, R. Bini, and V. Schettino. High pressure reactivity of solid benzene probed by infrared spectroscopy. *J. Chem. Phys.*, 116(7):2928–2935, 2002.

[249] C. Murli and Y. Song. Pressure-induced polymerization of acrylic acid: A raman spectroscopic study. *J. Phys. Chem. B*, 114(30):9744–9750, 2010.

[250] C. Murli, A. K. Mishra, S. Thomas, and Sharma S. M. Ring-opening polymerization in carnosine under pressure. *J. Phys. Chem. B*, 116(15):4671–4676, 2012.

[251] S. Sasaki, K. Nagata, and H. Shimizu. High-pressure raman study of hydrogen bonds in crystalline formamide. *Ferroelectrics*, 95:243–247, 1989.

[252] H. Shimizu, K. Nagata, and S. Sasaki. High-pressure raman study of the hydrogen-bonded crystalline formamide. *J. Chem. Phys.*, 89(5):2743–2747, 1988.

[253] R. Gajda and A. Katrusiak. Pressure-promoted ch- - -o hydrogen bonds in formamide aggregates. *Cryst. Growth Des.*, 11(11):4768–4774, 2011.

[254] M. Hamann, S. D.and Linton. The influence of pressure on the infrared spectra of hydrogen-bonded solids-iii. compounds with n-h...x bonds. *Aust. J. Chem.*, 29(8):1641–1647, 1976.

[255] P. Colomban, G. Sagon, M. Lesage, and J. M. H. Ramirez. Micro-raman study of the compressive behaviour of advanced pa66 polyamide fibres in a diamond-anvil cell. *Vib. Spectros.*, 37:83–90, 2005.

[256] T. Yan, S. Li, K. Wang, X. Tan, Z. Jiang, K. Yang, B. Liu, G. Zou, and B. Zou. Pressure-induced phase transition in n-h- - -o hydrogen-bonded molecular crystal ox-amide. *J. Phys. Chem. B*, 116(32):9796âĂŞ9802, 2012.

[257] Isakov I. V. Crystal structure of acrylamide. *J. Struct. Chem.*, 7:836–837, 1966.

[258] N. Jonathan. The infrared and raman spectra and structure of acrylamide. *J. Mol. Spectrosc.*, 6:205–214, 1961.

[259] R. Murugan, S. Mohan, and A. Bigotto. Ftir and polarized raman spectra of acrylamide and polyacrylamide. *J. Korean Phys. Soc.*, 32(4):505–512, 1998.

[260] A.S.R. Duarte, A.M. Amorim da Costa, and A.M. Amado. On the conformation of neat acrylamide dimers - a study by ab initio calculations and vibrational spectroscopy. *J. Mol. Struc. THEOCHEM.*, 723:63–68, 2005.

[261] K. Nakamoto, M. Magoshes, and R. E. Rundle. Stretching frequencies as a function of distances in hydrogen bonds. *J. Am. Chem. Soc.*, 77(24):6480–6486, 1955.

[262] C. Baldock, L. Rintoul, S. F. Keevil, J. M. Pope, and G. A. George. Fourier transform raman spectroscopy of polyacrylamide gels (pags) for radiation dosimetry. *Phys. Med. Biol.*, 43:3617–3627, 1998.

[263] J. S. Suh and K. H. Michaelian. Surface-enhanced raman spectroscopy of acrylamide and polyacrylamide adsorbed on silver colloid surfaces: Polymerization of acrylamide on silver. *J. Raman Spectrosc.*, 18:409–414, 1987.

[264] D. Chelazzi, M. Ceppatelli, M. Santoro, R. Bini, and V. Schettino. High-pressure synthesis of crystalline polyethylene using optical catalysis. *Nat. Mater.*, 3:470–475, 2004.

[265] H. Bhatt and M. N. Deo. A synchrotron infrared absorption study of pressure induced polymerization of acrylamide. *Spectrochim Acta A*, 185:45 – 51, 2017.

[266] L. L. De. Naturally occurring and synthetic imidazoles: Their chemistry and their biological activities. *Curr. Med. Chem.*, 13:1–23, 2006.

[267] J. Chengmin, C. Tianliang, S. Zhihua, G. Yan, L. Wenxiong, L. Junhua, S. Qian, and H. Maochun. Crystal growth and characterization of imidazolium l-tartrate (imlt): A novel organic nonlinear optical material with a high laser-induced damage threshold. *CrystEngComm*, 15:2157–2162, 2013.

[268] S. Horiuchi, F. Kagawa, K. Hatahara, K. Kobayashi, R. Kumai, Y. Murakami, and Y. Tokura. Above room temperature ferroelectricity and antiferroelectricity in benz-imidazoles. *Nat. Commun.*, 3:1308–1314, 2012.

[269] A. Kawada, A. R. McGuie, and M. M. Labes. Protonic conductivity in imidazole single crystal. *J. Chem. Phys.*, 52:3121–3125, 1970.

[270] I. Fischbach, H. W. Spiess, K. Saalwachter, and G. R. Goward. Solid state nmr spectroscopic investigations of model compounds for imidazole-based proton conductors. *J. Phys. Chem. B*, (108):18500–18508, 2004.

[271] S. M. Sharma and S. K. Sikka. Pressure induced amorphization of materials. *Prog. Mater. Sci.*, (40):1–11, 1996.

[272] W. Xu, E. Greenberg, G. K. Rozenberg, M. P. Pasternak, E. Bykova, T. Boffa-Ballaran, L. Dubrovinsky, V. Prakapenka, M. Hanfland, and O. Y. Vekilova. Pressure induced hydrogen bond symmetrization in iron oxyhydroxid. *Phys. Rev. Lett.*, 111:175501–175505, 2013.

[273] A. H. Benoit, M.and Romero and D. Marx. Reassigning hydrogen-bond centering in dense ice. *Phys. Rev. Lett.*, 89:145501–145505, 2002.

[274] M. Sikora and A. Katrusiak. Pressure-controlled neutral-ionic transition and disordering of nh- - -n hydrogen bonds in pyrazole. *J. Phys. Chem. C*, 117:10661–10668, 2013.

[275] A. Goncharov, M. Manaa, J. Zaug, R. Gee, L. Fried, and W. Montgomery. Polymerization of formic acid under high pressure. *Phys. Rev. Lett.*, 94:065505–065509, 2005.

[276] P. D. Serpell, C. J.and Beer. Intermolecular interactions in bromo-, methyl-, and cyanoimidazole derivatives. *Cryst. Growth Des.*, 13:2866–2871, 2013.

[277] W. Zielinski and A. Katrusiak. Hydrogen bonds nh- - -n in compressed benzimidazole polymorp. *Cryst. Growth Des.*, 13:696–700, 2013.

[278] M. Nishio, M. Hirota, and Y. Umezawa. *The CH-Pi Interaction: Evidence, Nature, and Consequences.* Wiley-VCH, Toronto, 1998.

[279] R. A Jiong. *Theoretical Study of CH- - -X (X = O, N, S, P and π) Interactions.* PhD thesis, National University of Singapore, Singapore, 2006.

[280] J. P. Perdew, K. Burke, and M. Ernzerhof. Generalized gradient approximation made simple. *Phys. Rev. Lett.*, 77:3865–3868, 1996.

[281] G. Kresse and J. Hafner. Norm-conserving and ultrasoft pseudopotentials for first-row and transition elements. *J. Phys.-Condens. Mat.*, 6:8245–8257, 1994.

[282] G. Kresse and D. Joubert. From ultrasoft pseudopotentials to the projector augmented-wave method. *Phys. Rev. B*, 59:1758–1775, 1999.

[283] P. E. Blochl. Projector augmented-wave method. *Phys. Rev. B*, 50:17953–17979, 1994.

[284] P. Giannozzi, S. Baroni, N. Bonini, M. Calandra, R. Car, C. Cavazzoni, D. Ceresoli, G. L. Chiarotti, M. Cococcioni, and I. Dabo. Quantum espresso: A modular and open-source software project for quantum simulations of materials. *J.Phys.: Condens. Mat.*, 21:1–19, 2009.

[285] J. P. Perdew and A. Zunger. Self-interaction correction to density-functional approximations for many-electron system. *Phys. Rev. B*, 23:5048–5079, 1981.

[286] D. A. Carter and J. E. Pemberton. Surface-enhanced raman scattering of the acid-base forms of imidazole on ag. *Langmuir*, 8:1218–1225, 1992.

[287] D. A. Carter and J. E. Pemberton. Raman spectroscopy and vibrational assignments of 1 and 2-methylimidazole. *J. Raman Spectrosc.*, 28:939–946, 1997.

[288] L. Colombo. Low frequency raman spectrum of imidazole single crystal. *J. Chem. Phys.*, 49:4688–4695, 1968.

[289] L. Colombo, P. Bleckmann, B. Schrader, R. Schneider, and T. Plesser. Calculation of normal vibrations and intra- and intermolecular force constants in crystalline imidazole. *J. Chem. Phys.*, 61:3270–3278, 1974.

[290] P. W. Loeffen, R. F. Pettifer, F. Fillaux, and G. J. Kearley. Vibrational force field of solid imidazole from inelastic neutron scattering. *J. Chem. Phys.*, 103:8444–8455, 1995.

[291] M. Majoube and G. Vergoten. Lattice vibrations of crystalline imidazole and [15]n and d substituted analogs. *J. Chem. Phys.*, 76:2838–2847, 1982.

[292] L. M. Markham, L. C. Mayne, B. S. Hudson, and M. Z. Zgierski. Resonance raman studies of imidazole, imidazolium, and their derivatives: The effect of deuterium substitution. *J. Phys. Chem.*, 97:10319–10325, 1993.

[293] C. Perchard and A. Novak. Far-infrared spectra and hydrogen-bond frequencies of imidazole. *J. Chem. Phys.*, 48:3079–3084, 1968.

[294] J. Sadlej, A. Jaworski, and K.A Miaskiewicz. Theoretical study of the vibrational spectra of imidazole and its different forms. *J. Mol. Struct.*, 274:247–257, 1992.

[295] G. S. S. Saini, S. Kaur, S.K. Tripathi, S. D. Dogra, J. M. Abbas, and C.G Mahajan. Vibrational spectroscopic and density functional theory studies of chloranil-imidazole interaction. *Vib. Spectrosc.*, 56:66–73, 2011.

[296] G. T. Shiau, J. L. Walter, and S. S. T. King. Lattice vibrations of imidazole crystals. *Spectrosc. Lett.*, 8:459–473, 1975.

[297] T. Lankau and C. H. Yu. A quantum description of the proton movement in an idealized nhn$^+$ bridge. *Phys. Chem. Chem. Phys.*, 13:12758–12769, 2011.

[298] T. Palasyuk, I. Troyan, M. Eremets, V. Drozd, S. Medvedev, P. Z. Ejgierd, E. M. Palasyuk, H. Wang, S. A. Bonev, and D. Dudenko. Ammonia as a case study for the spontaneous ionization of a simple hydrogen-bonded compound. *Nat. Commun.*, 5:3460, 2014.

[299] C. L. Perrin and J. B. Nielson. âĂIJstrongâĂİ hydrogen bonds in chemistry and biology. *Annu. Rev. Phys. Chem.*, 48:511–544, 1997.

[300] C. C. Su, H. C. Chang, J. C. Jiang, P. Y. Wei, L. C. Lu, and S. H. Lin. Evidence of charge-enhanced c-h-o interactions in aqueous protonated imidazole probed by high pressure infrared spectroscopy. *J. Chem. Phys.*, 119:10753–10758, 2003.

[301] K. Dziubek, M. Podsiadlo, and A. Katrusiak. Nearly isostructural polymorphs of ethynylbenzene: Resolution of ch—π(arene) and cooperative =ch- - -π(c=c) interactions by pressure. *J. Am. Chem. Soc.*, 129:12620–12621, 2007.

[302] M. Zhou, K. Wang, Z. Mena, S. Gao, Z. Li, and C. Sun. Study of high-pressure raman intensity behavior of aromatic hydrocarbons:benzene, biphenyl and naphthalene. *Spectrochim. Acta, Part A*, 97:526–531, 2012.

[303] G. Wang, J. Shi, H. Yang, X. Wu, Z. Zhang, R. Gu, and P. Cao. Surface-enhanced raman scattering of imidazole adsorbed on an iron surface. *J. Raman Spectrosc.*, 33:125–130, 2002.

[304] S. Inagaki, H. Murai, and T. Takeuchi. Theory of electron localization and its application to blue-shifting hydrogen bonds. *Phys. Chem. Chem. Phys.*, 14:2008–2014, 2012.

[305] K. Hermansson. Blue-shifting hydrogen bonds. *J. Phys. Chem. A*, 106:4695–4702, 2002.

[306] P. Hobza and Z. Havla. Blue-shifting hydrogen bonds. *Chem. Rev.*, 100:4253–4264, 2000.

[307] M. Bernasconi, G. L. Chiarotti, P. Focher, M. Parrinello, and E. Tosatti. Solid-state polymerization of acetylene under pressure: Ab initio simulation. *Phys. Rev. Lett.*, 78:2008–2011, 1997.

[308] M. Ceppatelli, L. Fontana, and M. Citroni. The high pressure reactivity of substituted acetylenes: A vibrational study on diphenylacetylene. *Phase Transit.*, 80:1085–1110, 2010.

[309] S. Yan, Isabelle G. L., D. Celine, G. Celine, L. Murielle, and L. Olivier. First evidence of a phase transition in a high-pressure metal iodate: Structural and thermal studies of agio$_3$ polymorphs. *Eur. J. Inorg. Chem.*, 2013:3526 – 3532, 2013.

[310] W. W. Zhang, Q. L. Cui, Y. W. Pan, S. S. Dong, J. Liu, and G. T. Zou. First evidence of a phase transition in a high-pressure metal iodate: Structural and thermal studies of agio$_3$ polymorphs. *J. Phys.- Condensed Mat.*, 14(44), 2002.

[311] L. Bayarjargal, L. Wiehl, A. Friedrich, B. Winkler, E. A. A. Juarez, W. Morgenroth, and E. Haussuhl. Phase transitions in kio$_3$. *J. Phys.- Condensed Mat.*, 24(32), 2012.

[312] Z. X. Shen, X. B. Wang, H. P. Li, S. H. Tang, and F. Zhou. High pressure raman studies of kio$_3$ single crystals. *Rev. High Pressure Sci. Technol.*, 7:751 – 753, 1998.

[313] J. R. Durig, O. D. Bonner, and W. H. Breazeale. Raman studies of iodic acid and sodium iodate. *J. Phys. Chem.*, 69:3886 – 3892, 1965.

[314] J. G. Bergman Jr., G. D. Boyd, A. Ashkin, and S. K. Kurtz. New nonlinear optical materials: Metal oxides with nonbonded electrons. *J. Appl. Phys.*, 40(7):2860–2863, 1969.

[315] B. Bentria, D. Benbertal, M. Bagieu-Beucher, R. Masse, and A. Mosset. Crystal structure of anhydrous bismuth iodate, bi(io$_3$)$_3$. *J. Chem. Crystallogr.*, 33(11):867–873, 2003.

[316] B. Bentria, B. Djamal, B. B. Muriel, Alain M., and Julien Z. Crystal engineering strategy for quadratic nonlinear optics. part ii: Hg(io$_3$)$_2$. *Solid State Sci.*, 5(2):359 – 365, 2003.

[317] K. Stahl and M. Szafranski. High pressure raman studies of kio$_3$ single crystals. *Act. Cryst.*, C48:1571 – 1574, 1992.

[318] D. Xue and S. Zhang. Effect of hydrogen bonds on optical nonlinearities of inorganic crystals. *Chem. Phys. Lett.*, 301(5-6):449 – 452, 1999.

[319] M. Kim and C. S. Yoo. Phase transitions in i$_2$o$_5$ at high pressures: Raman and x-ray diffraction studies. *Chem. Phys. Lett.*, 648:13 – 18, 2016.

[320] G. Cavallo, P. Metrangolo, R. Milani, T. Pilati, A. Priimagi, G. Resnati, and G. Terraneo. The halogen bond. *Chem. Rev.*, 116:2478 – 2601, 2016.

[321] S. Yamamoto, Y. Ohashi, Y. Masubuchi, T. Takeda, T. Motohashi, and S. Kikkawa. Niobium-aluminum oxynitride prepared by ammonolysis of oxide precursor obtained through the citrate route. *J. Alloy Compd.*, 482(1):160 – 163, 2009.

[322] Y. Ohashi, T. Motohashi, T. Masubuchi, T. Moriga, K. Murai, and S. Kikkawa. Preparation, crystal structure, and superconductive characteristics of new oxynitrides (nb_{1-x} m_x)($n_{1-y}O_y$) where m=mg, si, and x=y. *J. Solid State Chem.*, 184:2061 – 2065, 2011.

[323] Y. Ohashi, T. Motohashi, Y. Masubuchi, and S. Kikkawa. Crystal structure and superconductive characteristics of $nb_{0.89}al_{0.11}$ oxynitrides. *J. Solid State Chem.*, 183:1710 – 1714, 2010.

[324] Y. Ohashi, S. Kikkawa, I. Felner, M.I. Tsindlekht, D. Venkateshwarlu, V. Ganesan, and J.V. Yakhmi. Superconductivity in quaternary niobium oxynitrides containing main group elements (m=mg, al, si). *J. Solid State Chem.*, 188:66 – 71, 2012.